UNIVERSITY OF NAPLES FEDERICO II

Department of Industrial Engineering

Mechanic and Energetic Section

Ph.D SCHOOL IN INDUSTRIAL ENGINEERING - XXXII Cycle

High Performance Gasoline Engine Development Approach for New Current Requirements

Ph.D School Coordinator:

Prof. Michele Grassi

Ph.D Candidate:

Eng. Antonio Aliperti

Ph.D Tutor:

Prof. Fabio Bozza

Prof. Vincenzo De Bellis

Index

1. **Starting point**

Nowadays the efforts aimed at enhancing the Internal Combustion Engines (ICEs) are mainly focused on the fuel consumption minimization to comply with binding CO_2 emission legislation for vehicle homologation. Concerning the Spark-Ignition ICEs, the most widespread path to satisfy the pollutant emission limits is the adoption of a three-way catalyst (TWC) along the exhaust line. As known, this solution poses some issues, such as a low efficiency at cold start or an effectiveness degradation because of aging. In addition, it involves the impossibility to exploit the advantages of lean combustions, since a close to stoichiometric air/fuel mixture is mandatory for efficient TWC operation. For the above reasons, a growing interest towards solutions limiting engine raw emissions is emerging. So future legislation requires new technical measures to increase engine efficiency and reduce pollutant emissions.

Here gasoline engines with high specific power have a huge development potential, since, on the one hand, knocking at high Brake Mean Effective Pressure (BMEP) limits thermal efficiency and, on the other hand, high power densities lead to increased thermal loads, which, for component protection reasons, need to be controlled by means of enrichment beyond the stoichiometric air-fuel ratio.

This operation leads to increased fuel consumption and to higher pollutant emissions; especially harmful soot particles, hydrocarbons and carbon monoxide are emitted in a higher amount.

In addition to known systems, such as exhaust manifolds integrated in the cylinder head for direct cooling of the exhaust gas, extended effective expansion by optimized valve timings (Miller, Atkinson) and external cooled exhaust gas recirculation, also new technologies are being developed for passenger cars. Those technologies primarily aim to widen the lambda one range of the engine in order to maintain the stoichiometric air/fuel ratio throughout the entire engine operating range, which is expected to be required for future Real Driving Emissions (RDE) legislation.

The first chapter explains the current situation and future direction of internal combustion engines, with a particular focus on the gasoline engines with high specific power and covers broad regulatory changes in the last year related to tailpipe emissions of criteria pollutants and CO_2/fuel economy. Throughout the chapter, a brief overview of internal combustion engines and their future development will be provided so to understand and appreciate why it is still relevant to conduct research in this field, while facilitating the improvement of green technologies in order to achieve a sustainable transportation system. The motivation behind this study and the research direction will also be clarified.

Then, a Lamborghini 12-cylinder naturally aspirated spark ignition engine is investigated. The engine is experimentally tested under full and part load operation with two different Air-to-fuel ratio maps. Main performance parameters, in-cylinder pressure cycles and raw pollutant emissions are measured. The engine is schematized in a one-dimensional model (GT-Power™), where “user routines” are employed to simulate turbulence, combustion, knock and pollutant production. 1D model is validated against the experimental data, denoting a good accuracy. The innovative contribution of this section can be hence recognized in the development of a 1D model characterized by a single set of tuning constants allowing for an accurate reproduction of the combustion process in all the engine configurations. As better explained in the following, the combustion model is in fact coupled to a turbulence sub-model, preliminary tuned with reference to 3D-CFD results, in motored operation. This methodology is particularly helpful in the calibration of a VVT engine, where the turbulence levels substantially vary at part load according to the intake/exhaust valve strategies. Combustion and turbulence constants are hence selected through comparisons with few experimental data at full load and 3D results, and then employed at part load and in the optimization process, as well.

The results about the raw emissions put into evidence that the numerical approach predicts the experimental data of carbon monoxide (CO) and nitrogen oxides (NO), but it is not enough advanced to reproduce the hydrocarbon (HC) level, although the variations with the engine operating parameters (speed, load, air/fuel ratio) are captured. The model is employed to study the water injection impact to draw the variation trend of the exhaust temperature, performance and the pollutant emissions changing the engine hardware,

rather than to predict their absolute levels. The combustion speed takes into account the water presence with a refined correlation of laminar flame velocity and the knock model gives the possibility to set the best spark advance. The water evaporation reduces the in-cylinder temperature and, as a consequence the knock level, is lower.

The computed HC, CO and NO maps have been embedded in a vehicle simulation to estimate the impact of the analysed technical solutions on a RDE cycle suggested by Lamborghini. In this way, with a fully numerical approach, a new hardware is analysed and its impact in term of pollutions level is verified on a realistic drive cycle that the new regulations seems to impose. In this way, a new approach to design the future high performance engines has been individuated and the impact of the new regulations can be seen before experimental tests, reducing the time to market and the economic effort. Then, the difference between the engine out emission level and the limit that the regulation imposes can help also to design the after-treatment system.

Summarizing, the presented numerical approach showed the potential to predict, on a physical basis, the combined effects of various techniques on the engine performance. This methodology could represent an effective tool to identify the trade-off between engine complexity and expected improvements, contributing to support and drive the development process of new engine/vehicle.

2. Description of operation of modern Spark Ignition Engines and future direction

Description of Spark-Ignition internal combustion engine

Internal combustion engines (ICEs) allow to obtain mechanical power from the chemical energy contained in the fuel, which is burned inside the engine itself. Due to this configuration, the working fluids of internal combustion engines are the air-fuel mixture (before the combustion process) and the exhaust gases (after the combustion process); the interaction between these working fluids and the mechanical parts of the engine provides the desired power output.

For their simplicity and favourable power-weight ratio, two types of internal combustion engines have found wide application in transport and power generation sectors: the spark-ignition engines (called also Otto engines, or gasoline engines) and the compression-ignition or Diesel engines.

The development of internal combustion engines started in the mid of the 19th century but, despite the technological evolution, today the engines are still continuously subjected to improvements related to efficiency, power output and reduction of the emissions, thanks to research activities which keep on providing increasingly efficient technologies and better materials.

There are different types of internal combustion engines. They can be classified according to the main technical differences:

- Basic design of the engine: reciprocating engines (in-line, radial or V disposition of the cylinders) and rotary engines (the most famous being the Wankel disposal).
- Used fuel: for example, gasoline (or petrol), diesel fuel, hydrogen, natural gas, alcohols (ethanol or methanol).
- Method of mixture preparation: carburetion (by means of a carburettor), indirect fuel injection into the intake ports or manifolds and direct fuel injection (directly into the engine cylinder).

- Method of ignition: it corresponds to the previously mentioned diversification between petrol engines (spark ignition, SI) and Diesel engines (compression ignition, CI).
- Method of engine cooling: water cooled, air cooled (forced convection) or cooling by natural convection and radiation.
- Working cycle of the engine: four-stroke cycle, which can be naturally aspirated or turbocharged; two-stroke cycle (crankcase scavenged or turbocharged).

The majority of internal combustion engines are characterized by a four-stroke working cycle, where each piston of the engine is subjected to four strokes (corresponding to two revolutions of the crankshaft) for every cycle. As an example, Figure 2.1 depicts the strokes for a SI engine.

The four-stroke full cycle is now going to be briefly described, and the theory which will be reported is to be considered valid for both CI and SI engines.

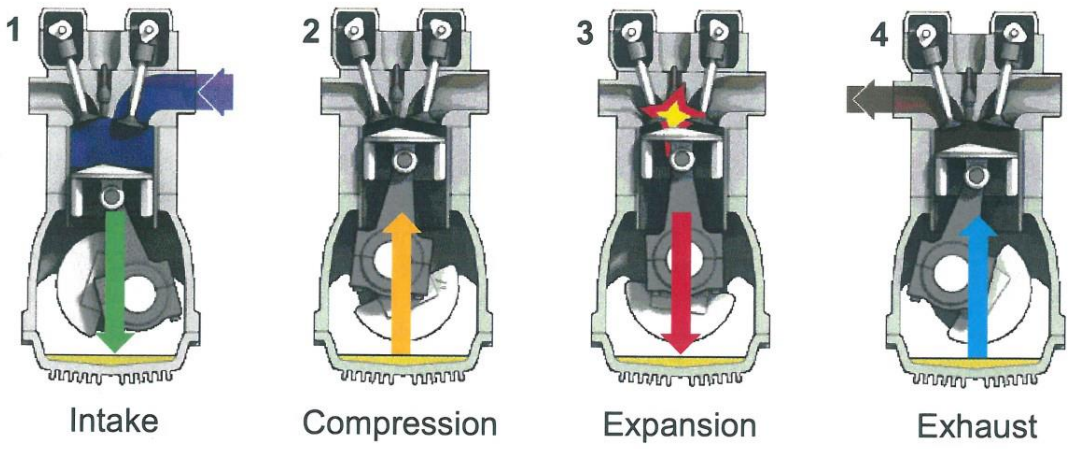

Figure 2.1 – Strokes for a 4-strokes Spark Ignition engine.

Intake Stroke: during this phase, the piston moves from the Top Dead Centre (TDC) to the Bottom Dead Centre (BDC). The opening of the intake valve allows the fresh air/fuel mixture to enter the cylinder. In presence of an Exhaust Gas Recirculation (EGR) system, the exhaust gases from previous cycles and fresh mixture are introduced into cylinder. To optimize the cylinder filling, the intake valve opening (IVO) is usually realized before TDC

(typically 0-40 degrees) while the intake valve closure (IVC) occurs after the BDC (typically 50 degrees after BDC).

Compression Stroke: this phase starts when the intake valves are closed and the mixture in cylinder is formed by fresh charge of premixed fuel and air and exhaust gases of previous cycles (internal EGR). The piston moves from BDC to TDC by increasing both pressure and temperature of gas inside the cylinder. Towards the end of the compression stroke (some degrees before TDC), the combustion process starts and thus the pressure and temperature inside the cylinder increase even more rapidly.

Expansion Stroke: it begins when the piston is at TDC and finishes when the exhaust valve opens. Expansion stroke allows to obtain useful work thanks to the energy released by the combustion process. Indeed, the chemical energy of the fuel is transformed into mechanical work by the force that the high-pressure gases exert on the piston.

Exhaust Stroke: it starts with the opening of the exhaust valve. Exhaust valve opening (EVO) happens before the piston reaches the Bottom Dead Center (BDC). This phase can be divided into two sub-phases: spontaneous exhaust and forced exhaust. In the former phase, the pressure of the gases within the cylinder is substantially higher than the pressure in the exhaust manifold. For the latter phase, the piston moves from BDC to TDC and pushes the burnt gases to the exhaust valve. As the piston approaches the TDC, the inlet valve opens and just after the TDC the exhaust valve closes, and the cycle starts again. Figure 2.2, related to a four strokes of a SI engine, shows that an overlap period when both intake and exhaust valves remain opened occurs. As known, this overlap is properly designed for the optimization of the engine exhaust gas process.

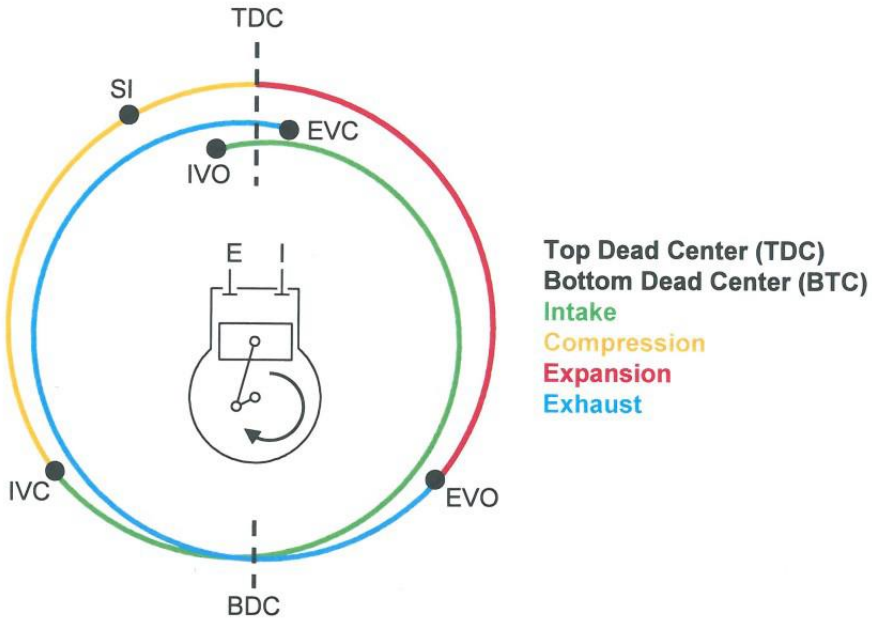

Figure 2.2 – Strokes for a 4-strokes Spark Ignition engine.

Referring to the 4-strokes SI engine cycle, Figure 2.3 shows a typical in-cylinder pressure trace in firing condition (solid line) and in motored condition (dashed line) together with the in-cylinder volume variation and mass fraction burned as a function of the engine crank angle. In the actual engine operation, air and fuel are usually mixed together in the intake system, before entering the cylinder by using a fuel injection system (port injection). The mass flow rate and consequently the engine power is controlled by adjusting the throttle valve. With port-injection, fuel is injected through individual injectors from a low-pressure fuel supply system into each intake port. There are several types of injection systems, but the one more widely adopted is the electronically controlled injection system.

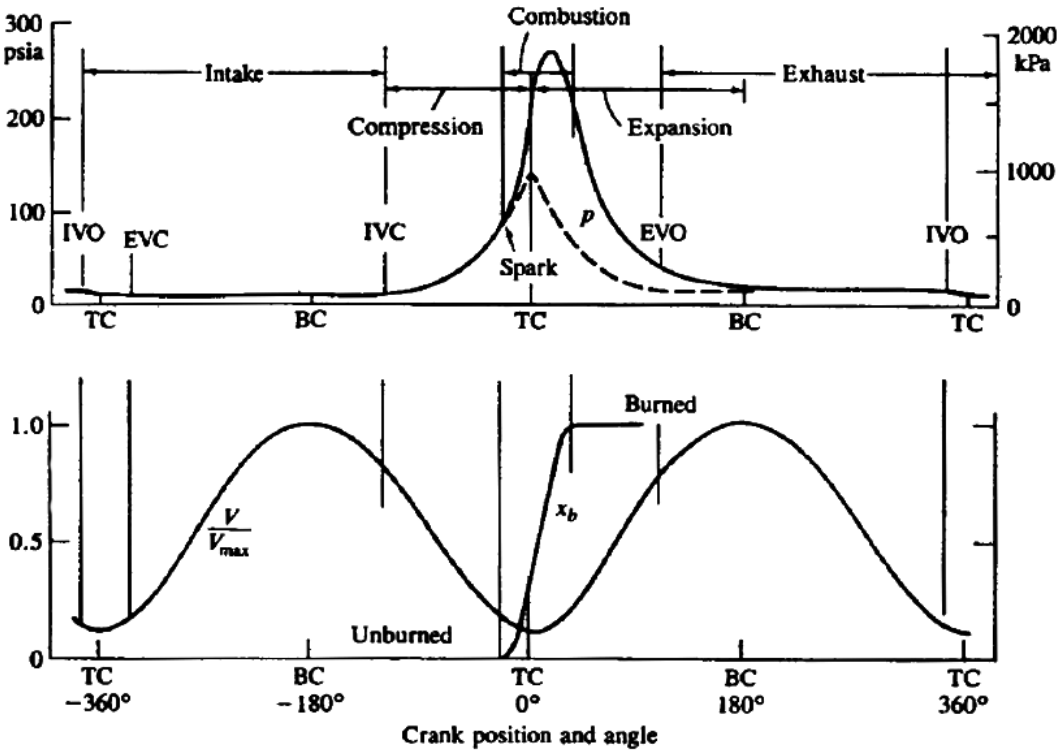

Figure 2.3 – In-cylinder pressure traces (a), volume and mass fraction burned (b) as a function of crank angle for a typical automotive SI engine.

As shown in Figure 2.3a, after the intake valve closure (IVC), the cylinder contents (air, fuel and residual gases) are compressed and during this phase, heat transfer to the piston, cylinder head, and cylinder walls occurs, but it exerts a slight influence on the unburned gas properties. An electric discharge across the spark plug is realized with a certain advance before the top dead centre (between 10 and 40 degrees), allowing the combustion process to take place within the engine cylinder. A turbulent flame develops from the spark discharge, propagates across the mixture in the cylinder and extinguishes at the combustion chamber wall. The duration of the burning process may vary with engine design and operation, but typically it covers an interval between 40 and 60 degrees (Figure 2.3). In presence of combustion, the in-cylinder pressure rises above the level due to the sole compression (motored or non-firing condition). In a spark ignition engine, due to differences in flow pattern and mixture composition between cylinders and differences among consecutive engine cycles in a single cylinder, not negligible variations in the development of each combustion process occur. As a consequence, significant variations in combustion process development for consecutive engine cycles in a single cylinder

have to be expected. This phenomenon is known as cycle by cycle variation of SI engines. In addition, these engines are also affected by knock occurrence in certain engine operating conditions, especially at high loads and low speeds. Knock phenomenon represents the most important abnormal combustion process for gasoline engines. According to the prevalent theory, it derives from the auto-ignition of a part of the gas mixture ahead the advancing flame front. Knocking combustions have to be avoided during the normal engine operation or reduced at a very low level because they cause severe engine damages and reduce the efficiency. This phenomenon bounds the maximum allowable engine compression ratio, especially in the case of turbocharged SI engines, and it causes limitations on the engine efficiency.

Modern technologies for gasoline engines

One approach to improve fuel economy is limiting the use of fuel enrichment, currently done to limit exhaust temperatures for protection of downstream components such as turbochargers and catalysts. Future regulations may limit fuel enrichment due to the lower fuel economy and high emissions inherent to the strategy. Studies show that CO emissions can especially be a concern during fuel enrichment. CO is currently only limited on the WLTP, but not on the RDE. During tests on a C-segment vehicle over a dynamic RDE scenario, Görgen et al. measured CO emissions > 3 times the WLTC limit, with a great fraction associated with over-fueling during full load accelerations. To enable stoichiometric ($\lambda=1$) operation over the entire engine map, technologies which decrease exhaust temperatures are being developed. These include exhaust gas recirculation (EGR), variable compression ratio (VCR), water injection (WI), and advanced boosting systems which combine increased turbine size with electrically assisted turbocharging and mild hybridization to overcome the loss in low-end torque (LT). Glahn et al. provide an overview of the potential of these technologies to extend the specific power of modern downsized engines. Compared to a conventional turbocharged 3-cylinder GDI engine, a combination of improved engine integration, integrated exhaust manifold and Miller cycle combined with variable geometry turbocharging can increase the specific power from 65 kW/L to 85 kW/L, at ~ 10% additional cost. External EGR can further increase the specific

power output up to 90 kW/L, but increases the cost by about 32%. VCR and WI can extend the benefit to 100 kW/L at similar costs, but the technology is not yet enough mature.

So modern gasoline engines are characterized by advanced technologies which involve the adoption of a variety of new components and sub-systems, aiming to improve the fuel consumption and to reduce the noxious emissions. These technical solutions are here listed and will be briefly discussed in the following:

- Compression ratio adjustment
- Water injection technology
- Turbulent jet ignition

Compression ratio adjustment

Variable compression ratio (VCR) system allows the geometrical compression ratio of an engine to be automatically adjusted in order to optimise the combustion process under different load and speed conditions. In general, compression ratio for SI PFI engines varies from 8 to 12. The main solution to prevent knock occurrence during full load operation is to reduce the volumetric compression ratio. However, this method lowers engine efficiency and performance at part load operating points, where pressure and temperature conditions do not favour knocking combustion. VCR system is capable to automatically adjust the compression ratio as a function of the operating point. With the adoption of this system, the compression ratio is limited at high loads, where the probability of knock occurrence is higher, while it is increased at low loads. This technology is still in research stage and it is not commercially available yet due to its mechanical complexity. Anyway, research done by the European Commission Community showed that VCR engines can achieve a reduction in fuel consumption up to 9%, compared to state-of-the-art turbocharged gasoline engines with a constant compression ratio [7].

Water injection

Water Injection (WI) technology represents a promising method for gasoline engines capable to furnish several advantages. In particular, water injection within the intake

manifold proves to drastically reduce temperature of the gases within the combustion chamber and at turbine inlet for turbocharged engine.

Because of heat subtracted by evaporation, the introduction of liquid water within the cylinders has a cooling effect on the fresh charge, increasing its density during the intake phase, and hence enhancing the volumetric efficiency. In addition, the injected water results in a greater mass of working gas during the expansion phase, and hence in an increased expansion work. On the other hand, the water directly affects the combustion process, generally causing a reduced burn rate. The evaporation-related cooling promotes a temperature drop during the compression stroke [18] [18] [19] that substantially contributes to mitigate the knock tendency. In addition, the temperature reduction is enhanced by the increased heat capacity of the charge, due to the larger content of inert in the cylinder.

So the reduction in gas temperature mitigates the knock tendency, mainly thanks to the heat subtracted by the water evaporation. The adoption of port water injection method allows to improve the fuel consumption of turbocharged gasoline engines, while preserving engine performance and knock safety margin [20] [21].

Turbulent jet ignition

The turbulent jet ignition in contrast to conventional ignition systems with spark discharge, is characterized by a particularly high ignition energy – sometimes by several orders of magnitude. The basic principle: the spark plug is separated from the main combustion chamber in a small space. As a result, only a portion of the mixture is initially burned – pressure and temperature in the pre-chamber rise rapidly. Through several overflow channels that connect the pre-chamber to the main combustion chamber, gas or flame jets pass over.

These take on two crucial tasks: after the jets penetrate deeply into the main combustion chamber, they ignite the mixture in several spots at the same time and they introduce additional turbulence. Due to the high ignition energy, the pre-chamber can therefore also ignite mixtures which are diluted with air or residual gas and which usually cannot be ignited with conventional spark ignition. Furthermore, the flame jets burn through the

mixture in the main combustion chamber much faster. The pre-chamber can be passive or active: in passive configuration, it is filled only during the compression stroke via the main combustion chamber. For the active configuration, an additional fuel-metering device is attached to the pre-chamber, which fills it separately with fuel.

Where there is normally a spherical flame propagation from a central ignition location, with a pre-chamber the mixture is burned from outside to the middle. Thus, the areas normally critical in terms of knock – such as the piston top ring – are reached by the flame much earlier. Together with an about 30 % shorter burn duration with the same combustion center position, the center of heat release can be advanced by about 4 to 5°CA. This in turn allows an increase in the compression ratio, with the aim of reducing the fuel consumption at part load.

CO_2 or Fuel Consumption

Most of the major vehicle markets have introduced energy efficiency regulations for the vehicle manufacturers to follow. Figure 2.4 provides a summary of the fleet-wide passenger car CO_2 requirements in some of the major markets. Achieving these standards will require a 3-6% reduction in tailpipe CO_2 per year.

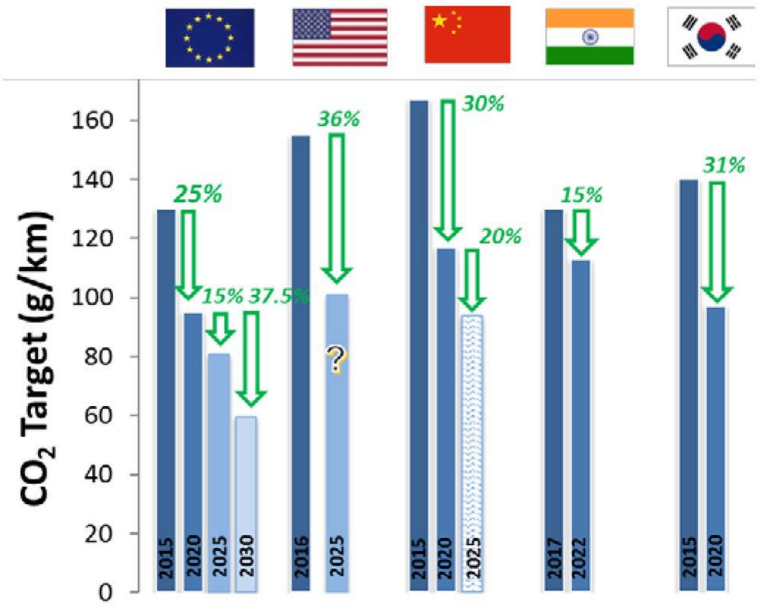

Figure 2.4 – CO2 requirements for passenger car.

In Europe, the European Commission's strategy for low-emission mobility aims to limit transport related greenhouse gas (GHG) emissions by 2050 to be at least 60% lower than in 1990. In line with the strategy, EU member states and the European Parliament in early 2019 reached an agreement to further tighten the tailpipe CO_2 targets. Compared to the New European Drive Cycle (NEDC) based CO_2 limits of 95 g/km for passenger cars and 145 g/km for light commercial vehicles in 2020, the future targets will require a 15% reduction in 2025 and 37.5% reduction in 2030 [1].
New CO_2 targets are challenging, especially as they are accompanied with changes to the measurement protocol. Real world emissions are usually higher compared to those measured under laboratory conditions. Fontaras, et al. [2] report that the difference between official and real world CO_2 emissions is as high as 30-40%, and growing over the years.

The US Environmental Protection Agency (EPA) and the National Highway Traffic Safety Administration (NHTSA), have proposed a revision to the current light-duty GHG standards [4]. For MY 2021-2026 passenger cars and light trucks. Eight alternatives have been proposed, with the preferred one aiming to freeze GHG and fuel economy standards at 2020 levels. The proposal also questions California's authority to set their own GHG and ZEV standards through the "Advanced Clean Cars" program. The low emission vehicle (LEV III) program, which sets the tightest standards for criteria pollutants, is not challenged. California Air Resource Board (CARB) has adopted a regulatory amendment which specifies that OEMs must continue to meet the original GHG standards in that state, and that vehicle manufacturers would not be "deemed to comply" with the state GHG standards if they follow any less stringent national standard.

China has a broad industrial policy to decrease dependency on imported petroleum and lead the world in electric vehicles. In this regard, the Ministry of Industry and Information Technology (MIIT) finalized the New Energy Vehicle (NEV) mandate policy [2]. The policy, expands on California's ZEV credit system, wherein vehicles get more credits for longer all-electric range, but China is the first to give more credit for higher efficiency vehicles. Auto manufacturers are required to generate 10% of NEV credits in 2019 and 12% in 2020. NEVs include plug-ins, full battery electric and fuel cell vehicles. Three credits on average per NEV could result in 4% adoption of NEVs in 2020 [2]. Excess credits can be traded to meet the NEV and also the corporate average fuel consumption requirements.

Criteria Pollutant Regulations

EURO 6 and RDE

The Real-Driving Emissions (RDE) requirements for Euro 6 passenger cars and vans went into effect starting Sept 1st 2017. The draft version of the 3rd RDE package was reviewed last year. It was officially published in June 2017, and retains the key elements: Conformity factor (CF) of 1.5 for particulate number (PN), strengthening of the regulations by including the first 5 minutes of cold start emissions in the urban portion, and an emphasis on transparency with requirements that OEMs make public the maximum RDE NOx and PN values and provide an "extended documentation package" on auxiliary emission

strategies. The regulatory package also sets the stage for inclusion of an evaluation method for hybrid and plug-in hybrid vehicles to ensure that their RDE emission values are comparable with conventional vehicles. The final method will be part of the fourth and final RDE package, expected to address in-service compliance and special provisions for light-commercial vehicles. Some changes are being considered to the RDE framework, such as inclusion of sub-23 nm particles. The two RDE analytical tools - EMROAD and CLEAR -will also be reviewed. RDE and WLTP are not perfect as there are still conditions in real world driving which are not captured in these tests. Emissions of both CO_2 and criteria pollutants are high during congested traffic, marked by more frequent start-stops and higher idling. Khalfan et al. [2] found significant increase in roadside emissions due to traffic congestion, attributed to both higher fuel consumptions at low speeds as well as lower exhaust temperatures leading to low power and extensive idling. There is also criticism that the longer duration of the new cycles (compared to NEDC) actually diminishes the relative contributions of emissions from cold-starts. There is a proposal under consideration to reform the vehicle type-approval process in Europe. The EU Commission will be authorized to carry out independent market checks, issue recalls and impose fines which do not depend on the member states. Member states will be required to carry out periodic spot checks and make results publicly available. In addition to the existing ban on defeat devices, the new rules require OEMs to provide access to software protocols.

EURO 7 preview

Discussions have started on Euro 7 regulations. In a stakeholder event to discuss future European regulations, Martini presented work being done at the Joint Research Center (JRC), on topics such as measurement of sub-23 nm particles, low temperature testing at -7 °C, and inclusion of previously non-regulated species such as ammonia, N_2O, isocyanic acid, and aldehydes. Remote sensing is being discussed as a complimentary tool to PEMS (portable emissions monitoring system) for screening high-emitters and faulty after-treatment systems.

Table 2.5 shows a preview of what the new limitations might be.

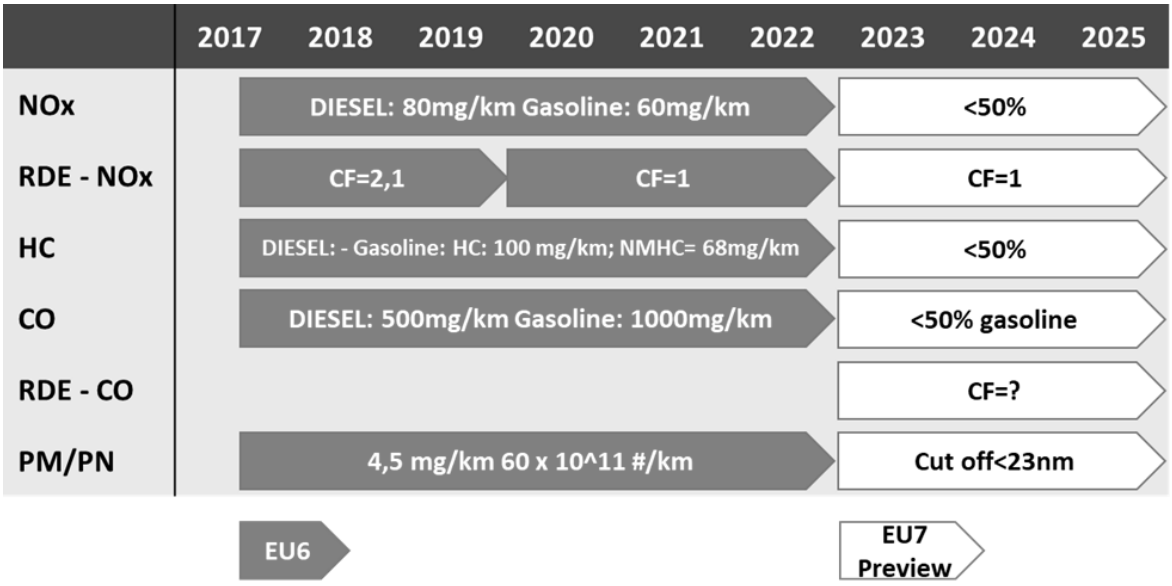

Figure 2.5 - Euro 7 regulation preview.

3. In cylinder modelling

To describe the phenomena that take place inside the engine is necessary follow the temporal evolution of some quantities (thermodynamic balance inside the cylinder, flow field, interaction between fluid dynamics and combustion process) that in general vary in time and space according to differential equations, that are not usually linear.

Due to the complexity of the system, it is always necessary to create a model that is able to simplify the description of the phenomena, thanks to more or less restrictive hypotheses. All this can be done following different modelling approaches and a certain number of equations characterizes each of them. However, even the most complex model remains an approximation of the observed physical event.

More in detail, as far as internal combustion engines are concerned, it is necessary to model the combustion process, so a correct schematization of what happens inside the cylinder during this phase is indispensable. Since this process is strongly influenced by the flow motions that occur inside the cylinder itself, in addition to the combustion model, it is necessary to create a model able to describe the generation and decay of the turbulence. There are essentially two possibilities: the first is represented by CFD analysis, computationally and economically more expensive; the second is a one-dimensional analysis, cheaper and faster. It is clear that, at an industrial level, the second one is preferred because it allows having good results in less time and with a lower economic effort, while renouncing to a detailed description of the phenomenon.

In this chapter, the in-cylinder 0D models developed from the Engine Research Team of University “Federico II” of Naples and used for this activity will be described in detail:

- Combustion model
- Turbulence model
- Emission model

Two zone combustion model

The two-zone combustion model is a thermodynamic model based on the hypotheses of stationarity and uniformity of properties within the control volume. This model is zero-dimensional and therefore allows to solve the balance equations of mass and energy within a given control volume which, in the case under consideration, will be constituted by the cylinder.

It is based on the following assumptions:

- the air and burned gases are stationary inside the cylinder

- all properties are uniform inside the cylinder

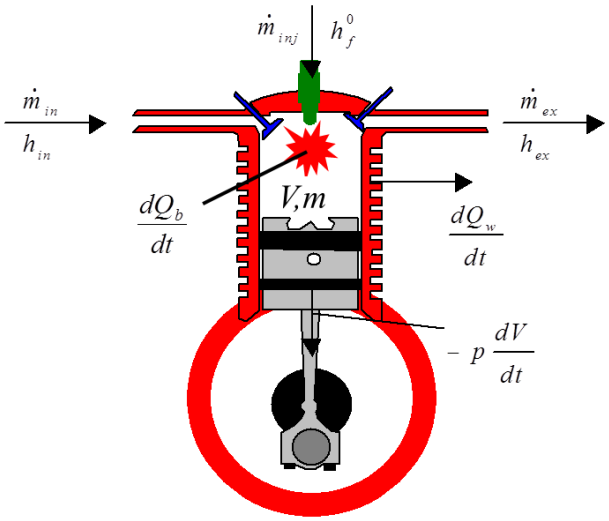

Figure 3.1 – Control volume schematization

According to the control volume defined in figure 3.1 and conveniently ignoring the mass losses due to leakage between piston and barrel, it is possible to write the mass (3.1) and energy (3.2) balance equations.

$$\frac{dm}{dt} = \dot{m}_{in} - \dot{m}_{ex} + \dot{m}_{inj} \qquad (3.1)$$

$$\frac{d(me)}{dt} = -p\frac{dV}{dt} - \frac{dQ_w}{dt} + \frac{dQ_b}{dt} + \dot{m}_{in}h_{in} - \dot{m}_{ex}h_{ex} + \dot{m}_{inj}h_f^0 \qquad (3.2)$$

Where:

$\dot{m}_{in}$ is the mass flow rate entering the intake valves

$\dot{m}_{ex}$ is the mass flow rate at the exhaust valves

$\dot{m}_{inj}$ is any mass flow rate of fuel injected directly into the cylinder

These three terms in the energy balance equation are associated with convective flows; then there are diffusive terms:

$p\frac{dV}{dt}$ is the diffusive term related to the work generated by the motion of the piston

$\frac{dQ_w}{dt}$ is the diffusive term related to heat loss through the walls of the chamber

$\frac{dQ_b}{dt}$ is the amount of heat released by the combustion process in the time unit

It is possible to note how, through an analysis of this type, it is not possible to gather any information about the propagation of the flame front; concentrating then on the volume enclosed within the combustion chamber alone, it is preferable to divide this volume into two zones:

- one including the combustion gases called Burned Zone (BZ), connected to the exhaust valve;

- one including the fresh mixture called the Unburned Zone (UZ), connected to the intake valve.

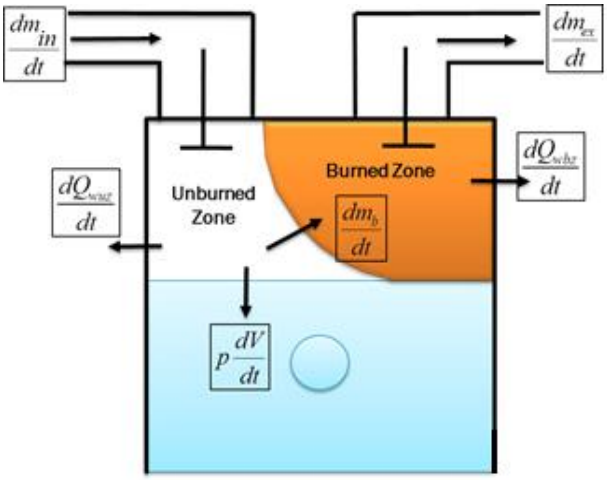

Figure 3.2 – Two zone combustion schematization

For each of these zones, the mass and energy balance equations must be rewritten.

For the unburned zone:

$$\frac{dm_{uz}}{dt} = \frac{dm_{in}}{dt} - \frac{dm_b}{dt} \tag{3.3}$$

$$\frac{dm_{uz}e_{uz}}{dt} = -p\frac{dV_{uz}}{dt} - \frac{dQ_{wuz}}{dt} + \frac{dm_{in}}{dt}h_{in} - \frac{dm_b}{dt}h_{uz} \tag{3.4}$$

For the burned zone:

$$\frac{dm_{bz}}{dt} = -\frac{dm_{ex}}{dt} + \frac{dm_b}{dt} \tag{3.5}$$

$$\frac{dm_{bz}e_{bz}}{dt} = -p\frac{dV_{bz}}{dt} - \frac{dQ_{wbz}}{dt} - \frac{dm_{ex}}{dt}h_{ex} + \frac{dm_b}{dt}h_{uz} \tag{3.6}$$

The coupling term between the two zones is $\frac{dm_b}{dt}$, which is the change in burned mass over time due to combustion: it involves a reduction in unburned gases in the unburned zone in favour of an increase in burned gases in the burned zone.

It is evident that, having defined two zones, a different temperature will be obtained for each of them. This contrasts with the hypothesis of uniformity of properties within the control volume, characteristic of the thermodynamic model, but does not affect the validity of the treatment.

The model is completed introducing:

- The gas state law to describe the development of pressure over time:

$$p(t) = \frac{m(t)R(t)T(t)}{V(t)} \tag{3.7}$$

- A model or an experimental heat exchange correlation that allows to calculate the term related to heat loss, such as, for instance, the Woschni correlation;
- A heat release law that allows calculating the terms related to combustion.

Precisely this last point is what differentiates the various combustion modelling approaches. Assigning a trend for the burnt mass variation leads to non-predictive models, calculating this trend on the basis of experimental correlations leads to semi-predictive models, while only calculating this trend on the basis of physical theories this leads to predictive models.

Non-predictive and predictive combustion

A non-predictive combustion model simply imposes a combustion speed depending on the crank angle. This combustion speed will not be dependent on the conditions in the cylinder: it is not influenced by factors such as the residual fraction or injection time. This approach may be appropriate as long as the objective is to study a variable that has little effect on the combustion speed. For example, a model built to study the influence of intake manifold length on volumetric efficiency or a model built to study the acoustic performance of different types of silencers does not require any prediction of combustion speed. In these cases, the variables of interest have a minimal effect on the combustion speed.

However, a non-predictive model cannot be a good choice when the purpose of the model is to study a variable that has a direct and significant effect on combustion speed. In that

case, a predictive or semi-predictive combustion model is the most appropriate choice: the combustion rate responds appropriately to a change in the variable of interest.

In theory, predictive combustion models are an appropriate choice for all simulations. However, there are practical factors that make non-predictive combustion models preferable in certain situations. First, complexity increases computation time; second, predictive models generally require calibration for data measurement in order to provide accurate results. Therefore, a logical strategy would be to implement non-predictive models where appropriate, and to implement predictive models only when required.

Typical combustion model is the Wiebe equation:

$$x_b(\theta) = 1 - e^{-a\left(\frac{\theta-\theta_i}{\theta_f-\theta_i}\right)^m} \tag{3.8}$$

In the equation (3.8), x_b (θ) is the fraction of burnt mass, evaluated for each crank angle by means of an exponential law depending on the starting combustion angle θ_i and the ending combustion angle θ_f.

However, the model does not automatically calculate these two angles, but requires, as input data, the duration of combustion, considered as the time that elapses to pass from 10% (MFB10) to 90% (MFB90) of burned mass, and the angle at which 50% (MFB50) of burned mass is reached, i.e. the centre of combustion. Moreover, the dependence of the burned mass fraction on the angles is also linked to the two constants *a* and *m*, respectively defined as efficiency parameter and chamber factor: the first takes into account the possibility that not all the fuel is burned, preventing the burned mass fraction from reaching the unit value, while the second takes into account the size of the combustion chamber, strongly influencing the combustion speed.

All these parameters can be defined on the basis of experience; however, in order to have an accurate modelling of the combustion process, it would be appropriate to obtain them from a comparison with the experimental analysis. In both cases it is clear that such a model cannot be used during the preliminary stages of the design of a new engine.

As already mentioned, a predictive model must be able to evaluate the combustion speed through a physical description of the combustion itself. The one developed and used in this thesis activity is the fractal model.

Fractal combustion model

The fractal combustion model is based on the two-zone combustion model, previously analyzed, and the characterization of the flame front according to the fractal geometry.

This model is able to describe combustion in all its phases, from incubation to wall combustion, using dedicated equations for each of them. Strictly speaking, these equations would be valid only within the regime of the wrinkled flamelets of the Borghi diagram and under the hypothesis of spherical propagation of the flame front, but, through some corrections, the validity of the model can be extended also to the regime of distributed reactions and for not properly spherical flame fronts.

To the combustion model, is associated the sub-model of turbulence K-k-T, simplification of the more complex three-dimensional model k-ε, with which it is possible to describe the temporal trend of the kinetic energy of the mean field of motion K and the turbulent kinetic energy k.

In this chapter, after a brief introduction on fractal geometry, the flame front will be characterized according to the fractal geometry and then the in-depth description of the fractal combustion model and the turbulence model will be done.

Finally, the models of emission production will be described.

Fractal dimension

The simplest definition of fractal describes it as a geometric figure characterized by the infinite repetition of the same motif, on an increasingly smaller scale, a property that is called self-similarity. This means that, by enlarging the figure, recurring shapes will be found and that with each enlargement it will be enriched with new details.

The term fractal is a neologism created by Benoît Mandelbrot and derives from the Latin *fractus*, or broken/split, and has the same root as the term fractal because fractals do not have a whole dimension.

According to the canons of Euclidean geometry, one is accustomed to define the dimensions of objects through integer numbers: 0 is the size of a point, 1 is the size of a line, 2 is the size of a surface and 3 is the size of a solid. It is difficult to imagine an object with a size of 1.5 or 2.5 that is an object with a non-integer size.

Euclidean geometry allows us to describe simple shapes with a good approximation, while it can be inadequate in the description of complex shapes; a corrugated line, such as the one representative of the Italian coast, is halfway between a line (of dimension 1) and a plane (of dimension 2) and it would be better to describe it through a more appropriate dimension, such as 1.5, called fractal dimension.

Fractal dimension is precisely a fractional dimension, not whole and not necessarily rational, used for the description of objects with a complex shape.

Such objects must have:

- irregularities such as those that cannot be described exhaustively enough with Euclidean geometry

- extension depending on the scale of measurement adopted

- fine structure, i.e. able to have good detail even on very small scales

- self-similarity, i.e. a part of it must be similar to the starting geometry

In reality, just as there are no objects in nature that can be described with Euclidean geometry, in the same way there are no objects that can be described perfectly with fractal geometry, but the approximation that will be made with the latter will be much more accurate than the first.

Koch curve

The Koch curve also known as the Koch snowflake is one of the first fractal curves of which a description is known.

This particular fractal, with a very simple algorithm, is obtained starting from a segment of a given length and operating in the following way:

1. it divides the segment into 3 parts;

2. we delete the central part and replace it with 2 segments forming the sides of an equilateral triangle;

3. the segment is divided with point 1 for each of the current segments.

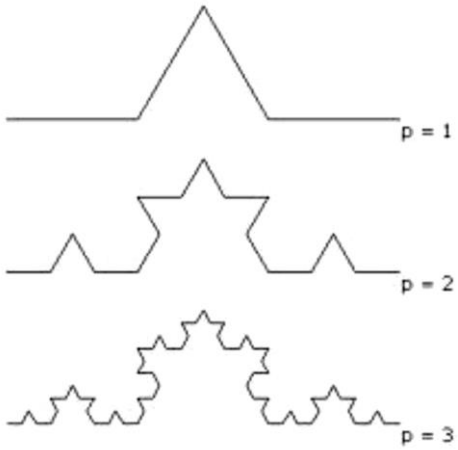

Figure 3.3 – Example of fractal geometry obtained from a simple curve.

In the case of this fractal, it can be noted that, starting from the initial figure, it can be divided into four parts similar to the initial fractal (figure 3.3) and how this property applies at each subsequent enlargement:

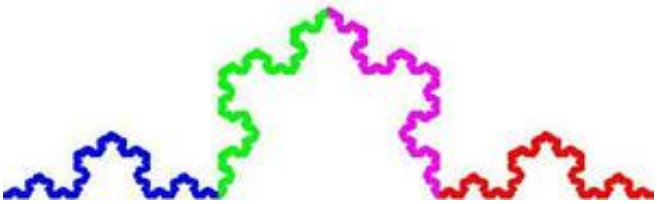

Figure 3.4 – Fractal geometry.

It has come to define, through an extremely simple basic profile, an object of complex geometry with infinite perimeter, but finite area.

In general, a fractal object Γ presents, on a logarithmic plane, an extension L(Γ) that grows linearly as it varies on the scale λ (Figure 3.5) according to the eq. (3.9).

$$L(\Gamma) \propto \frac{1}{\lambda^{D_2-1}} \qquad (3.9)$$

The exponent D_2-*1* is the slope of the curve: as this exponent increases, the growth in length that occurs for a given scale increases; but from this expression it is also clear that the smaller the scale λ, the greater will be the extension L(Γ) of the fractal object. The latter is a characteristic that distinguishes fractals from Euclidean objects: for a Euclidean object, in fact, as the scale with which the measurement is made varies, the same length is always obtained; for a fractal object, instead, its length increases as the scale of length with which it is measured decreases, up to the minimum scale.

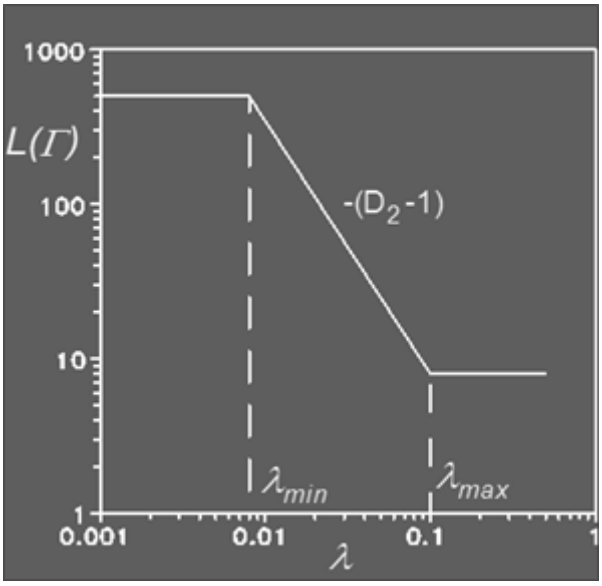

Figure 3.5 – Extension of a fractal object

It should be noted, however, that D_2*-1* means a dimension between one and two, i.e. halfway between a line and a plane (corrugated line), while D_3*-1* will be written in the case of a dimension between two and three, i.e. halfway between surface and volume (corrugated surface); therefore, a more generic expression for the extension of the fractal object is represented by (3.10).

$$L(\Gamma) \propto \frac{1}{\lambda^{[D_i-(i-1)]}} \qquad i = 2,3 \qquad (3.10)$$

The writing D_2*-(2-1)* (or similarly D_3*-(3-2)*) serves to underline the difference between fractal and Euclidean dimensions: representing the slope of the line, it expresses how much the length of the fractal object increases as the scale decreases.

From the mathematical point of view there are no limits for the values that the length scale can assume, but in reality there will be a value of the macroscale λ_{max} above which the extension of the fractal object does not decrease, and a value of the microscale λ_{min} below which the extension does not increase. In other words, with a scale greater than the largest corrugation, or smaller than the smallest corrugation, the extension of the fractal object will no longer vary: for scale values equal to λ_{min}, the fractal object is evaluated with

the best possible resolution, i.e. you will get the maximum extension that takes into account each micro corrugation; for scale values equal to λ_{max}, the fractal object is analysed with the lowest resolution and you can only define the average extension.

This can be expressed mathematically through the (3.11):

$$\frac{L(\Gamma)_{max}}{L(\Gamma)_{min}} = \left(\frac{\lambda_{max}}{\lambda_{min}}\right)^{[D_i-(i-1)]} \tag{3.11}$$

Flame front

Starting from a non-corrugated flame core, such as a small volume of flue gas between the electrodes of the spark plug, generic-shaped vortexes appear which determine macro-corrugations and, as the flame front propagates within the turbulent motion field, micro-corrugations (Figure 3.6 and Figure 3.7).

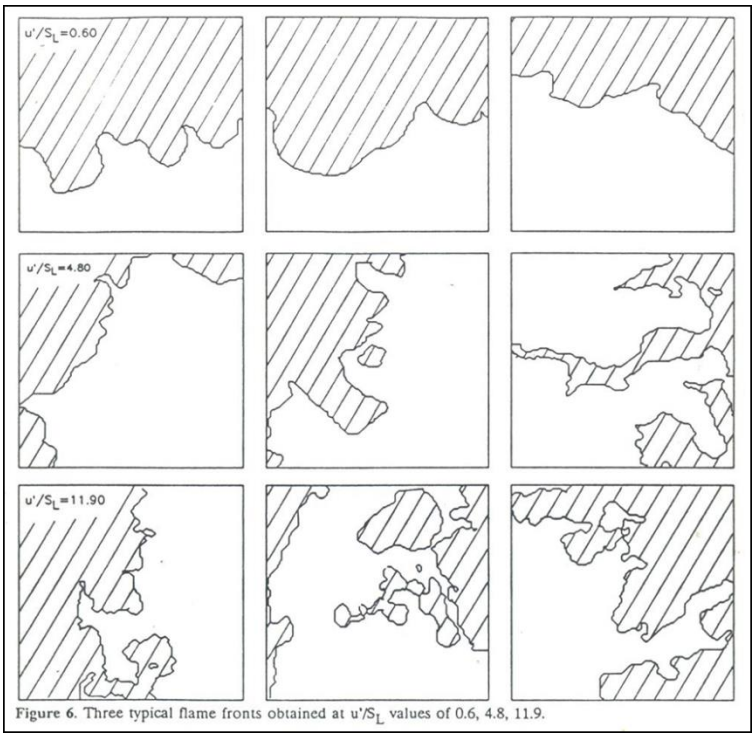

Figure 6. Three typical flame fronts obtained at u'/S_L values of 0.6, 4.8, 11.9.

Figure 3.6 – Typical flame fronts obtained at u'/S_L values of 0.6, 4.8, 11.9.

In order to try to realize the flame front according to the canons of fractal geometry, it is possible to consider a closed polygon (Figure 3.7 a) and go to replace for each side of it a certain basic profile; this last operation must be performed for a high number of iterations, leading to the object in Figure 3.7 d.

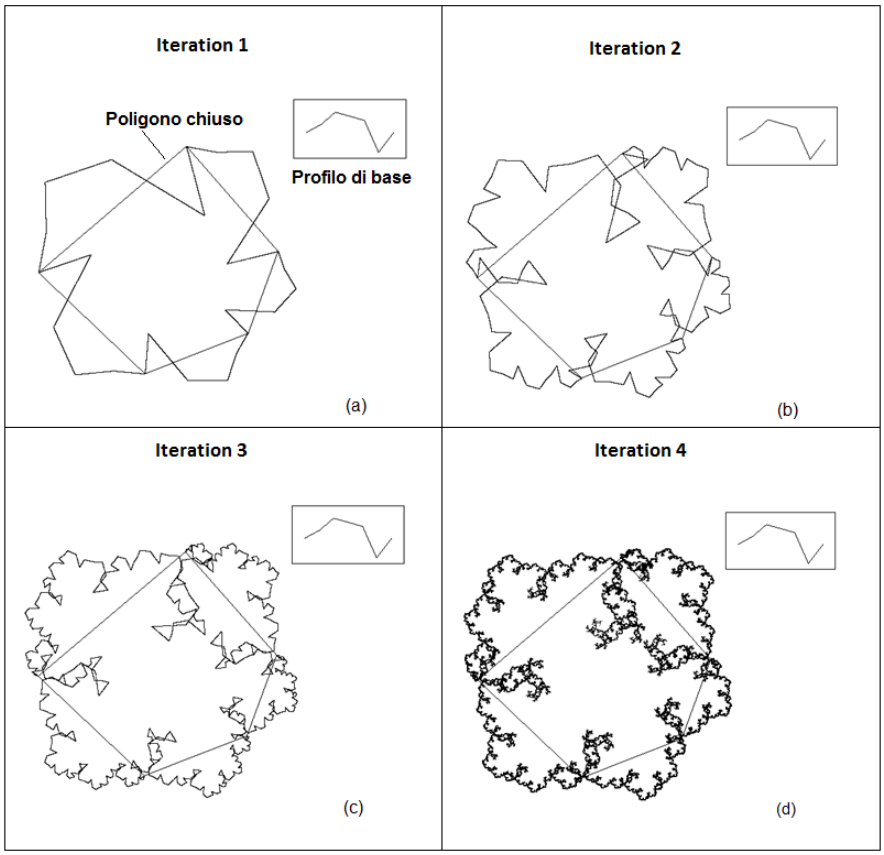

Figure 3.7

This object has a shape very similar to those typical of the flame front, so it seems possible to characterize the latter through fractal geometry.

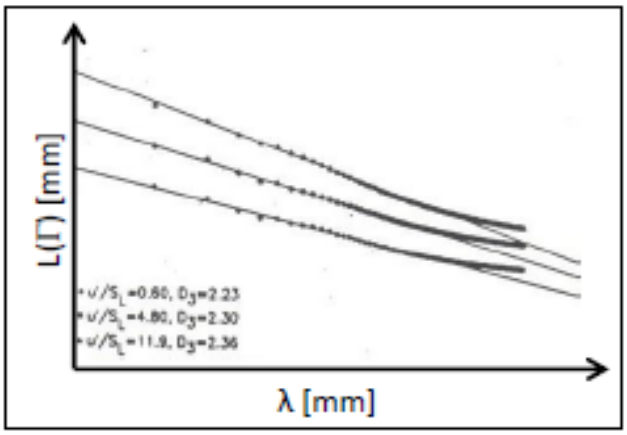

Figure 3.8 - Extension L(Γ) of the flame front in function of the measurement scale λ.

From the analysis with optical engine, with which the results in figure 3.6 have been measured, it is possible to obtain also the trend of the extension L(Γ) of the flame front as a function of the measurement scale λ (Figure 3.8): in spite of the different values of the turbulent intensity, the three trends of L(Γ) are analogous and all of them tend to flatten for high values of the measurement scale; moving towards lower values of the measurement scale, we can also see that the extension of the flame front increases logarithmically as a function of the scale. Once reached low values of the measurement scale, it is expected that L(Γ) tends to surface again, but this does not occur in the experimental analysis because the resolution is not high enough. The agreement between the experimentally calculated trend (figure 3.8) and the theoretical trend of figure 3.7, shows the possibility to characterize the flame front as a fractal object.

Flame front characterization

Having ascertained that the flame front can be considered as a fractal, for its characterization it is sufficient to define λ_{max}, λ_{min} and D_3: for the first two terms turbulence scales will be used, while for the third one an experimental relationship will be used.

λ_{max} allows the fractal object to be analysed with minimum resolution, that is without any information on the corrugations; for the flame front, a macroscale of turbulence is then defined with which, considering no corrugations, the front is considered spherical and its surface is equal to the laminar flame area.

λ_{max} is related to a macroscopic characteristic dimension of the flame front, here assumed proportional to the flame radius, r_f, by the tuning constant c_{wrk} (wrinkling multiplier).

$$\lambda_{max} = c_{wrk} r_f \tag{3.12}$$

λ_{min} instead allows to analyse the fractal object with the highest resolution, that is without losing information even on the smallest of the corrugations; a microscale of turbulence is then defined, with which you can evaluate the turbulent flame area. λ_{min} is commonly taken equal to the size of the smallest turbulent eddy [26], expressed by the Kolmogorov length scale, η.

D_3 is finally defined through the experimental relationship (3.13) in which the dependence on the turbulent intensity u' and on the laminar speed of flame S_L is explained.

$$D_3 = \frac{2.35u' + 2.00S_L}{u' + S_L} \tag{3.13}$$

Combustion model

The fractal model considers the corrugated flame front, characteristic of a turbulent propagation, but locally propagating at laminar speed (Figure 3.9).

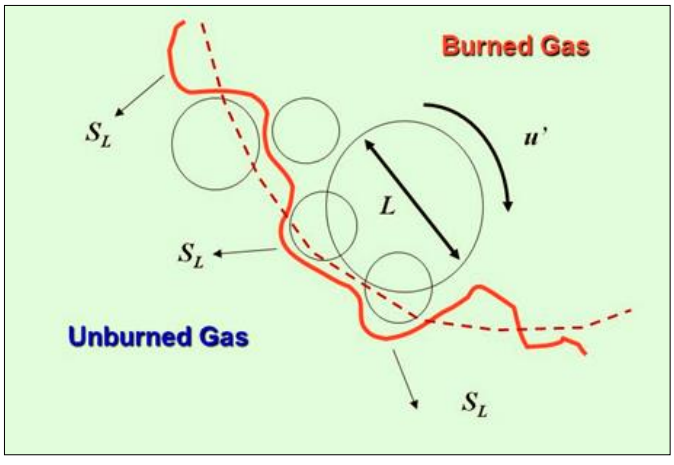

Figure 3.9 – Fractal model: the corrugate flame front propagates at laminar speed locally.

The combustion speed is expressed as follows:

$$\frac{dm_b}{dt} = \rho_u \left(\frac{A_T}{A_L}\right) A_L S_L \qquad (3.14)$$

However, in order to have a predictive combustion model, it is necessary to rewrite the term (A_T/A_L) according to what has just been said for the characterization of the flame front through the fractal geometry.

Summarizing:

λ_{min}= Kolmogorov scale (η)

$\lambda_{max}=c_{wrk}\ r_f$

L(Γ)max=A_T or equal to the turbulent flame area

L(Γ)min=A_L or equal to the laminar area of flame

D_3 function of u' and S_L according to (3.13).

On the basis of these data, it is possible to rewrite the (3.11) as follows:

$$\frac{A_T}{A_L} = \left(\frac{\lambda_{max}}{\lambda_{min}}\right)^{D_3-2} \qquad (3.15)$$

Explaining all the terms and introducing the relationships for Kolmogorov's scale and for the turbulent Reynolds number (3.16), we get the (3.17).

$$\eta = \frac{L_I}{Re_t^{3/4}} \qquad Re_t = \frac{u' L_I}{\nu} \qquad (3.16)$$

$$\frac{A_T}{A_L} = \left(\frac{c_{wrk} r_f}{L_I^{1/4} \nu^{3/4}} u'^{3/4} \right)^{\frac{2.35u' + 2.00S_L}{u' + S_L} - 2} \tag{3.17}$$

This writing highlights the need to calculate u' and L_I in order to correctly define the ratio between turbulent area and laminar area of flame.

Finally, replacing the (3.17) in the (3.14), we get the (3.18).

$$\frac{dm_b}{dt} = \rho_u \left(\frac{c_{wrk} r_f}{L_I^{1/4} \nu^{3/4}} u'^{3/4} \right)^{\frac{2.35u' + 2.00S_L}{u' + S_L} - 2} A_L S_L \tag{3.18}$$

This is the equation of the fractal combustion model in the case of fully developed combustion.

The laminar area A_L is determined geometrically: the flame front is assumed as a smooth spherically-shaped surface and its area is computed by an automatic procedure implemented in a CAD software capable of processing the actual 3D geometry of the combustion chamber.

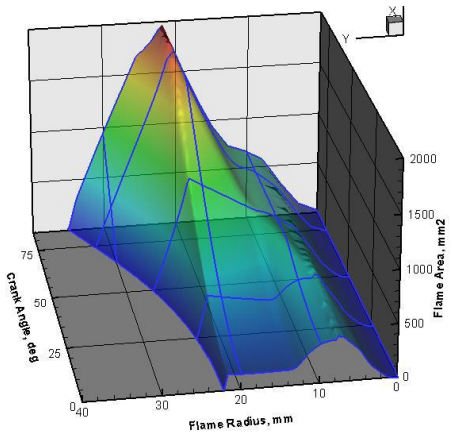

Figure 3.10 – Example of laminar area

The laminar speed, on the other hand, is essentially a function of the type of fuel, the air/fuel ratio and the residual gas fraction.

Its unstretched value can be defined experimentally by considering a transparent tube (Figure 3.11) within which a stationary combustion process takes place, at reference pressure and temperature values.

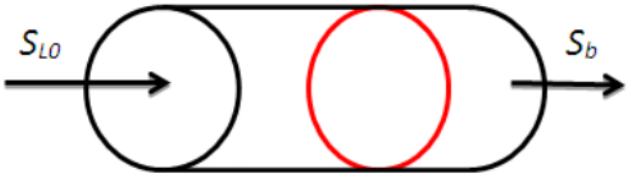

Figure 3.11 – Experimental schematization to define S_L

Once the equivalence ratio $\varphi=\alpha_{st}/\alpha$ is fixed, the speed of the reagents is varied until the flame stops. Repeating the experiment for different values of φ, the value of S_{L0} is obtained, i.e. the laminar speed unstretched relative to a planar flame front.

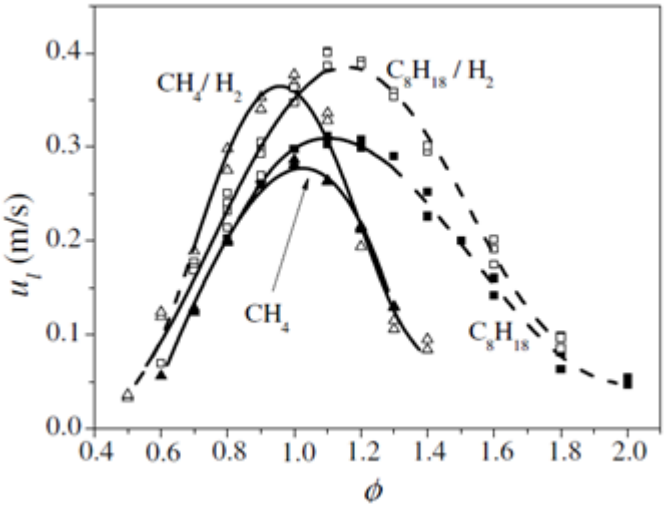

Figure 3.12 – S_{L0} for different fuels.

Referring to the diagram of figure 3.12, it can be seen that at most the laminar speed unstretched assumes values equal to 30-40 cm/s. Assuming then that the flame front must cover about 5 cm inside the combustion chamber, the time needed to cross the chamber would be 0.167 s. Considering then that at the rotation speed of 1000 ERPM, the angular

duration of the combustion is 40°, the whole process will last at most 0.0067 s. This means that the laminar combustion is so slow that it cannot complete even at the minimum speed.

Laminar combustion speed S_L

The laminar flame speed, S_L, in eq. (3.18) is evaluated by a general developed correlation, that explicitly considers the water content in the unburnt mixture. This correlation is the result of the fitting process of laminar flame speed outcomes from a chemical kinetic solver (CHEMKIN) applied to the computation of 1D laminar flames. The gasoline is modelled by a Toluene Reference Fuel (TRF), composed of iso-octane, n-epthane and toluene. The volume fractions of the three components of the surrogate fuel are selected so as to match the RON and MON of the actual gasoline [27]. Different oxidation mechanisms for gasoline surrogates are available in the current literature, ranging from simplified [28] to semi-detailed [29] and detailed kinetics [30]. They are characterized by an increased number of species and reactions, and hence by growing computing times. Since the development of a quite general correlation requires a large number of flame speed data (more than 3000 evaluations), a compromise between accuracy and computational effort is mandatory. For this reason, it was decided to use the semi-detailed mechanism developed by Liu et al. [29], which handles both low and high temperature kinetics, and includes 5 elements, 56 species and 168 reactions. The computation of S_L was performed for several values of pressure, p, temperature, T, equivalence ratio, $\Phi=1/\lambda$, RON, MON, EGR mass fraction, x_r, and water mass fraction, x_w, in the following ranges:

- Pressure, p: 1 – 10 bar
- Temperature, T: 323 – 473 K
- Equivalence ratio, Φ: 0.7 – 1.6
- RON: 80 – 100
- MON: 74 – 94
- EGR mass fraction, xr: 0 – 0.25
- Water mass fraction, xw: 0 – 0.1

The composition of the recirculated exhaust gas was computed in each condition (TRF blend, Φ, T, p) as the equilibrium composition of the combustion products (6 species). The

values of S_L computed by CHEMKIN were fitted by a function of Φ, *T*, *p*, *xr*, *xw*, and TRF composition. Preliminary tests showed that, in the considered ranges of RON and MON, the laminar flame speed mainly depends on the fuel sensitivity, S=RON-MON, rather than on the specific TRF blend. This resulted in a strong simplification of the data fitting procedure and led to the following correlation:

$$S_L = S_{L0}\left(\frac{T}{T_{ref}}\right)^{\alpha}\left(\frac{p}{p_{ref}}\right)^{\beta}(1-\kappa x_r)^{\gamma}(1-\chi x_w) \qquad (3.19)$$

Where:

$$\begin{aligned} &S_{L0} = A + B\phi + C\phi^2 + D\phi^3 + E\phi^4 \\ &A = a_1 + a_2 S\,, \quad B = b_1 + b_2 S\,, \quad C = c_1 + c_2 S \\ &D = d_1 + d_2 S\,, \quad E = e_1 + e_2 S \\ &\alpha = \alpha_1 + \alpha_2\phi\,, \quad \beta = \beta_1 + \beta_2\phi \\ &\gamma = \gamma_1 + \gamma_2\phi\,, \quad \delta = \delta_1 + \delta_2\phi \end{aligned} \qquad (3.20)$$

The values of the 20 coefficients in Equation (3.20) that provide the best fitting of the flame speed data are reported in Table 2. The average fitting error is 2.2% and the maximum error is 6.0%.

a_1	101.7068	α_1	1.388656
a_2	-16.80694	α_2	0.3742516
b_1	-777.2416	β_1	-0.3952267
b_2	76.07949	β_2	0.1766350
c_1	1763.747	γ_1	1.311202
c_2	-125.1039	γ_2	0.6858792
d_1	-1360.444	κ	1.538489
d_2	84.03323	δ_1	1.264575
e_1	340.6086	δ_2	1.169524
e_2	-19.61888	χ	1.961413

Table 3.1 – Coefficient for the laminar flame speed correlation.

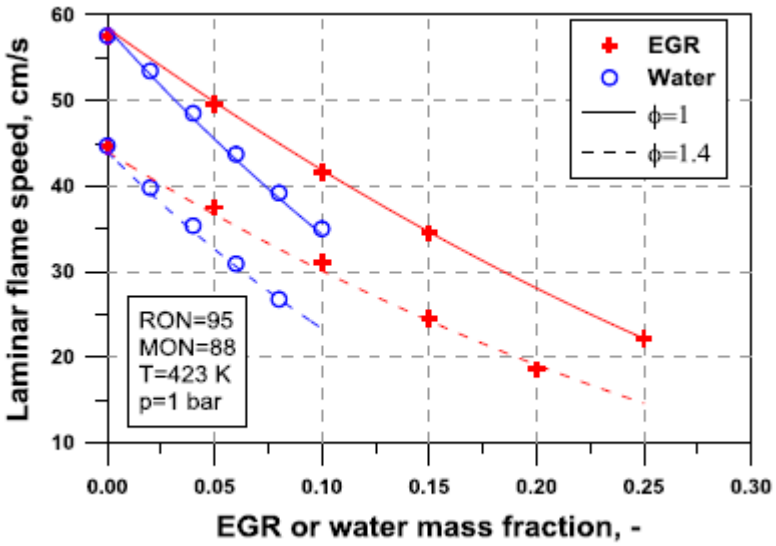

Figure 3.13 - Sensitivity of the laminar flame speed to the addition of water or exhaust gas to the unburnt mixture. Symbols: CHEMKIN data. Lines: present correlation.

The proposed correlation separates the effects of the water addition from those of other diluents. The importance of such refinement is highlighted in Figure 3.13, which shows the variations in the laminar flame speed with EGR and water mass fractions, for two equivalence ratios, and fixed values of RON, MON, T and p. It can be observed that water causes a stronger decrease in the flame speed than EGR, up to about 40% for x_w=0.1.

Laminar and wall combustion

The above described fractal model actually applies for a fully developed and freely expanding turbulent flame. During both early flame development and combustion completion, proper modifications are required. At the combustion beginning, the flame front is not effectively corrugated by the turbulence, while at the end of the process, it is characterized by a progressive interaction with the walls. The combustion is assumed to start with a purely laminar propagation. The transition from laminar to turbulent combustion is then described by a progressive increase of the fractal dimension D_3, according to (3.21) and (3.22).

$$D_3 = \frac{D_{3,max}u' + D_{3,min}S_L}{u' + S_L} \tag{3.21}$$

$$D_{3,min} = 2.00 \qquad D_{3,max} = 2.00(1 - w_{trans}) + 2.35w_{trans} \tag{3.22}$$

The variable w_{trans} in eq. (3.22) handles the evolution of the wrinkling process, as a function of a characteristic time scale, t_{trans}.

$$w_{trans} = \int \frac{dt}{c_{trans}t_{trans}} \tag{3.23}$$

where c_{trans} (transition multiplier) is a tuning constant of the model. The characteristic time scale is computed as:

$$t_{trans} = \frac{k}{\varepsilon} \tag{3.24}$$

where k is the turbulence kinetic energy, and ε is its dissipation rate. When the flame front interacts with the combustion chamber walls, another modification of the burning rate has to be introduced. Although a detailed description of flame-wall interaction is far beyond the possibility offered by a quasi-dimensional model, it can be argued that flame front wrinkling no more occurs near the walls, and the burning rate slows down. The overall burning rate is hence expressed as a weighted average between a purely fractal burning rate and a laminar wall combustion, according to (3.25) and (3.26).

$$\frac{dm_b}{dt} = (1 - w_{wall})(\frac{dm_b}{dt})_{fract} + w_{wall}(\frac{dm_b}{dt})_{wall} \tag{3.25}$$

$$(\frac{dm_b}{dt})_{wall} = \rho_u A_L S_L \tag{3.26}$$

The progress variable w_{wall} defines the transition from turbulent to wall combustion through the ratio between the area wetted by the flame front on piston, head and cylinder, A_w, and the total flame front area, A_{tot}. This ratio is multiplied by the mass fraction of burned gas, x_b, raised by an exponent which is amplified by the tuning constant x_{wc} (wall combustion multiplier).

$$w_{wall} = \frac{A_w}{A_{tot}} {x_b}^{10x_{wc}} \tag{3.27}$$

Turbulence Model

In order to correctly apply the fractal combustion model, it is necessary to calculate the turbulent intensity u' and the integral length scale L_I; and this can in principle be done through computational fluid dynamics (CFD) analysis.

With the CFD analysis, in fact, it is possible to solve the Reynolds – averaged Navier-Stokes equations on an arbitrarily defined three-dimensional domain, in order to obtain the description of the mean field of motion, i.e. the velocity magnitude, U_{flow} (Figure 3.14), and the description of the turbulent motion field; for the latter, since it is necessary to guarantee the closure of the system of equations as already said in the previous chapter, we introduce the turbulence model k-ε, which allows to describe the turbulent kinetic energy, TKE, and the dissipation rate, ε (Figure 3.15).

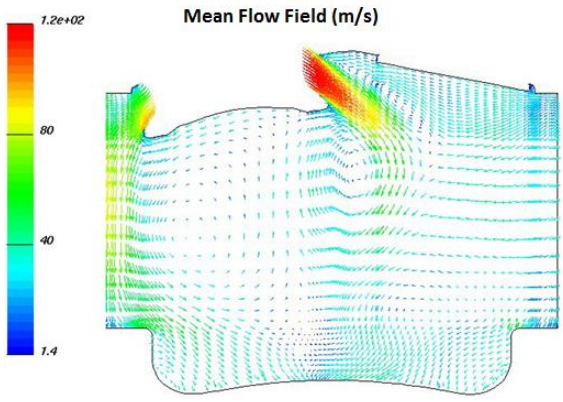

Figure 3.14 - Velocity magnitude.

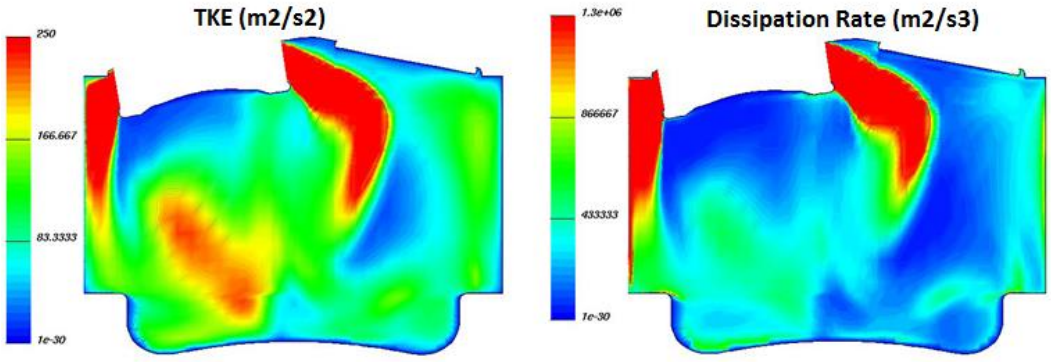

Figure 3.15 - Turbulent kinetic energy and dissipation rate.

It is clear from the images that the results obtained from a numerical analysis of this type are a function of time and space, that is for each of the calculated quantities, for each instant of time, you will have three spatial components. However, since these data must be introduced in the fractal model, which schematizes the cylinder with a zero-dimensional domain, it is necessary to renounce to the spatial dependence for all the properties and assume that they are homogeneous and isotropic.

For this reason, all the properties obtained from the CFD analysis are therefore mediated in space, so as to obtain for each of them a trend that varies only according to the crank angle (figure 3.16).

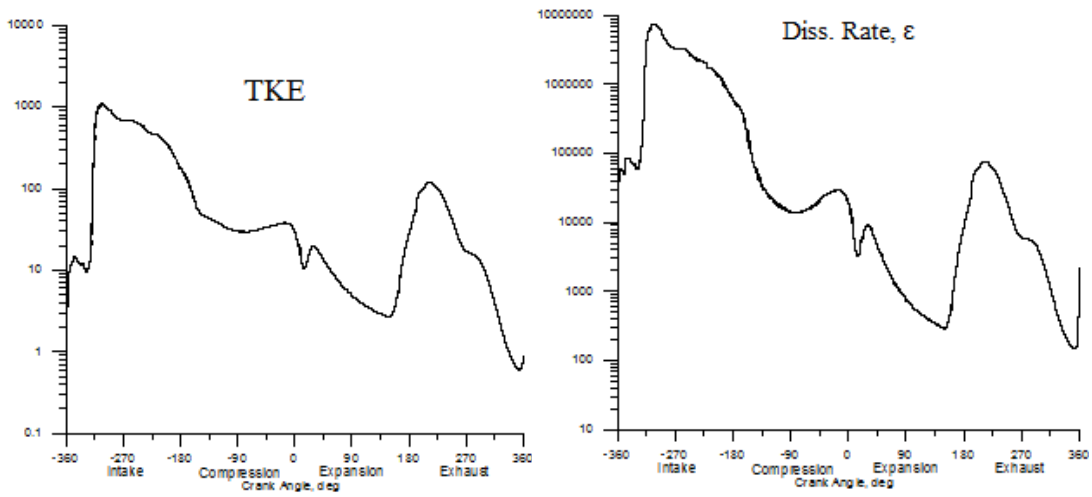

Figure 3.16 – TKE and dissipation rate spatially averaged.

At this point, to evaluate u' and L_I, the following equations can be adopted, respectively.

$$TKE = \frac{3}{2}u'^2 \tag{3.28}$$

$$\varepsilon = 0.09^{3/4}\frac{TKE^{3/2}}{L_I} \tag{3.29}$$

The (3.28) makes explicit that turbulent kinetic energy is given by the sum of the contributions of kinetic energy along the three directions, which however are equal to each other for the hypothesis of homogeneity and isotropy; the (3.29) instead is a constitutive relation of the K-ε model, which relates the length of the integral scale, the turbulent kinetic energy and the dissipation rate.

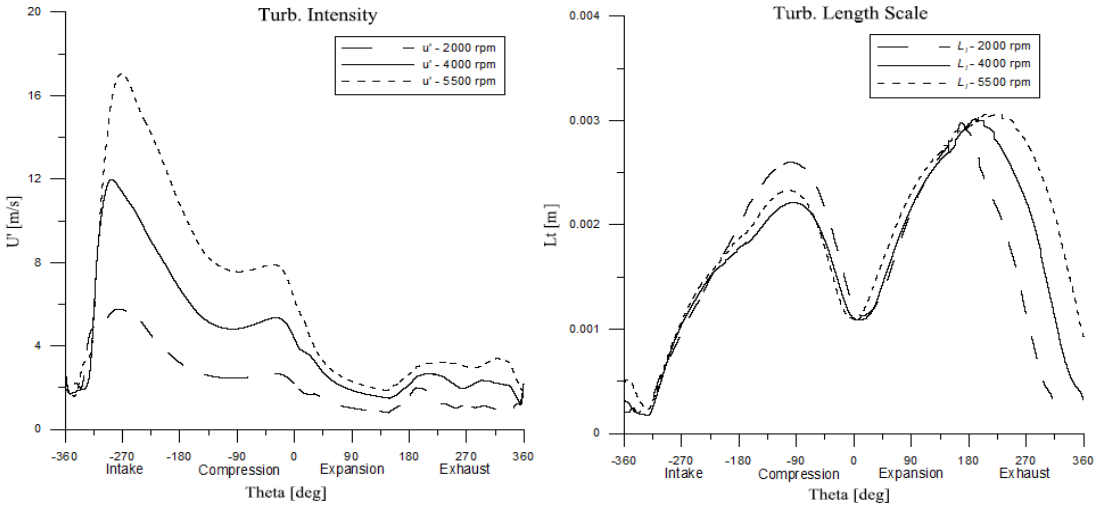

Figure 3.17 – Turbulent intensity and integral length scale from 3D CFD analysis.

The results of figure 3.17 show how the turbulent intensity varies considerably as the speed varies, while the integral length scale remains almost constant as the speed varies.

K-k-T model

The adopted turbulence model is comprehensively described and validated in [26] and [31]. It includes the balance equations of turbulent kinetic energy, k, mean flow kinetic energy, K, and tumble angular momentum, T. These parameters are defined as:

$$K = \frac{1}{2} U_{flow}^2 \tag{3.30}$$

$$k = \frac{3}{2} u'^2 \tag{3.31}$$

$$T = U_t r_t \tag{3.32}$$

where u' is the turbulence intensity, U_{flow} is the mean flow velocity, U_T is the tumble velocity and r_T is the radius of the tumble vortex. The k equation derives from the 3D RNG *k*- ε turbulence formulation, which, synthesized in a phenomenological framework, leads to:

$$\frac{dmk}{dt} = (\dot{mk})_{inc} - (\dot{mk})_{out} + \frac{2}{3}\frac{\dot{\rho}}{\rho}\left(-m\nu_t \frac{\dot{\rho}}{\rho} + mk\right) + P - m\varepsilon \tag{3.33}$$

where ν_t is the turbulent viscosity:

$$\nu_t = c_\mu \frac{k^2}{\varepsilon} \tag{3.34}$$

The balance equations of mean flow kinetic energy and tumble momentum look like:

$$\frac{dmK}{dt} = (\dot{mK})_{inc} - (\dot{mK})_{out} - f_d \frac{mK}{t_T} + mK\frac{\dot{\rho}}{\rho} - P + \dot{K}_{inj} + \dot{K}_p \tag{3.35}$$

$$\frac{dmT}{dt} = (\dot{mT})_{inc} - (\dot{mT})_{out} - f_d \frac{mT}{t_T} \tag{3.36}$$

The first and the second terms in equations (3.33), (3.35) and (3.36) describe the incoming and outcoming convective flows through the valves. Incoming fluxes are modulated by dedicated tuning constants, named c_{Kin0} and c_{Tin0}, for *K* and *T*, respectively, while no valve

flow contribution is considered in the turbulent kinetic energy equation. The third term in equations (3.35) and (3.36) expresses the decay due to the shear stresses with the combustion chamber walls. To model this effect, a decay function, f_d, and a characteristic time scale, t_T, are introduced:

$$f_d = c_{fd0} + c_{fdm}[\max\left(\frac{B}{H}, 1\right) - 1] \tag{3.37}$$

$$t_T = \frac{r_T}{u'} \tag{3.38}$$

The decay function only depends on the instantaneous geometrical dimensions of the combustion chamber. It is built to be particularly high near the TDC, where the tumble vortex collapse is expected to occur. The parameters c_{fd0} and c_{fdm} are tuning constants: the former is active all over the engine cycle, and represents an offset introduced to consider the tumble and kinetic energy dissipations due to internal viscous forces. The above offset allows to improve the tumble prediction around the BDC. c_{fdm} parameter is a multiplier utilized to adjust the intensity of the tumble collapse.

Coherently with the k formulation, the K equation includes an additive compressibility term, mK ρ⁄ρ, and a subtractive turbulent production term, P, expressing the energy cascade mechanism. The latter quantity is related to the difference between the overall mean flow kinetic energy, K, and the one associated to the tumble motion, $K_T=U_T^2⁄2$, according to:

$$P = c_{pKk} m \frac{K - K_T}{t_T} \tag{3.39}$$

c_{PKk} being a model constant, modulating the energy transfer from the mean flow to the turbulent one.

The turbulence integral length scale is not directly modeled, but its evolution during the engine cycle is described by a sequence of S-shaped functions. It is assumed to not

change with the engine operating conditions. The dissipation rate, $\boldsymbol{\varepsilon}$, needed to integrate the k equation, is calculated by:

$$\varepsilon = c_{\mu}{}^{3}/_{4}\frac{k^{3/2}}{L_I} \tag{3.40}$$

The tumble radius is assumed as a pure geometrical parameter, not depending on the operating conditions. It is specified by a simple formulation:

$$r_T = c_{rT0} + c_{rTm}\frac{1}{4}\sqrt{B^2 + H^2} \tag{3.41}$$

c_{rT0} and c_{rTm} being two adjustable constants.

Emission model

The model also includes an estimation of the emissions namely CO, HC and NO. The model for the evaluation of CO and NO concentrations is based on a multi-zone schematization of the burned zone. A temperature stratification is supposed, where each burned parcel is assumed to compress/expand adiabatically according to the in-cylinder pressure. In each burned parcel, the CO and NO concentrations are computed starting from the equilibrium one and applying a simplified chemical kinetics. For the NO, the extended Zeldovich model is applied, whereas the CO variations are computed by a single-step reaction scheme [**Error! Reference source not found.**].

Concerning the HC modeling, the literature proposes various formation mechanisms, such as the adsorption/desorption from the oil layer, wall flame quenching and crevices. Among those mechanisms, in this work, the HC production is estimated by a very simplified methodology, where only the opposing effects of crevices HC release and thermal oxidation are considered. The unburned hydrocarbons are assumed to accumulate (be released) during the pressure rise (decrease) phase in (from) an arbitrary assigned constant volume. It is assumed to be representative of the crevices in the combustion

chamber, where the flame front extinguishes. In this volume, the temperature is considered the same as the wall one, while the pressure is supposed equal to the cylinder one. The mass (or moles) released in each time step is computed by the universal gas law, assuming a gas composition equal to the unburned mixture. The unburned hydrocarbons emanated from the crevices are assumed to burn with an oxidation rate determined by the empirical correlation proposed in [39]. This depends on the HC and molecular oxygen concentrations and on the temperature. The oxidation temperature is computed as a weighted average between the in-cylinder mean gas temperature and the wall temperature.

4. Experimental setup and tests

The experimental testing was conducted with a Lamborghini V12 naturally aspirated engine at the testing department of the Automobili Lamborghini S.p.A.

Figure 4.1 - Engine V12 Lamborghini.

The considered engine is a high performance naturally aspirated V12-cylinder PFI SI unit, whose main characteristics are summarized in table 4.1. Each cylinder presents a conventional pent-roof architecture of the combustion chamber and is fitted with a centered spark-plug, a standard ignition system and four valves. The latter are controlled by unphased VVT devices. The intake pipe network presents some valves which allow to couple/decouple the intake air paths. In this way, cylinder filling is optimized according to the engine speed, employing the wave dynamic effects. A muffler is installed along the exhaust line, which can be disabled by an additional flap valve. The main engine specifications are listed in table:

12-cylinder VVT Naturally-Aspirated PFI Engine	
Compression ratio	11:8:1
Displaced volume, cm^3	541.54
Bore, mm	95
Stroke, mm	76.4
Connecting rod length, mm	145.8
Maximum brake power, kW	566.6 @ 8500 rpm
Maximum brake torque, Nm	720.0 @ 6750 rpm
Valve number	4 valve/cylinder

Table 4.1 – Engine main characteristics.

The pressure measurements were carried out as follows:

- for the cylinder a Kistler A6045 B pressure transducer was flush-mounted in the combustion chamber side roof;
- sampling was performed via Kistler charge amplifiers and a AVL combustion analysis system at a resolution of 0.1 CAD;
- for the dynamic intake and exhaust gas pressures, Kistler 4045 A5 pressure transducers were chosen and data were sampled with a resolution of 1 CAD.

In total, 500 consecutive cycles were collected for each operating point. An ensemble average of these cycles has been considered for the comparison with the model.

Measurements of static pressures and temperatures were performed with conventional pressure transducers and thermocouples during an averaging interval of 30 s. Oil and water conditioning systems allowed for steady-state operations.

The engine has been investigated in two conditions: with the standard lambda map and with lambda = 1 in all engine operation points, in according to EU7 direction. For the standard lambda map the fuel is metered to realize a stoichiometric air/fuel mixture at low speeds (up to 4000 rpm). At higher speeds, the mixture is progressively enriched to favorite the drivability and to limit the exhaust temperature. The spark advance is generally set to ensure engine operation at maximum brake torque. Only at low speeds and high loads it is delayed to avoid knocking combustion. The VVT devices are controlled so as to maximize the torque at full load. At decreasing load, the valve timing is modified to increase their overlapping. In this way, the internal EGR is promoted, reducing the need for intake throttling.

Under λ=1 strategy the exhaust manifold was without insulation in order to reduce the temperature on the catalyst element and the limit temperature on the brick catalyst was increased from 880°C to 1050°C. The same expedients were adopted on the engine model.

For the analysis of pollutant emissions, an AVL i60 AMA 4000 system is employed. Integrated pumps draw in the measurement gas from sample points. The analysis of the gas is performed using high-end analyzers – FID for THC, CLD for NO/NOx, IRD for CO. After several correction steps, the raw values of the analyzers provide pollutant concentrations, which are transmitted to a test cell automation system.

Engine model description

The engine, in all its geometries, was first schematized in the GT-Power™ software. In figure 4.2 we can appreciate the main macro blocks that constitute it: the intake manifold synthesized, starting from the external environment, with a series of volumes and pipes; the six cylinders (one bank) that constitute the engine with the linked direct injectors; the exhaust manifold given by the primary and secondary exhaust, the catalysts and the silencer, that flows into the external environment; and the crankshaft.

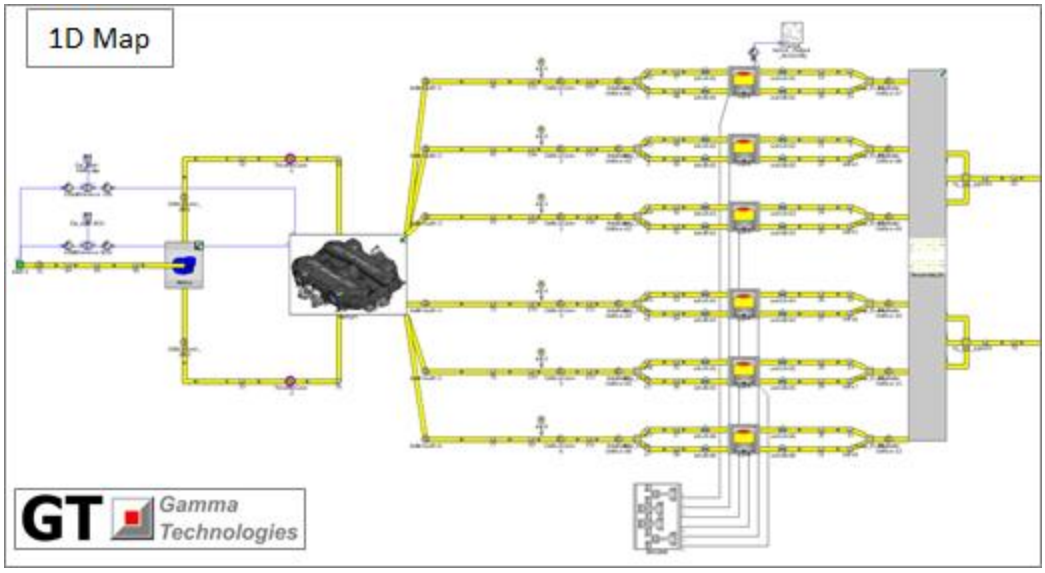

Figure 4.2 – Engine schematization in GT Power environment.

To reduce the calculation effort, the engine has been reduced at one bank thanks to perfect symmetry between the banks.

Turbulence validation

The first stage of the model tuning is the identification of the constants for the turbulence sub-model, according to a hierarchical 1D/3D methodology.

To this aim, preliminary in-cylinder 3D CFD simulation were carried out for a speed of 7000 rpm under motored conditions. Time-varying boundary conditions at the intake and exhaust ports are derived from 1D simulations.

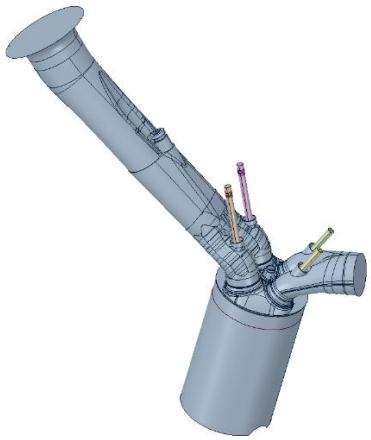

Figure 4.3 – Combustion system and in/ex ducts for 3D CFD analysis.

Figure 4.4 depicts a comparison between the turbulence intensity computed by the 0D model and the one resulting from the mass-averaged turbulence intensity field in the 3D model, at each crank angle. 3D analyses provided data just before the FTDC, but the agreement close to the firing TDC is very satisfactory. Here the typical turbulence speed-up, due to the collapse of the tumble motion, occurs.

For the turbulence model closure, the integral length scale, L_I, has to be estimated. To this aim, no refined formulation is employed, but this parameter is described by a simplified methodology. L_I is specified by a sequence of S-shaped curves. The related 0D/3D assessment is shown in figure 4.4.

The 0D model accuracy is quite satisfactory, especially near the TDCF, when the combustion takes place.

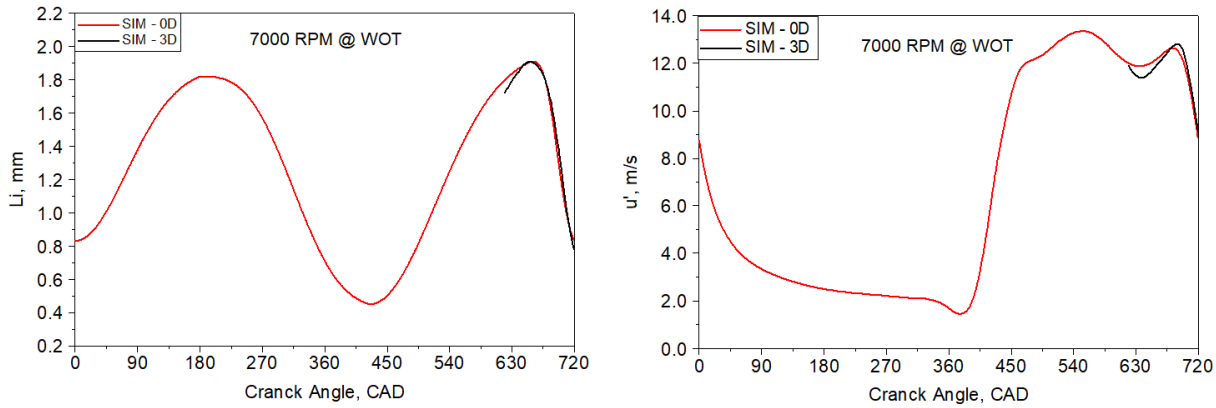

Figure 4.4 - Numerical 1D/Numerical 3D assessment.

Engine Model validation at Full Load

For the full load analysis, the experimentally actuated λ and valve timing are imposed as input data in the simulations. The positions of the intake/exhaust flap valves are assigned according to the experiments, as well. The throttle valve is assumed fully opened. The spark advance is not directly imposed, but it is identified by an automatic controller implemented in the combustion model which targets the measured MFB50 (figure 4.6). In detail two levels of lambda are investigated (figure 4.5).

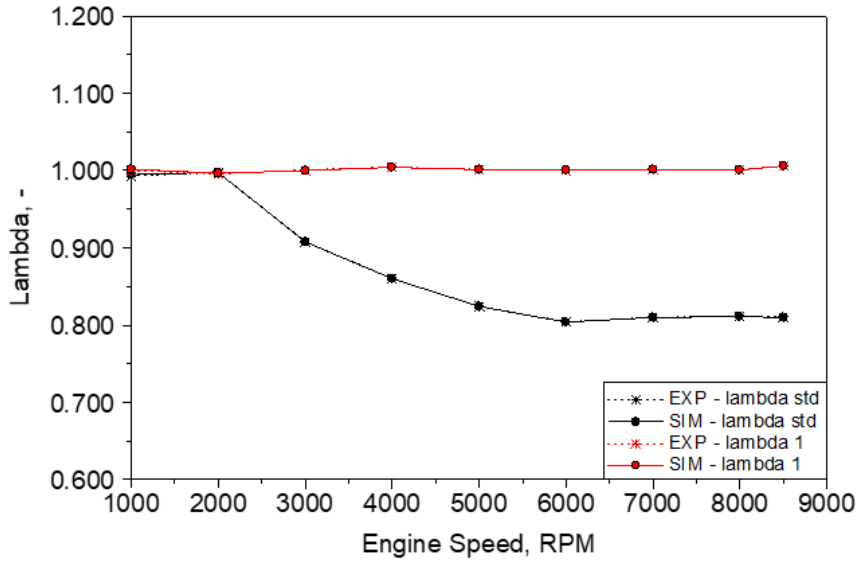

Figure 4.5 – Lambda values @ WOT.

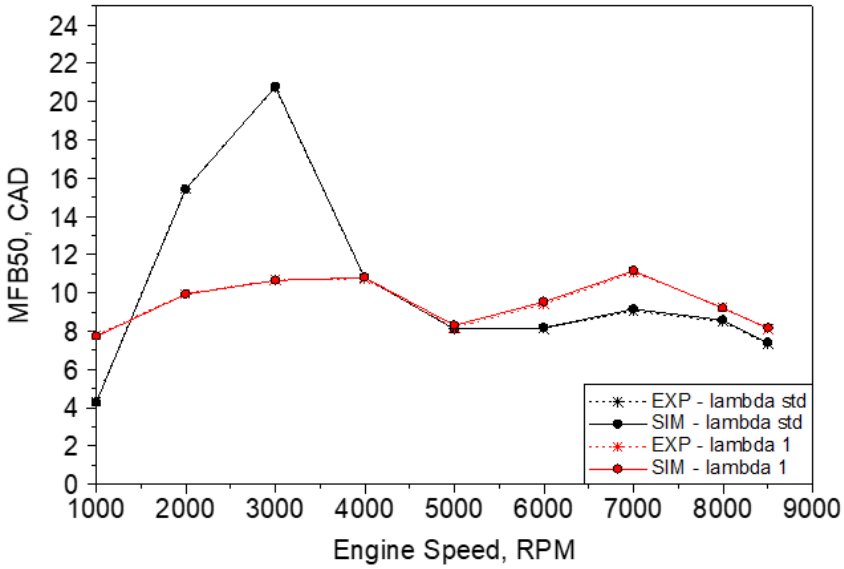

Figure 4.6 – MFB50 values @ WOT.

As clarified in the previous paragraph, the experimental combustion is phased to reach the maximum brake torque, considering the knock limit. The figure 4.6 shows that above the 4000 RPM the results are similar: the enrichment is not necessary to mitigate the knock phenomena and also with a stoichiometric mixture the MFB_{50} reaches the best value in term of efficiency (8-10 CAD). Only the point at 7000 RPM WOT is slightly limited

from knock. Under 4000 RPM, the results present an irregular trend. The reason of this trend is the smoothing of torque curve for the lambda standard setting (black curve).

These two parameters are inputs of the simulation; this is the reason why the model perfectly matches the experimental counterparts.

As a first verification of the model consistency, in figure 4.7 the numerical/experimental comparison of the BMEP, BSFC, Air Flow Rate and in-cylinder peak pressure are shown. Most of the points lie in the error bands of ± 5%, denoting the good accuracy in the engine geometry schematization and in the combustion/turbulence modeling. Some errors concern the BSFC predictions, which are probably due to the inaccuracies in heat transfer modelling. The errors for most points are below 5% for this parameter, as well.

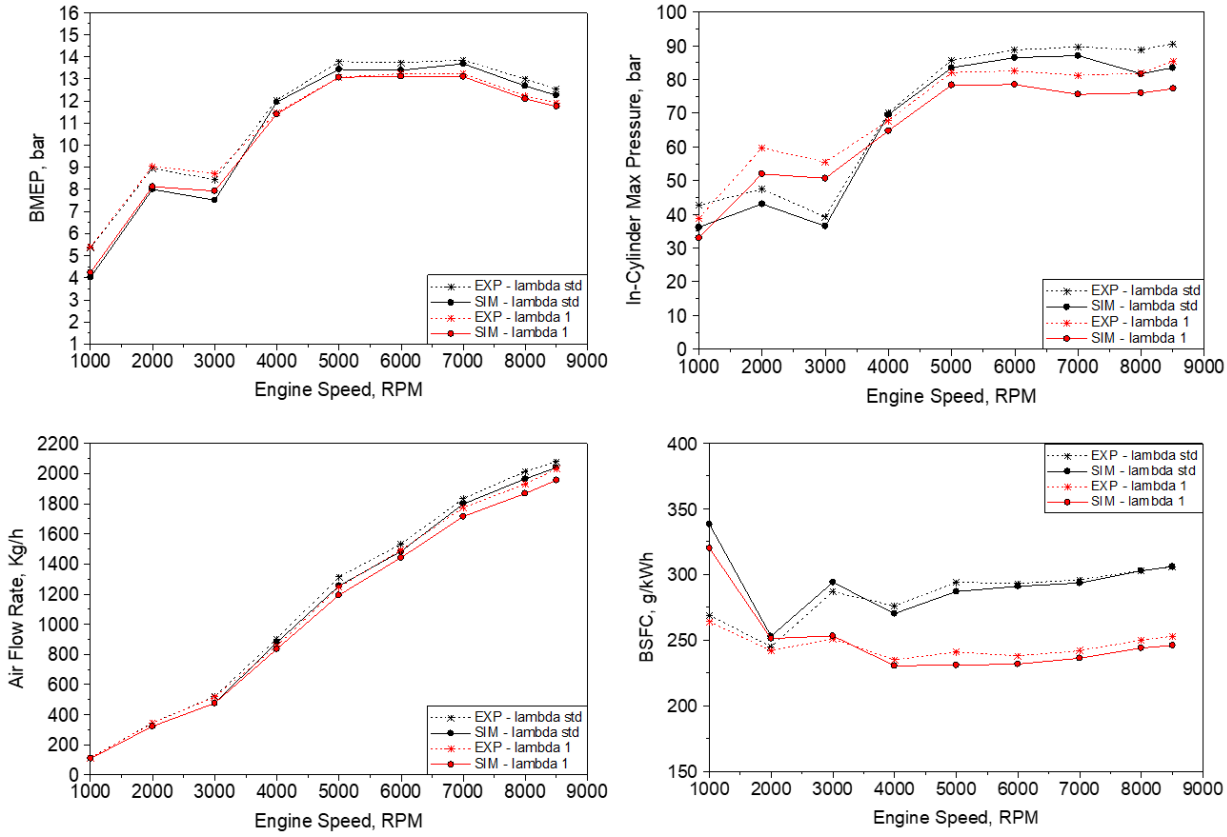

Figure 4.7 – Experimental/Numerical assessment for BMEP, BSFC, Air flow Rate, In-cylinder peak pressure.

The figure 4.8 shows the BSFC delta percentage between the different lambda settings. The reference is the BSFC with rich mixture and for this reason the values are negative.

The numerical/experimental comparison is quite satisfactory, only at 1000 rpm the BSFC delta is out of 2%. In general, it is clear that the model understimates a little bit the BSFC when the lambda values is 1. The problem is due to a higher combustion efficiency compared to the measurements; probably the S_L variation changing the lambda is overestimated by the model. However, it should be noted that no different calibration constants are used and that the model therefore reacts consistently to the fuel metering change.

The higher temperature due to the lower fuel evaporation (worst volumetric efficiency) with a stochiometric mixture and a lower combustion velocity are the causes of performance loss. Running at lambda 1, the delta percentage at max power is experimentally 4.9% and 4.1% via simulation, confirming the better efficiency that the model foresees with lambda 1. It is necessary to clarify that this difference is also a consequence of different ambiental conditions. Comparing the perfomance parameters with the same ambient conditions, the delta performance at peak power reduced at 3.8%. It clear that the maximum power variation also depends on the turbulence level: an engine with a more intense tumble motion will be less sensitive to the lambda input. But for a high performance naturally aspirated engine, like the one under study, the intake duct is designed to exasperate the discharge coefficient to increase the power.

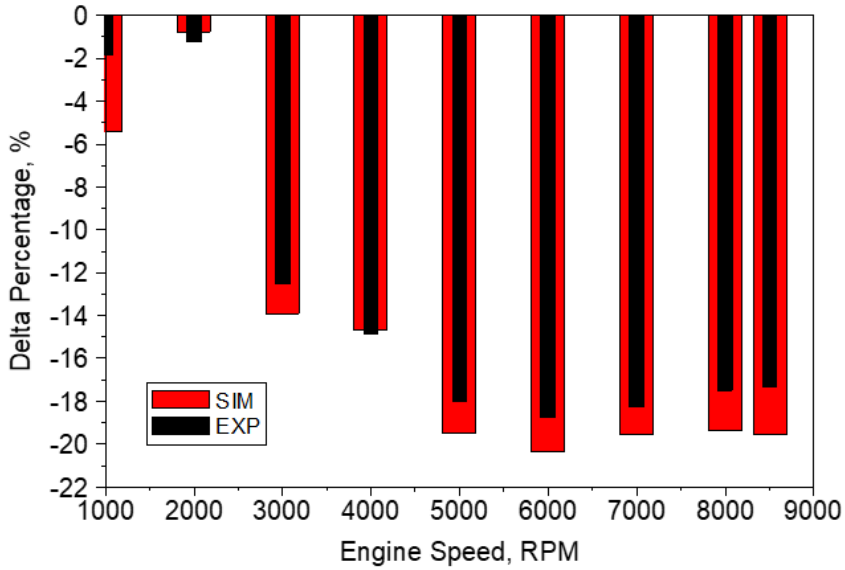

Figure 4.8 – Lambda stoichiometric vs lambda 1 in term of delta percentage BSFC, numerical/experimental assessment.

The accurate schematization of the engine piping is further proved by the experimental/numerical comparisons of the intake and exhaust traces at different engine speeds, shown in figure 4.9. The picture underlines that pressure fluctuations are very well captured by the model, both in terms of shape and pulse amplitude, for all the considered speeds.

Finally, in figure 4.10 it is possible to observe the comparison in terms of in-cylinder pressure and burn rate. It is evident that the model is able to reliably replicate the combustion process and consequently to resume the cycle in the area close to the TDCF in an accurate way.

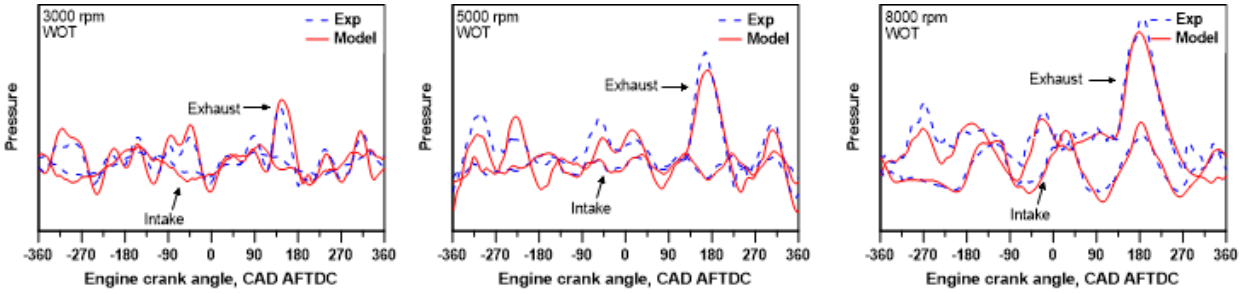

Figure 4.9 - Experimental/numerical assessment of the intake and exhaust pressure traces at 3000, 5000 and 8000 rpm WOT.

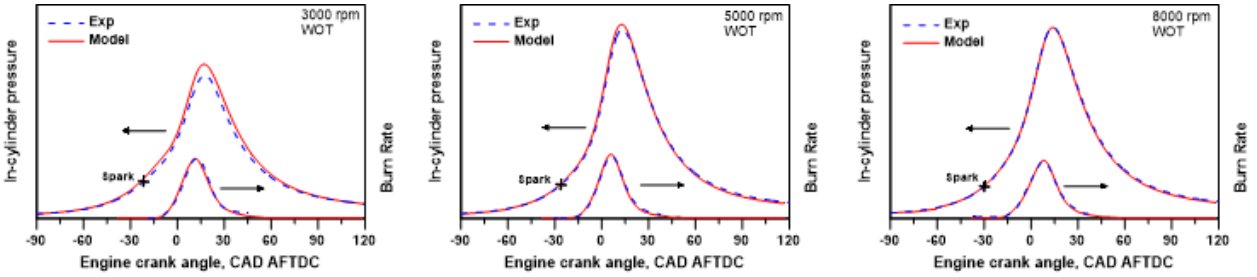

Figure 4.10 - Experimental/numerical assessment of the in-cylinder pressure traces at 3000, 5000 and 8000 rpm WOT.

The temperature at catalyst brick puts in evidence the second problem to work with lambda 1: the thermal management. For this research activity, the range of temperature for the catalyst safety has been extended of 170 °C, but for a series application this limit is impossible to reach with the current state of art. Even in this case, the model is able to follow the experimental trend.

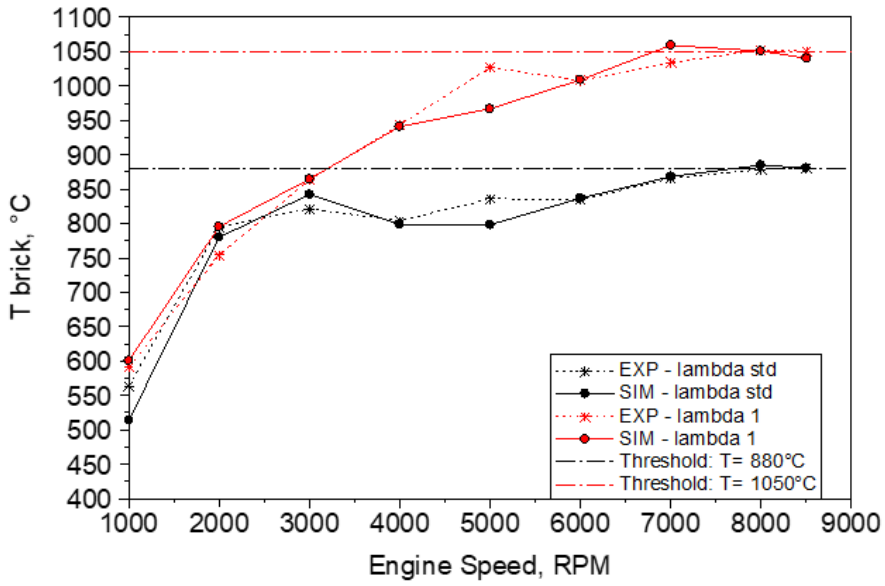

Figure 4.11 - Experimental/numerical assessment of in-catalyst temperature.

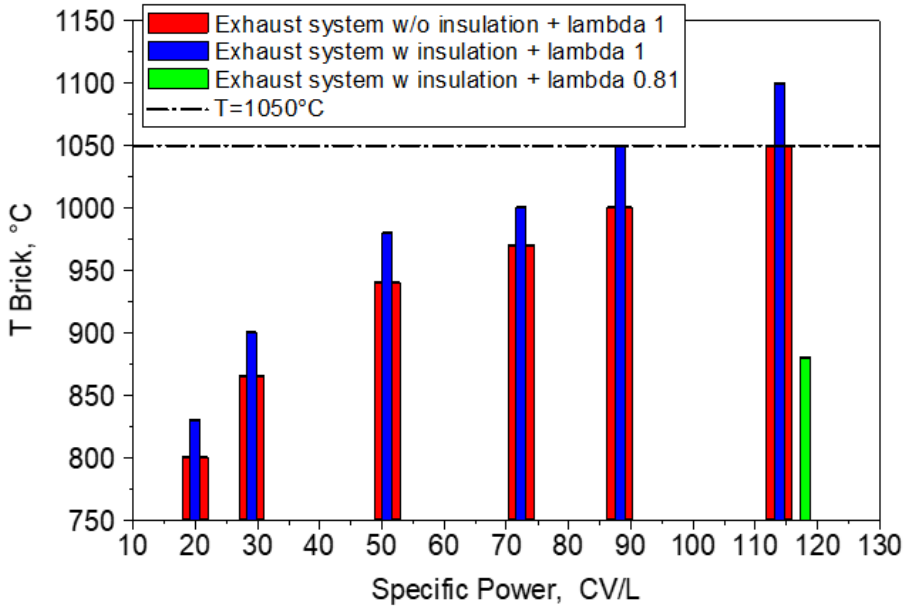

Figure 4.12 - Numerical assessment of in-catalyst temperature vs specific power.

A simulation with the exhaust system plus the insulation has run to understand the importance of managing the exhaust temperature without the possibility to adjust the gasoline metering. So, the delta power due to the combustion efficiency reduction from lambda rich to lambda 1 is 3.8%, without limitation in the exhaust temperature and increasing the heat transfer at test bench. But with a realistic limit of 950°C (state of art)

and a series production exhaust system the delta power increases to ≈ 50%. Now it is clear that the problem for high performance engine is significant and the solutions are essentially two ones:

- exit the cylinder at a lower temperature
- lower the temperature before entering the catalyst

The model also provides an estimation of the raw emissions of CO, HC and NO. These are assessed with the related measured data in figures 4.13 – 4.14 – 4.15. Starting from the CO concentration prediction, the model demonstrates to sense effects of the air/fuel enrichment, which results in a higher CO production. The trends in the picture clearly show the link between mixture enrichment and CO production. The curves in black (both experimental and numerical) present an increasing trend with the engine revs because we are injecting more gasoline than in the stoichiometric case. Instead, in this condition (curve in red), the trend is quite constant with the engine speed. The model fits well the experimental results with a percent error of about 25% on average.

The HC numerical estimation is less accurate, especially at very low load. This is probably due to an overestimation of the post-oxidation effect under such operating conditions. The model detects the reduced HC production around the 2000 rpm and higher levels at high speed. On the contrary, the simulation is not able to perceive the increase of HC emissions at the lowest speeds and in the speed range 4000-5500 rpm. Despite the highlighted errors, the model predictions can be considered adequately accurate (with a percent error of about 30% on average) in the light of the adopted very simplified approach, which does not consider some HC formation mechanisms. However, the proposed modeling is able to perceive the change of the mixture dosage: the model is well affected by the decrease of HC when the engine runs in stoichiometric conditions.

Moving to the NOx model response, the related experimental/numerical maps in figure 4.15 present very similar shapes. Maximum NOx concentrations, in accordance with the measurements, are estimated where the λ values are close to the stoichiometric levels, which simultaneously determine higher in-cylinder temperatures and lack of molecular

oxygen in the burned gas. The good prediction of NOx is in accordance to the global good prediction of the in-cylinder temperatures. The percent error of about 20% on average.

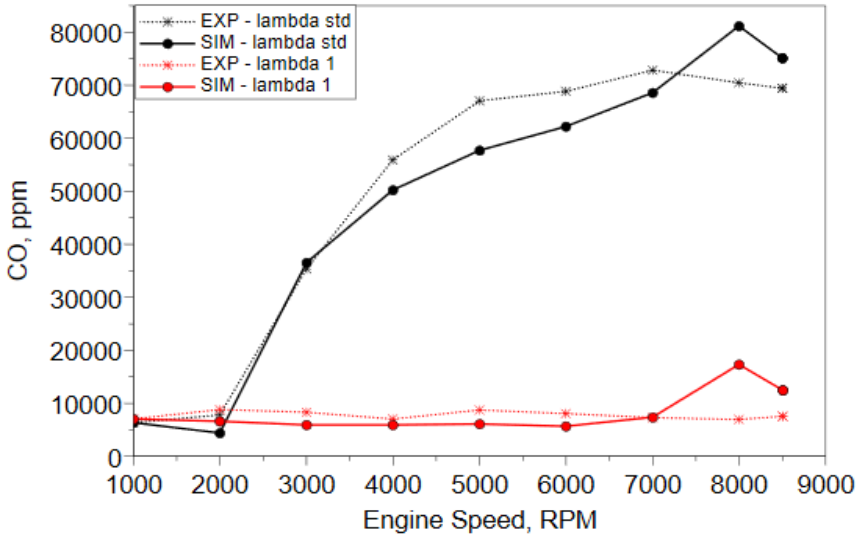

Figure 4.13 - Experimental/numerical assessment of engine out CO emissions.

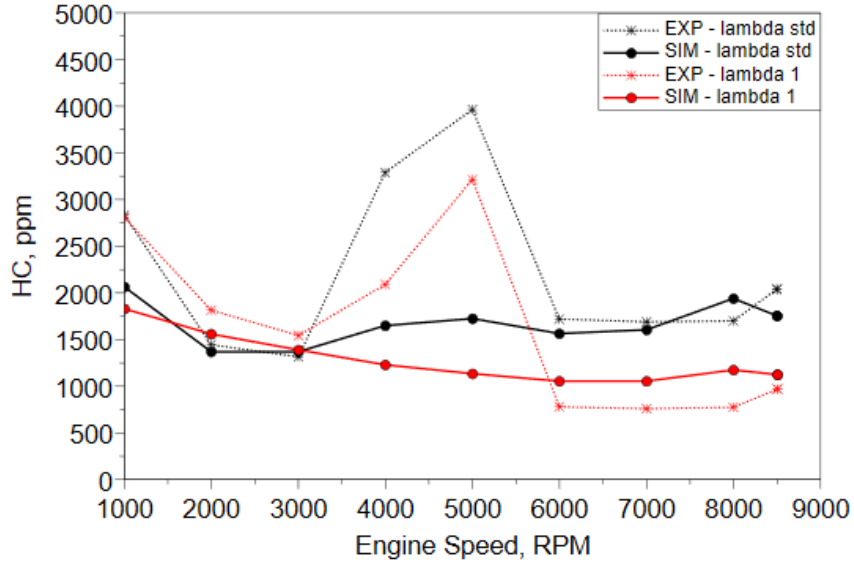

Figure 4.14 - Experimental/numerical assessment of engine out HC emissions.

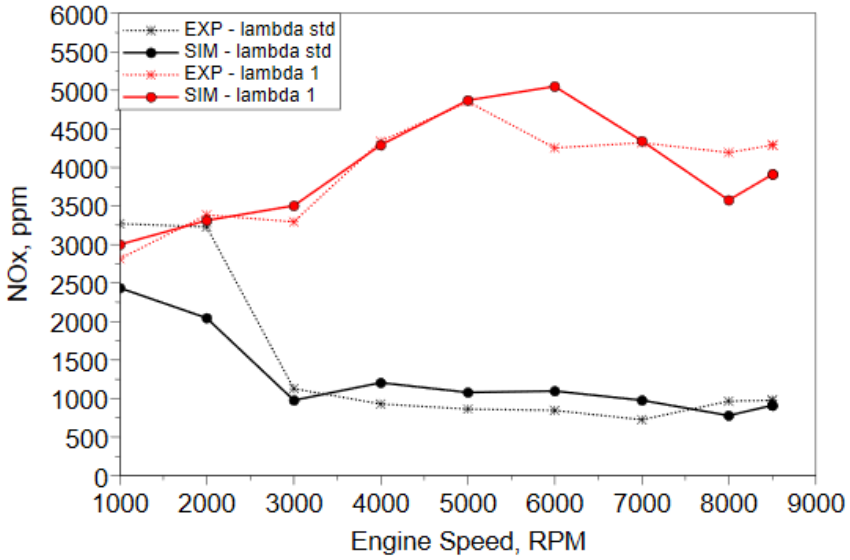

Figure 4.15 - Experimental/numerical assessment of engine out NO emissions.

Engine Model validation at Part Load

The model consistency is verified over the whole engine operating plane, based on the experimental data collected under part load conditions. To this aim, the tuning of turbulence / combustion / heat transfer model is not modified compared to the full load analysis. The simulation inputs are the same as the full load setup, namely, the intake/exhaust valve timing, the flap position, the air/fuel mixture quality and the MFB_{50}. The only difference regards the throttle valve opening, which is modulated by an automatic controller targeting the measured BMEP level. The simulation reliability is here verified by comparing the experimental/numerical maps of air flow rate, BSFC, combustion phase MFB_{50}, exhaust temperature in three-way catalyst and raw concentrations of CO, HC and NOx (upstream the catalytic converter).

For all comparisons the same level and color scale are chosen for the measured and calculated data, so to favorite the figures readability and comparability.

Starting from the experimental/numerical BSFC comparison of figure 4.17, it can be observed that the model is able to reproduce the measured data with an adequate accuracy. It is able to correctly detect the level and the speed-BMEP range of minimum fuel consumption. In addition, it shows the capability to perceive the BSFC worsening at

increasing speed, which is mainly due to the air/fuel mixture enrichment, and at reducing load, which is affected by the intake throttling. The computed and experimental contours of combustion phase MFB_{50} in figure 4.19 present a similar shape. As well as the full load simulations, the model slightly overestimates this parameter compared to the experimental outcomes, excepting in the region of very low load. Figure highlights a combustion lengthening for speeds below 4000 rpm, which is due to the activation of the muffler along the exhaust line. This causes an increased backpressure and a higher level of residual gas in the cylinder, affecting the combustion speed. The model shows to perceive quite well this phenomenology, as demonstrated by the experimental/numerical comparison. The latter underlines that the residual content is quite low for this engine over the whole operating plane, and even at low load. As a further demonstration of the model consistency, the experimental and numerical iso-lines of exhaust temperature are plotted in figure 4.21. The maps are similar in terms of both shape and level. The expected temperature increase at rising engine speed is partially compensated by the air/fuel enrichment, highlighted in figure 4.18. The maximum temperature occurs at high speed and it is the upper limit allowable by the after treatment device.

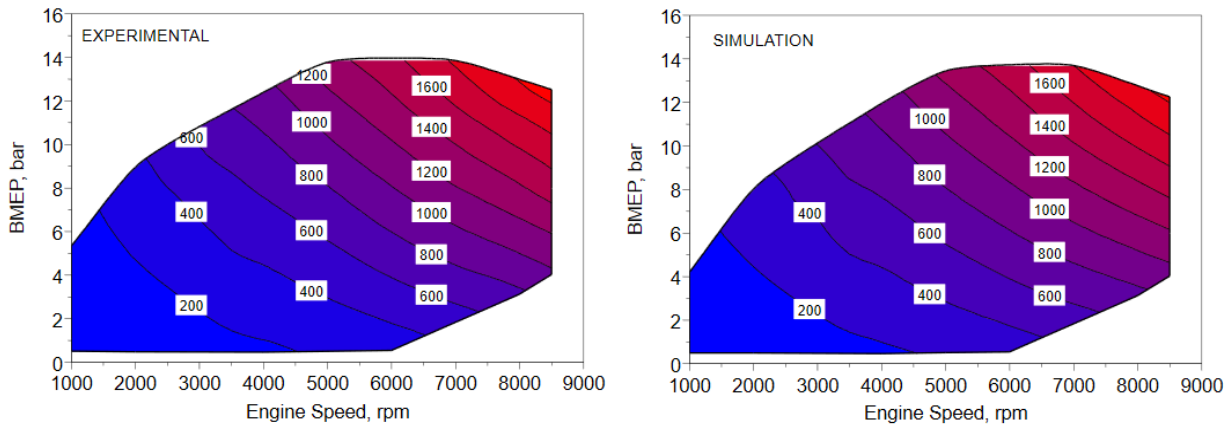

Figure 4.16 - Experimental (left) and numerical (right) air flow rate maps.

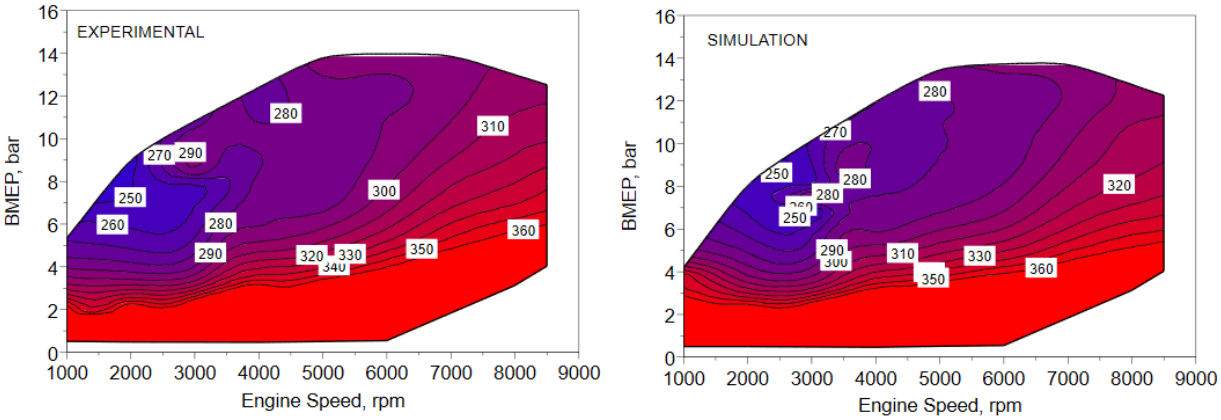

Figure 4.17 - Experimental (left) and numerical (right) BSFC maps.

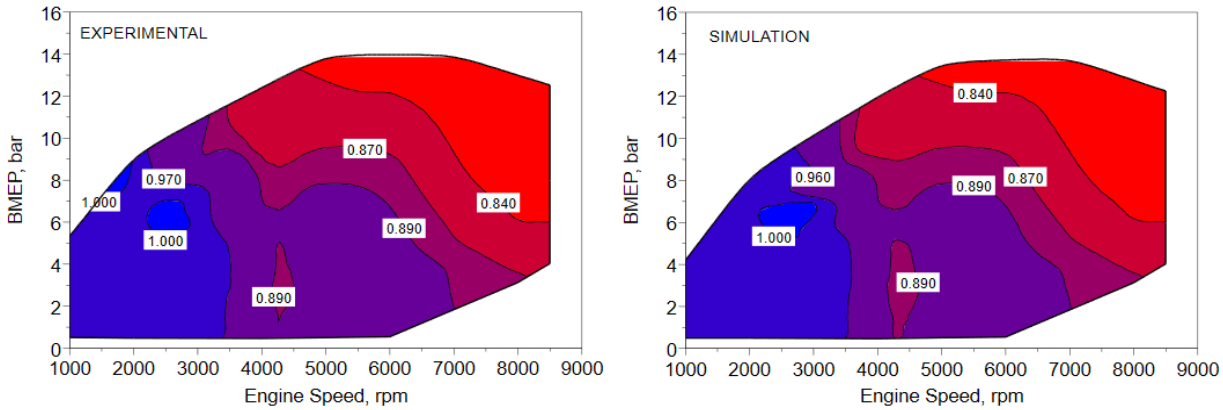

Figure 4.18 - Experimental (left) and numerical (right) lambda maps.

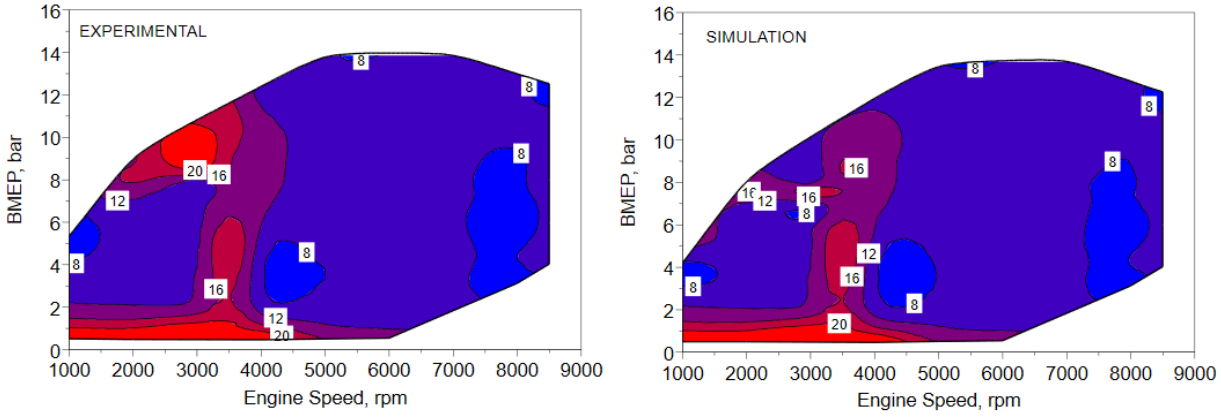

Figure 4.19 - Experimental (left) and numerical (right) MFB_{50} maps.

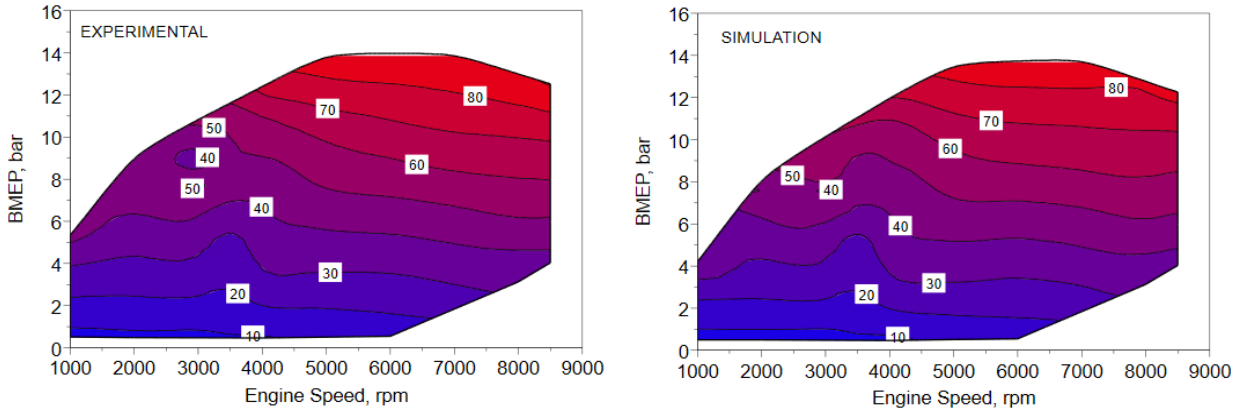

Figure 4.20 - Experimental (left) and numerical (right) in-cylinder maximum pressure maps.

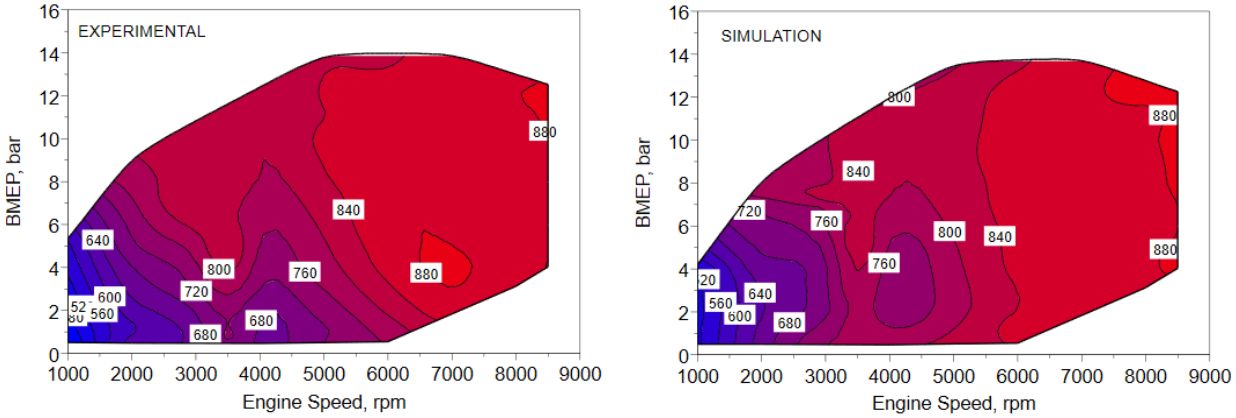

Figure 4.21 - Experimental (left) and numerical (right) three-way catalyst temperature maps.

The model also provides an estimation of the raw emissions of NOx, CO and HC. These are assessed with the related measured data in figure 4.22, figure 4.23 and figure 4.24, respectively. The iso-contour shapes of the emission maps resemble the corresponding experimental counterpart, but the predicted levels are in in some cases quite different. Starting from the CO concentration prediction, the model demonstrates to sense effects of the air/fuel enrichment, which results in a higher CO production. However, numerical estimations are about 19% lower than the measured concentration on average. The HC numerical estimation is less accurate, especially at very low load. This is probably due to an overestimation of the post-oxidation effect under such operating conditions. The model detects the reduced HC production around the 3500 rpm and higher levels at high speed and medium loads. On the contrary, the simulation is not able to perceive the increase of HC emissions at the lowest speeds and in the speed range 4000-5500 rpm close to the

full load operations. Despite the highlighted errors, the model predictions can be considered adequately accurate (with a percent error of about 31% on average) in the light of the adopted very simplified approach, which does not consider some HC formation mechanisms. Moving to the NOx model response, the related experimental/numerical maps in figure 4.19 present very similar shapes of the iso-NOx curves. Maximum NOx concentrations, in accordance with the measurements, are estimated in the region where the λ values are close to the stoichiometric levels, which simultaneously determine higher in-cylinder temperatures and lack of molecular oxygen in the burned gas. However, the simulation gives on average a NOx prediction similar to the experimental counterpart.

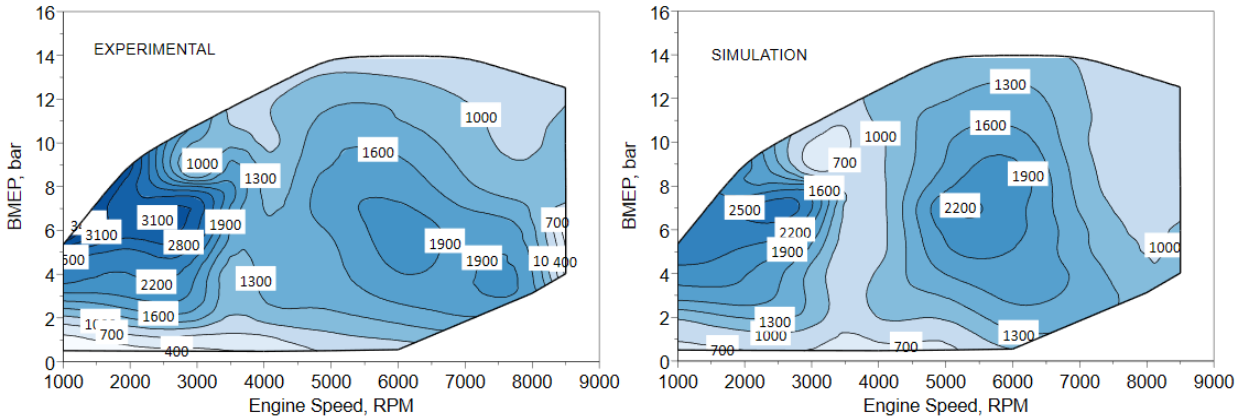

Figure 4.22 - Experimental (left) and numerical (right) NOx concentration maps.

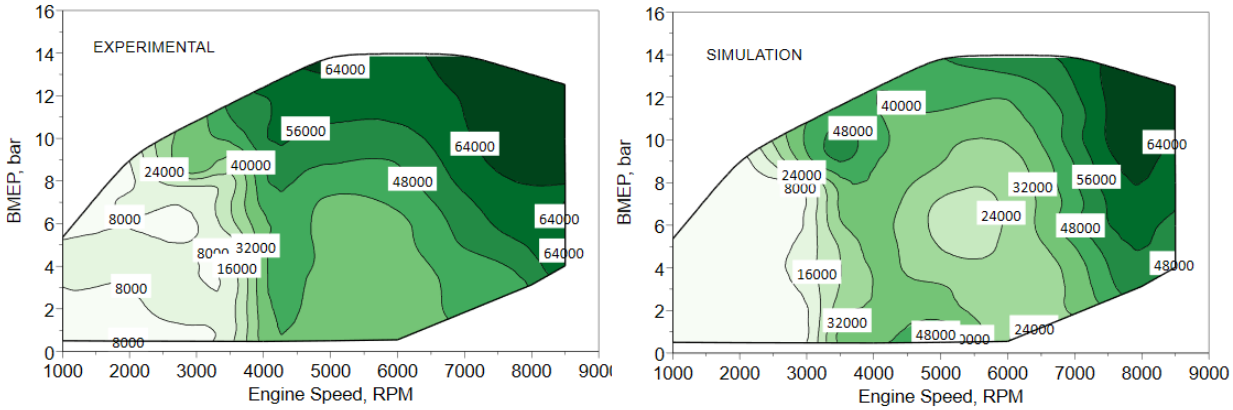

Figure 4.23 - Experimental (left) and numerical (right) CO concentration maps.

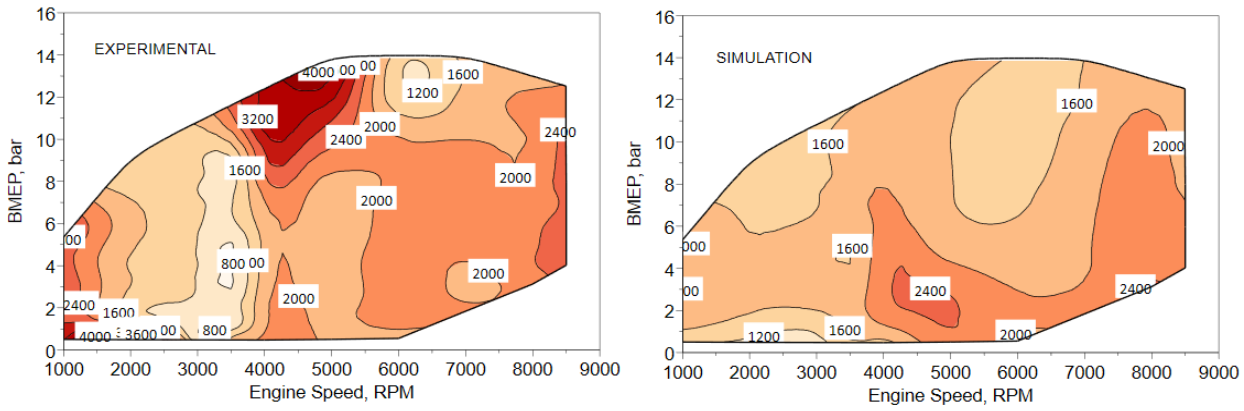

Figure 4.24 - Experimental (left) and numerical (right) HC concentration maps.

The proposed results about the pollutant emissions put into evidence that the numerical approach is enough advanced to quantitatively predict the experimental data of NOx and CO, but not for the HC. Although the variations with the engine operating parameters (speed, load, λ) are captured. For this reason, the model will be employed in the following to draw the variation trend of the pollutant emissions changing the engine calibration, rather than to predict their absolute levels.

Same comparisons are done with the lambda 1 on entire the engine map (figure 4.27). The performance results are aligned with the experimental ones. The BSFC comparison of figure 4.26 shows that the model is able to reproduce the measured data with an adequate accuracy. Once it is able to correctly detect the level and the speed-BMEP range of minimum fuel consumption. In addition, it shows the capability to perceive the BSFC worsening at increasing speed, which is mainly due to the air/fuel mixture enrichment, and at reducing load, which is affected by the intake throttling.

As a further demonstration of the model consistency, the experimental and numerical iso-lines of exhaust temperature are plotted in figure 4.30. The maps are similar in terms of both shape and level. The temperature increases at rising engine speed; in this case there is not fuel enrichment and the maximum temperature occurs at high speed.

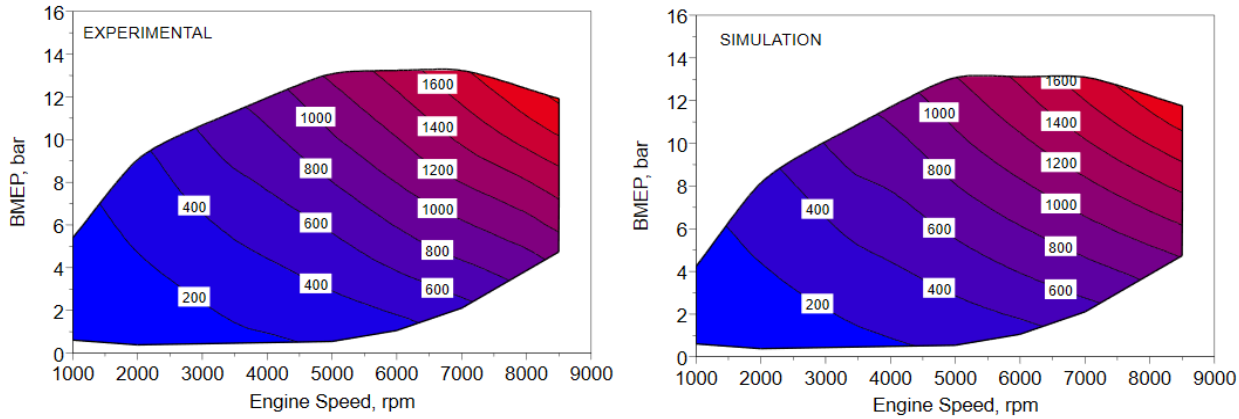

Figure 4.25 - Experimental (left) and numerical (right) air flow rate maps.

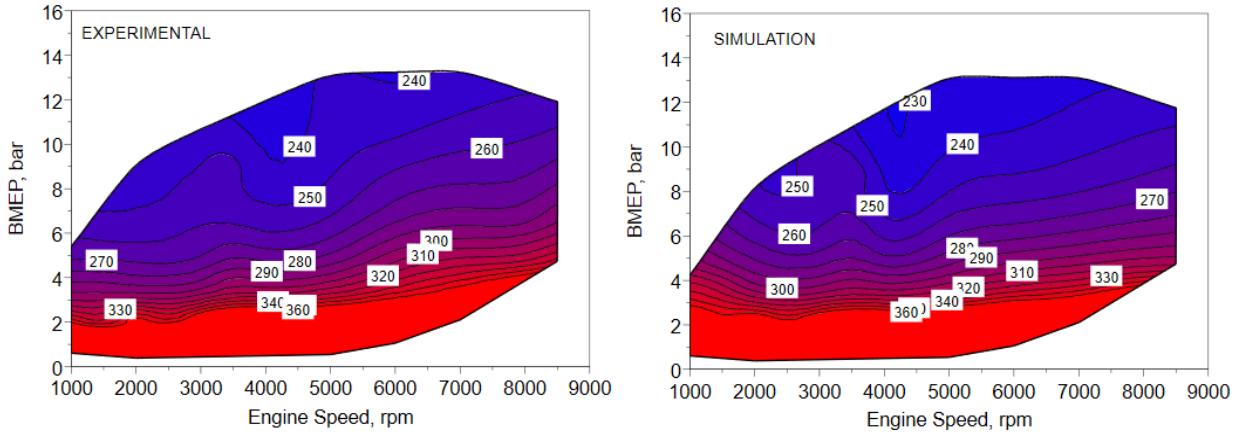

Figure 4.26 - Experimental (left) and numerical (right) BSFC maps.

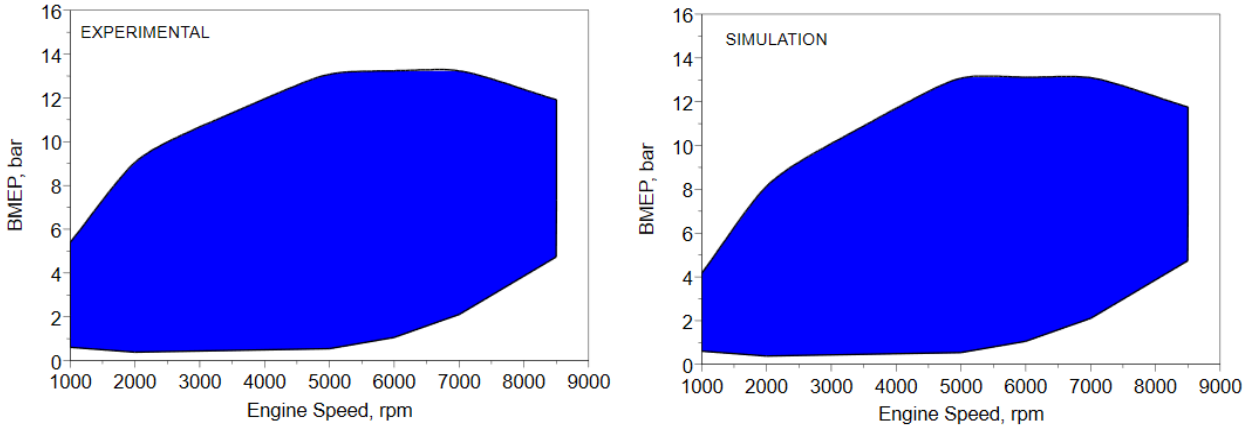

Figure 4.27 - Experimental (left) and numerical (right) lambda maps.

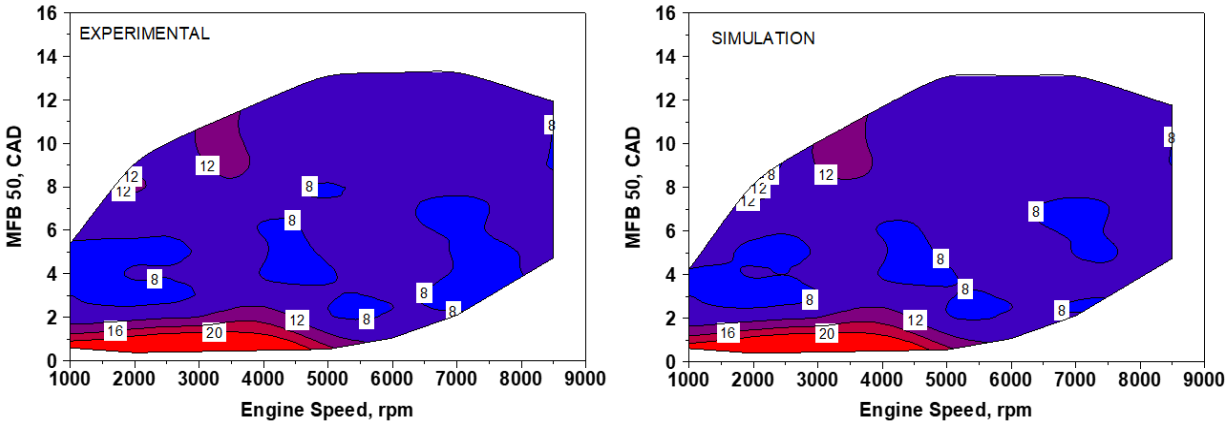

Figure 4.28 - Experimental (left) and numerical (right) MFB50 maps.

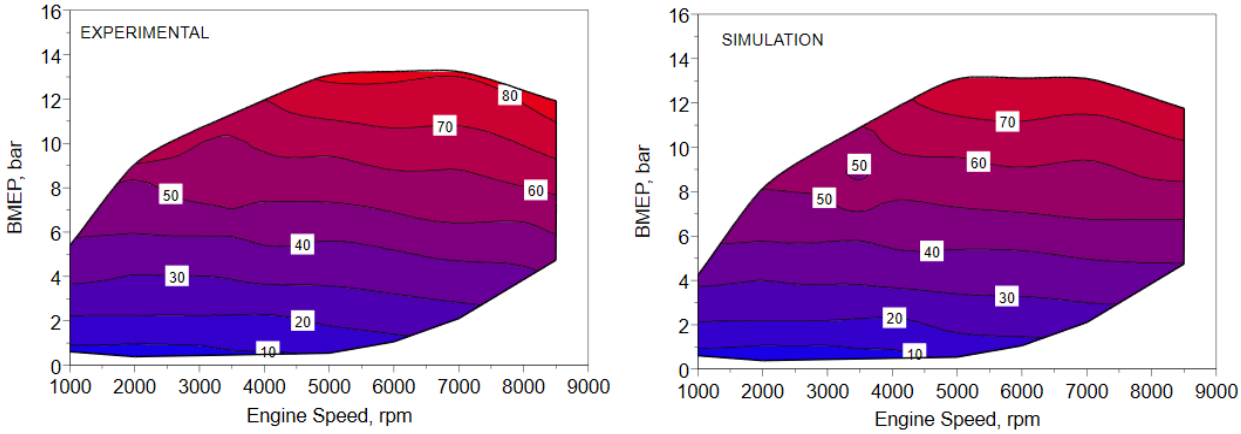

Figure 4.29 - Experimental (left) and numerical (right) in-cylinder maximum pressure maps.

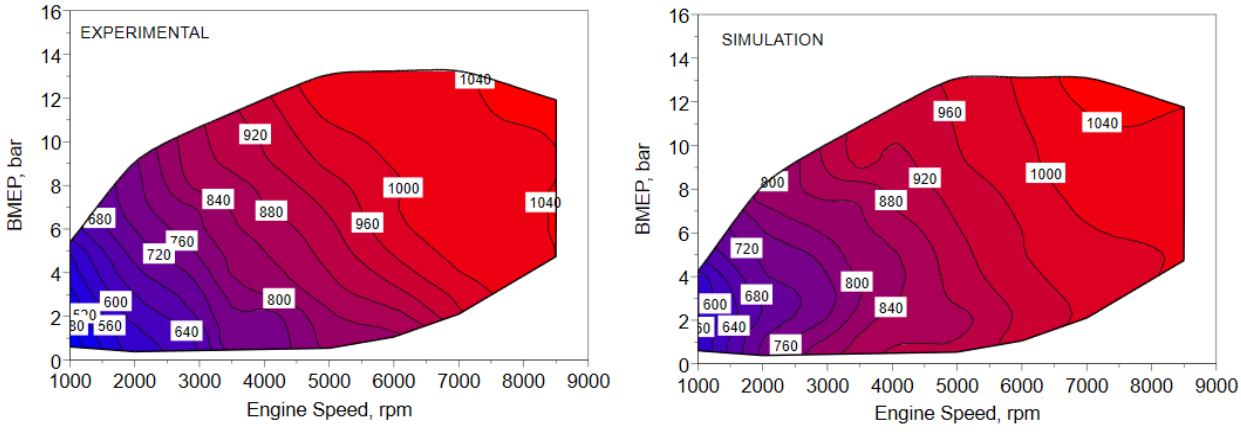

Figure 4.30 - Experimental (left) and numerical (right) three-way catalyst temperature maps.

The estimation of the raw emissions of NO, CO and HC are assessed with the related measured data in figure 4.31 - 4.32 and 4.33, respectively. The iso-contour shapes of the emission maps resemble the corresponding experimental counterpart, but the predicted levels are in most cases quite different. Starting from the CO concentration prediction, the model demonstrates to follow the experimental trends well. However, the numerical estimations are about 21% lower than the measured concentration on average. Again, the HC numerical estimation is less accurate, especially at very low load. This is probably due to an overestimation of the post-oxidation effect under such operating conditions. The model detects the minimum HC zone and high load and rpm. On the contrary, the simulation is not able to perceive the increase of HC emissions at the lowest speeds and in the speed range 4000-5500 rpm close to the full load operations. Despite the highlighted errors, the model predictions can be considered adequately accurate (with a percent error of about 31% on average) in the light of the adopted very simplified approach, which does not consider some HC formation mechanisms. Moving to the NOx model response, the related experimental/numerical maps in figure 4.31 present very similar shapes of the iso-NOx curves. Maximum NOx concentrations, in accordance with the measurements, are estimated in the region where the higher in-cylinder temperatures are determined. On the other hand, the model slightly underestimates the concentration in the area of peak power. However, the simulation gives on average a NOx prediction similar to the experimental counterpart.

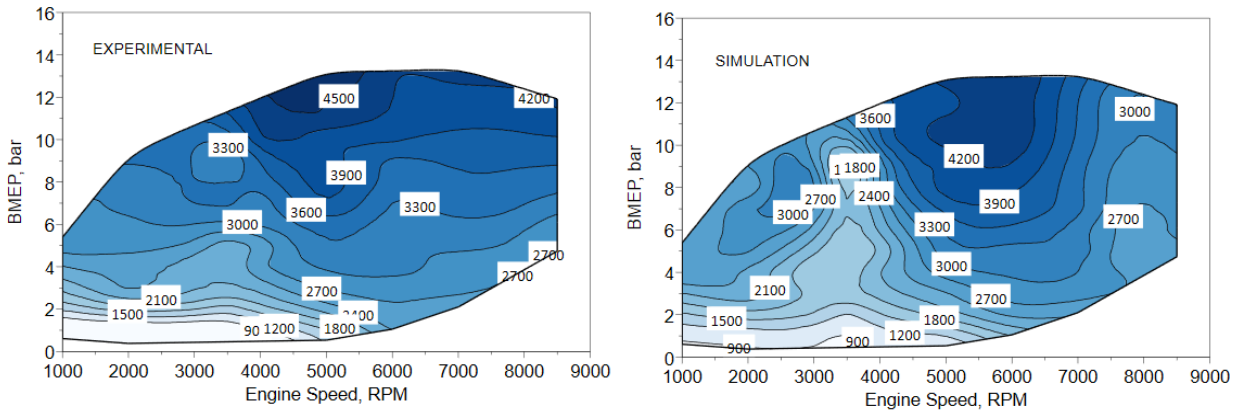

Figure 4.31 - Experimental (left) and numerical (right) NOx concentration maps.

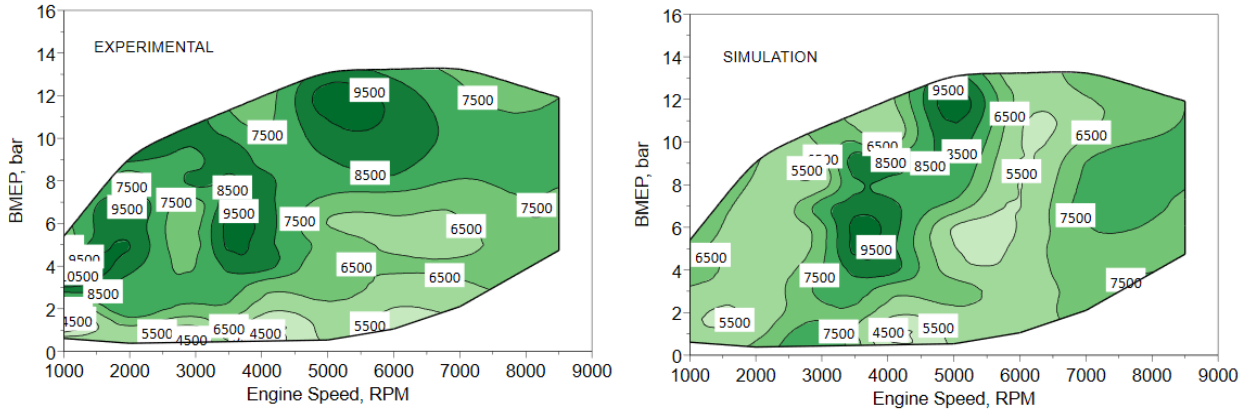

Figure 4.32 - Experimental (left) and numerical (right) CO concentration maps.

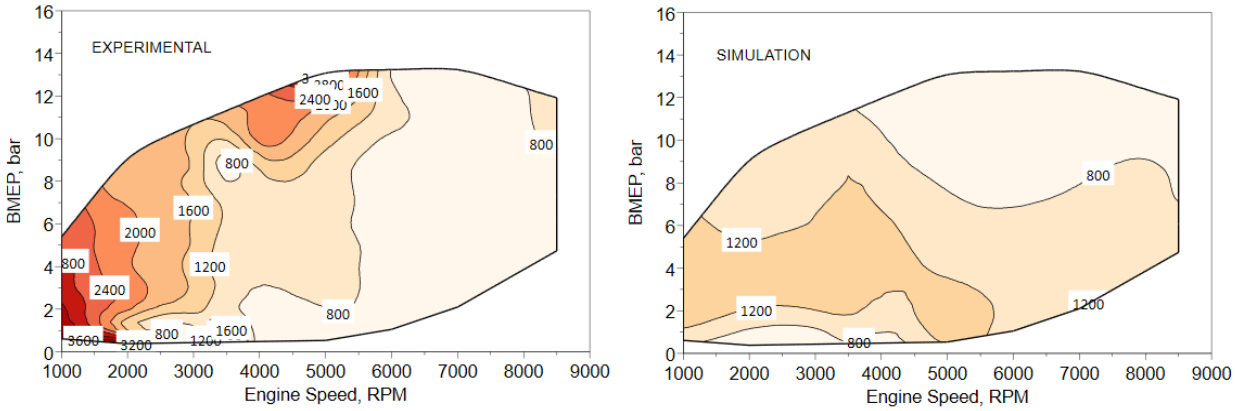

Figure 4.33 - Experimental (left) and numerical (right) HC concentration maps.

Water injection setup

The water is introduced in the engine model by injectors located at the end of each intake runner, just upstream of the fuel injectors (figure 4.34). It is a solution to reduce the temperature at exhaust without fuel enrichment. So, those simulations are performed with lambda set at 1.

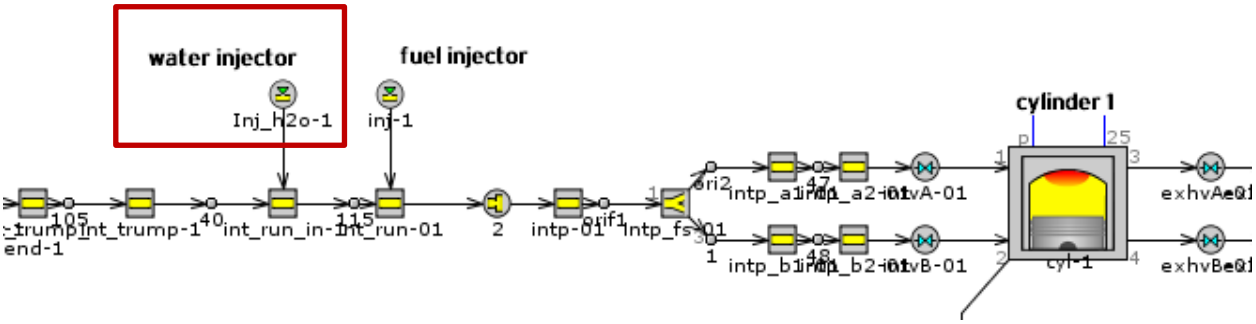

Figure 4.34 – Water injector on the 1D engine model.

A discontinuous injection of liquid water at a temperature of 25 °C is specified. It is assumed that 30% of the total mass of water vaporizes immediately upon the injection. This value is equal to the one advised for a typical fuel injector in the GT-Power user manual. A parametric analysis, not reported here for brevity, showed that substantial variations in the above percentage do not significantly affect the simulation results. Due to the low temperature and pressure, water evaporation is abled in the intake pipes downstream of the injectors. Water evaporates inside the cylinders, at a rate provided by a semi-empirical correlation. With this assumption, water evaporation begins during the intake stroke, and completes before the spark event. The water evaporation heat is assumed to be subtracted from the cylinder/piston walls and the working fluid to the same extent (50%). Although no data are currently available to verify the reliability of the previous assumptions, they appear reasonable.

A refined model of the heat transfer inside the cylinder and exhaust pipes is also introduced, applying a wall temperature solver based on a finite element approach. Concerning the in-cylinder heat transfer, a Hohenberg-like correlation is used, while convective, radiative and conductive heat transfer modes are considered for the exhaust pipes.

To elude water condensation and oil emulsion in a real application, the amount of injected water is restricted to a maximum water/fuel (W/F) ratio of 0.3. In order to have a direct comparison with the case without water, the VVT strategy is not modified. A PID controller (figure 4.35) manages the amount of water injected. When the exhaust temperature is higher than 950°C, the amount of water injected increases until the temperature goes down below the above constraints. The upper limit, as announced, is imposed as a water

to fuel ratio of 0.3. The map in fig. 4.36 shows the iso-contours of water to fuel ratio. This underlines that the water to fuel ratio reaches the maximum value of 0.3 for the higher engine speeds and loads, while it is 0 for the speeds below 4000 rpm.

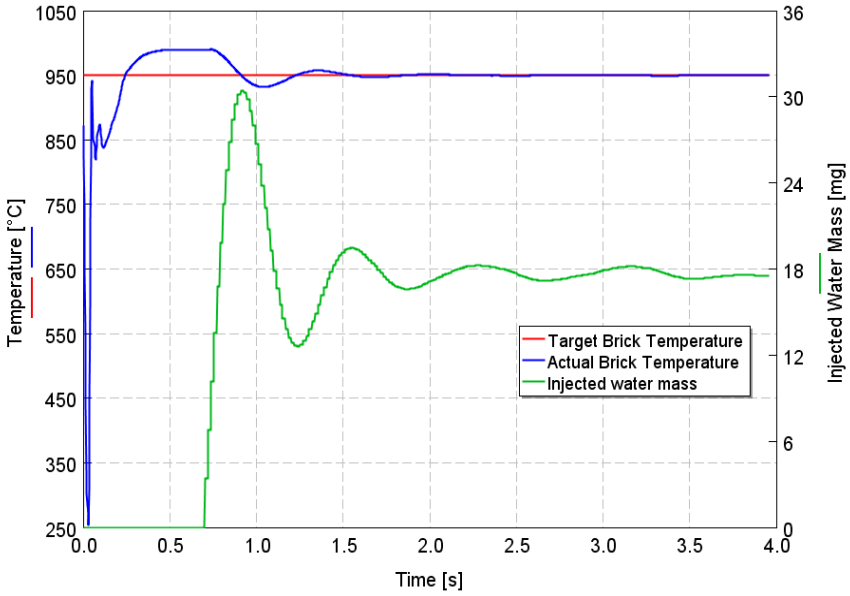

Figure 4.35 – PID controller for water injection mass.

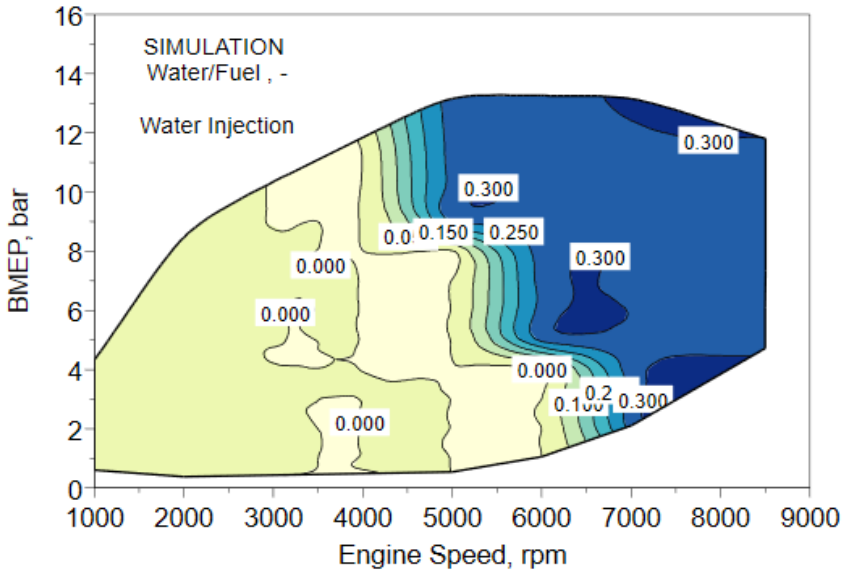

Figure 4.36 – Water to fuel ratio map.

The spark advance is controlled by another PID controller. The strategy is to work around the maximum brake torque (MBT), unless there is a knock phenomenon. In this case, the spark is appropriately delayed. In this way, the engine works at maximum performance with the water that cools the exhaust gas (both because it allows for more advanced spark and because it absorbs heat to evaporate) reducing the temperature at the catalyst. In this case, the aim is not to optimize the use of water to try to minimize emissions, but with the sole purpose of cooling the gas at the exhaust. As an additional positive effect, the combustion phasing can be anticipated, thanks to the knock mitigation capability of this technique.

Water injection results

The comparisons here proposed are is between numerical results. The figure 4.37 puts into evidence that the water gives a small reduction in term of brake specific fuel consumption.

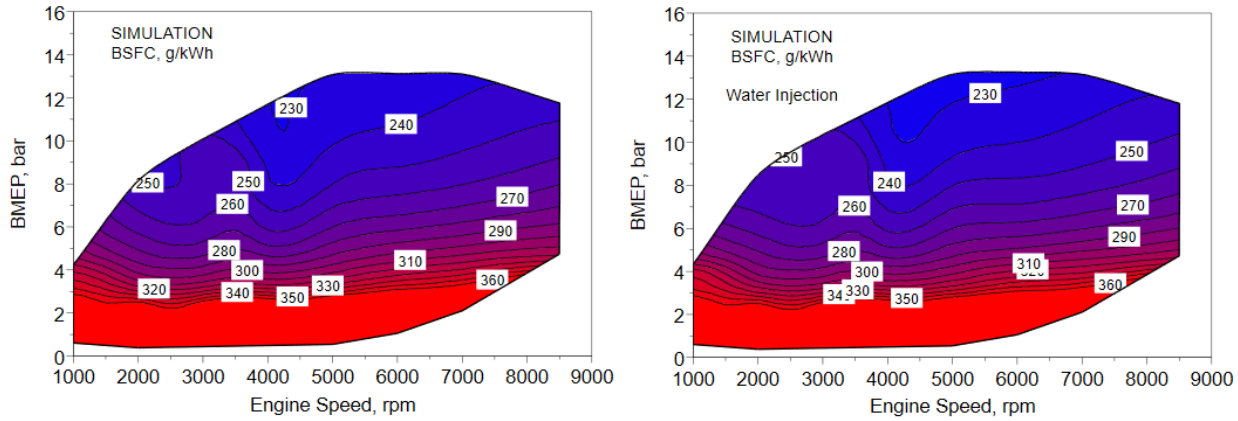

Figure 4.37 – Numerical λ1 (left) and numerical λ1 + water injection (right) BSFC maps.

The combustion reaches everywhere the MFB_{50} that determines the maximum brake torque (figure 4.38). This is because the water evaporation, lowering the in-cylinder temperature, gives the possibility to avoid the knock phenomena.

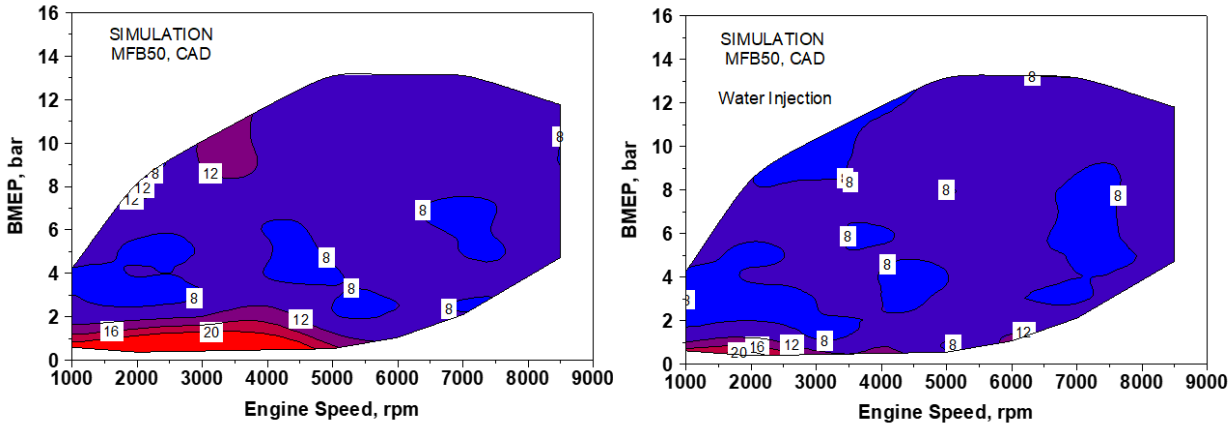

Figure 4.38 – Numerical λ1 (left) and numerical λ1 + water injection (right) MFB_{50} maps.

The variation of the exhaust gas temperature with engine speed without and with water injection is shown in figure 4.39. The heat absorbed by the water evaporation explains the decrease in the exhaust temperature. Lower exhaust gas temperature is an indication of a lower mean-cycle in-cylinder temperature through the engine cycle. The delta temperature attains a maximum of 40°C. It should be noted that, even with the maximum allowed water-fuel ratio of 0.3, safe operation are not allowed over the entire map. In fact, one portion of the map remains with catalyst input temperature above 950°C.

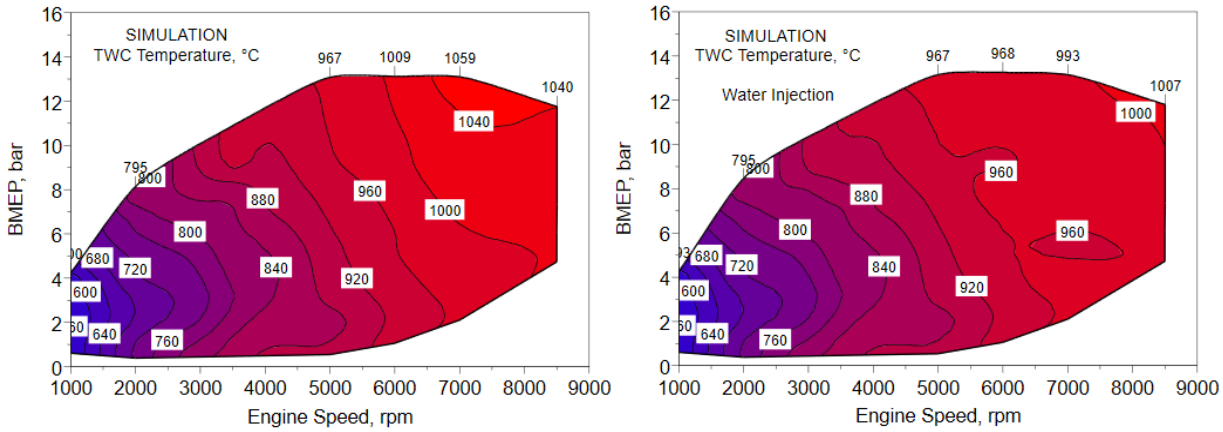

Figure 4.39 – Numerical λ1 (left) and numerical λ1 + water injection (right) T three-way catalyst maps.

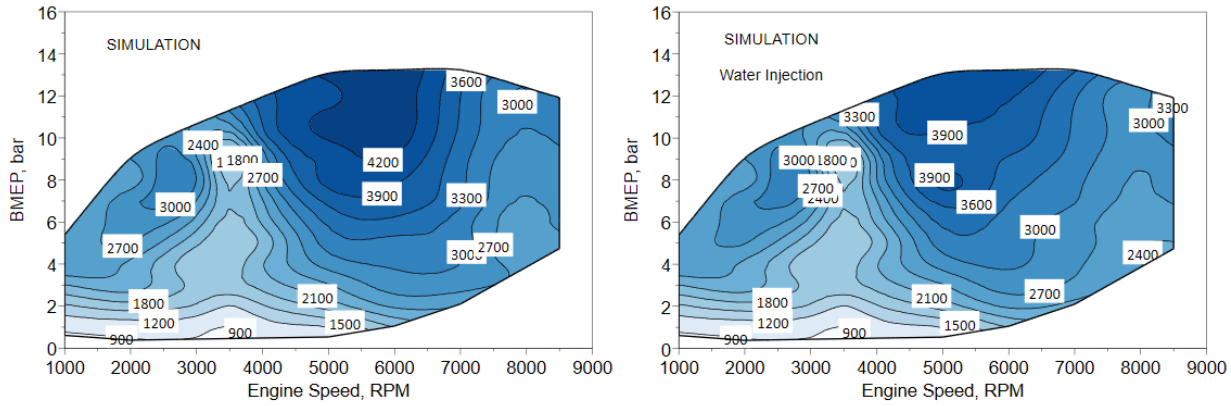

Figure 4.40 – Numerical λ1 (left) and numerical λ1 + water injection (right) NO maps.

A reduction in term on NOx concentration (figure 4.40) due to the lower in-cylinder temperature is predicted by the model. The average reduction is of 17.5%.

The impact of water on CO as expected is not perceptible. While, as expected, there is a slight increase in HC. It is finally clear that lambda 1 and lambda 1 plus water injection maps are the same in low load and low speed zones, where water fraction is zero.

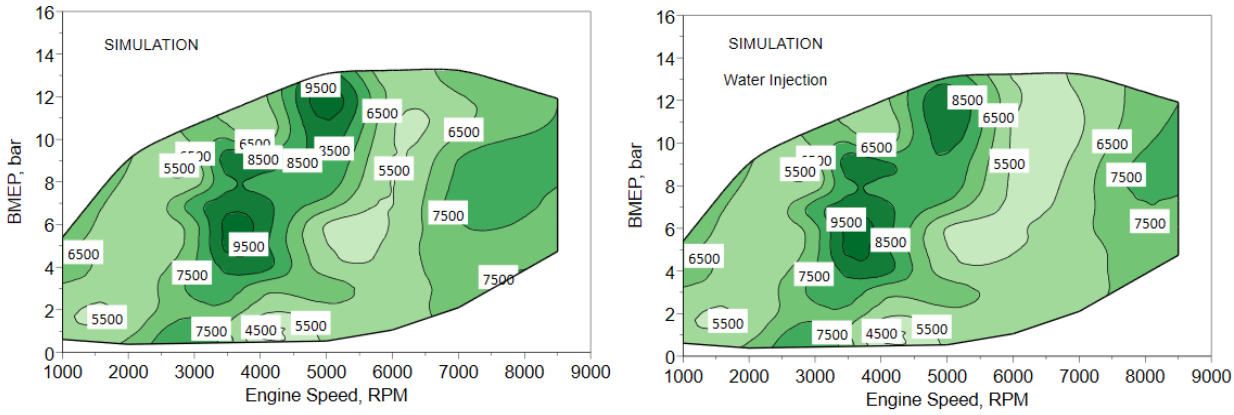

Figure 4.41 – Numerical λ1 (left) and numerical λ1 + water injection (right) CO maps.

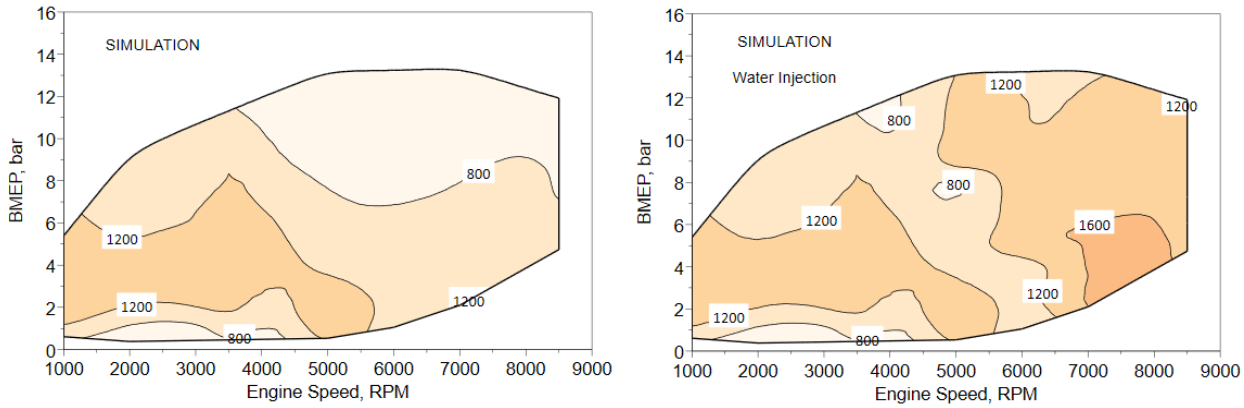

Figure 4.42 – Numerical λ1 (left) and numerical λ1 + water injection (right) HC maps.

5. Vehicle model

Starting from the previous results, a map approach has been used to build up a vehicle model. To limit the computational effort, the thermal unit is described by a quasi-steady map-based approach, instead of a physical engine model (crank angle resolved). The so-called “dynamic analysis” is executed, where the vehicle control is managed by a “virtual driver”, based on PID logics, which selects the gear ratio and the pedal position required to follow the imposed speed profile. To this aim, the model takes into account the vehicle inertial forces and resistances (aerodynamic and rolling load). A proper gear shift strategy is implemented. The input engine maps in term of brake power, friction, fuel consumption and emissions came out from the engine simulation commented in the previous chapter.

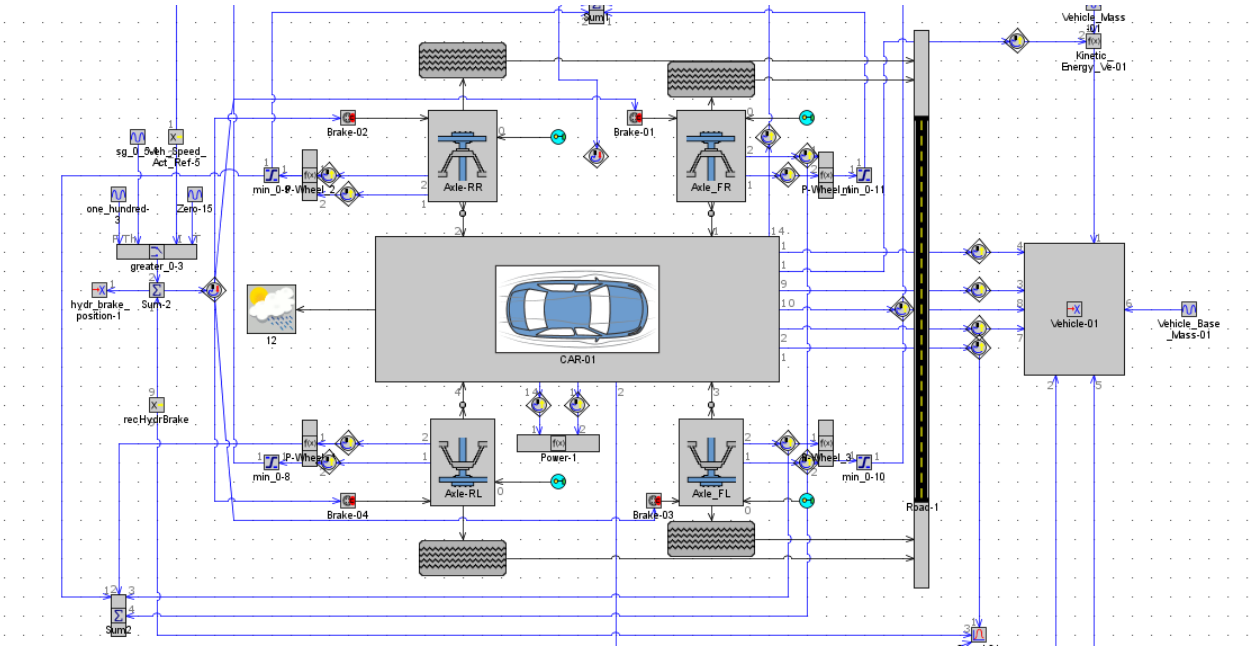

Figure 5.1 – Vehicle model schematization.

The driving cycle investigated is an RDE cycle provided by Automobili Lamborghini and reported in figure 5.2. It is a very aggressive cycle and it is considered from the company the worst case for the CO emissions that this hardware (vehicle + engine) can meet.

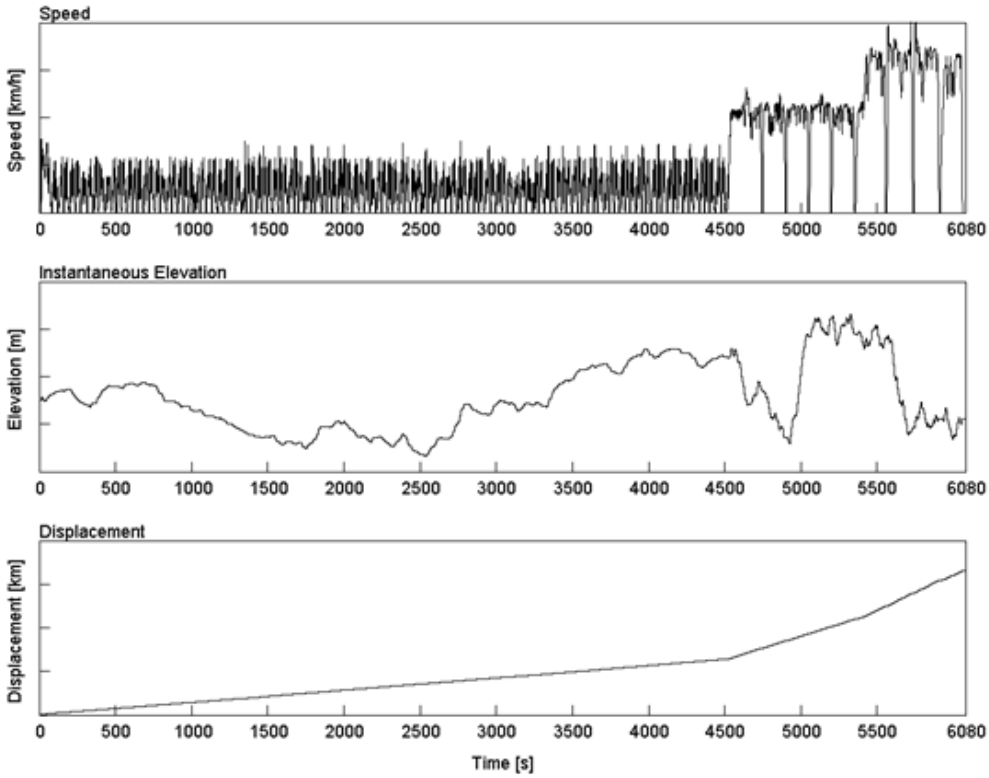

Figure 5.2 – RDE cycle: speed and elevation profiles and cumulative displacement.

The cycle fulfills all the RDE compliance. The vehicle simulation provides as an output the time spent by the engine in each point along the driving cycle. The figure 5.3 shows a comparison between the engine operation point when the vehicle run two different types of cycle: WLTC and RDE. The time step is 0.1 s. It is clear that by running an RDE cycle, the engine is working across most part of the operating range, once again highlighting the need for action from the engine development phase to improve the engine behavior over the entire operating domain. On the WLTC cycle, the engine runs up to the middle engine speed and with low loads. It never reaches the maximum power or torque. And in this area, the engine operates under the best conditions to reduce the emission: the temperature is not so high for component protection and the engine is able to run with a stoichiometric value of mixture. Instead, when the vehicle run the RDE cycle, the difference is relevant. The engine operating points cover the entire engine map and also the zones of maximum torque and power.

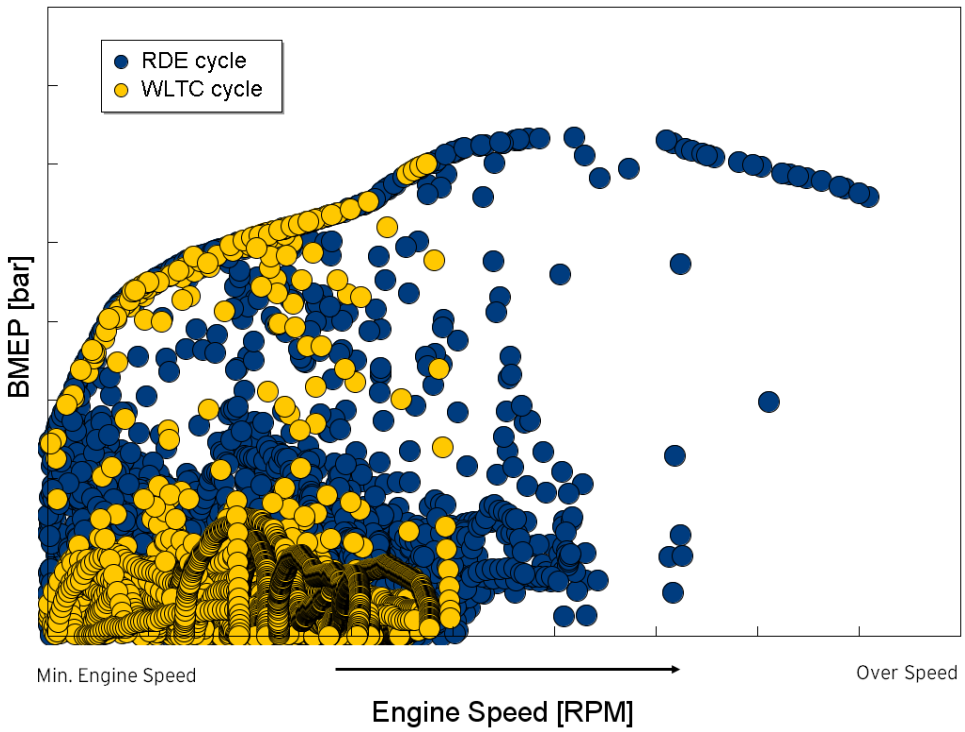

Figure 5.3 – Engine operation points when the vehicle run a WLTC (yellow dots) and an RDE cycle (blue dots).

The objective is to estimate the raw emissions over the driving cycle. To do this, it is necessary to correct the emission maps obtained with the previous numerical method. In fact, the computed maps are measured with standard conditions for what concern:

- Lambda
- ignition timing
- coolant temperature (90 °C)

The innovation introduced in this paragraph is that the transient operations during the cycle are considered using correction factors derived from experimental measurements on different engines at test bench. The figure 5.4 summarizes the workflow for determining the dynamic corrected raw emissions.

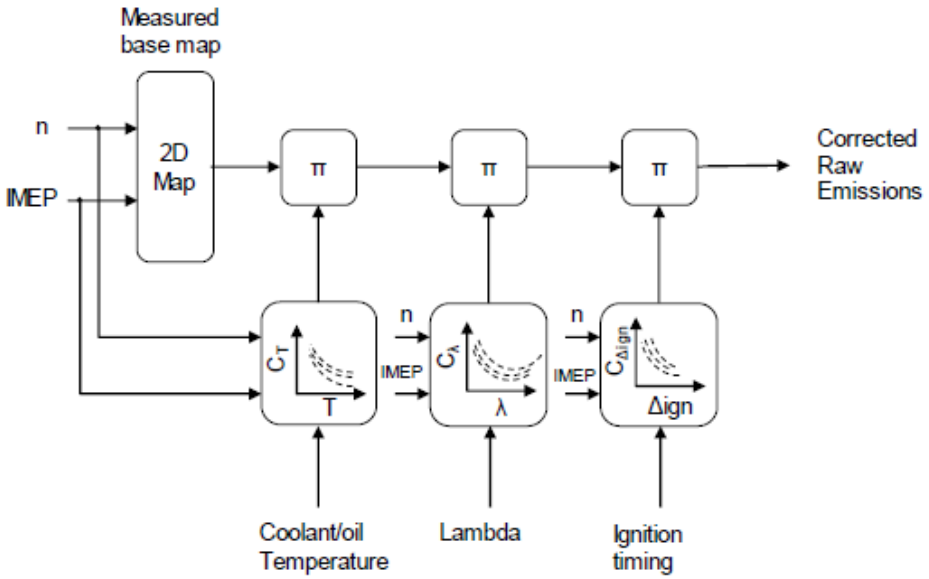

Figure 5.4 – Workflow to switch from stationary to dynamic emissions.

Figure 5.5 shows how the correction factors for HCs are determined as a function of temperature. The correction factor of warm engine conditions (90°C) is equal to 1. Example:

Measured $HC_{T=90°C}$=330ppm

Measured $HC_{T=50°C}$=594ppm

Correction factor:

Factor $HC_{T=50°C}$=(594 ppm)/(330 ppm)=1.8

The correction maps have been built at three different engine load levels: 2 - 8 and 14 bar. Then the results are interpolated by the Cftool included in the Matlab™ software.

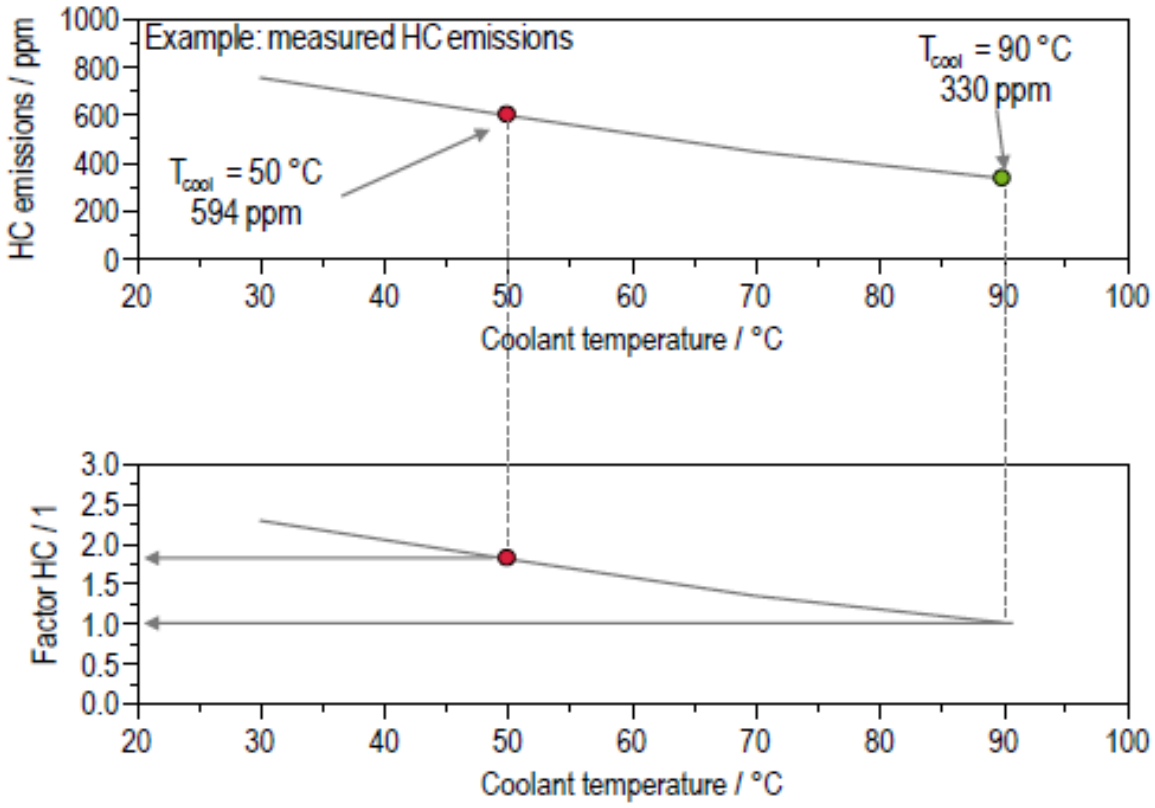

Figure 5.5 - Methodology for determining the correction factor for HCs measured on the test bench.

In this way, correction maps were determined for the three main pollutants as a function of coolant temperature, spark advance and lambda. Due to confidentiality reasons, the maps obtained are not explicitly included in this work, but a description of the main trends is given below.

As far as HCs are concerned, when the air/fuel ratio is fixed, the factors are elevated at low temperatures to tend to the unit, once the temperature of 90°C is reached. This trend is reproduced for all loads, but, as the load increases, the emissions amplify more and more at low temperatures. The CO value increases with rich mixture and, in this case, the correction factors are very similar with different loads. The NOx has a parabolic trend, with high values for very retarded/advanced ignition timing.

In order to determine the correct lambda value, an object from the GT Power library called *event manager* is used. This template may be used to implement two different control schemes:

1) an event-based test cycle, where multiple events, each with their own completion criteria, must be accomplished in a particular sequence and

2) a selection-based test cycle, where the completion of one event might result in multiple possible next events, depending upon the system state.

The user can pass through signals or specify outputs, based on a set of input values for each event. Using this object, the map has been corrected taking into account the event of engine start, use of secondary air, catalyst heating, as well as control strategy. In the figure below, for example, the lambda correction is shown for the first 10 sec of the cycle: the continuous curve shows the lambda value from the static map, while the dashed curve shows the corrected lambda value. The engine is cold, so no enrichment is required to protect the after treatment.

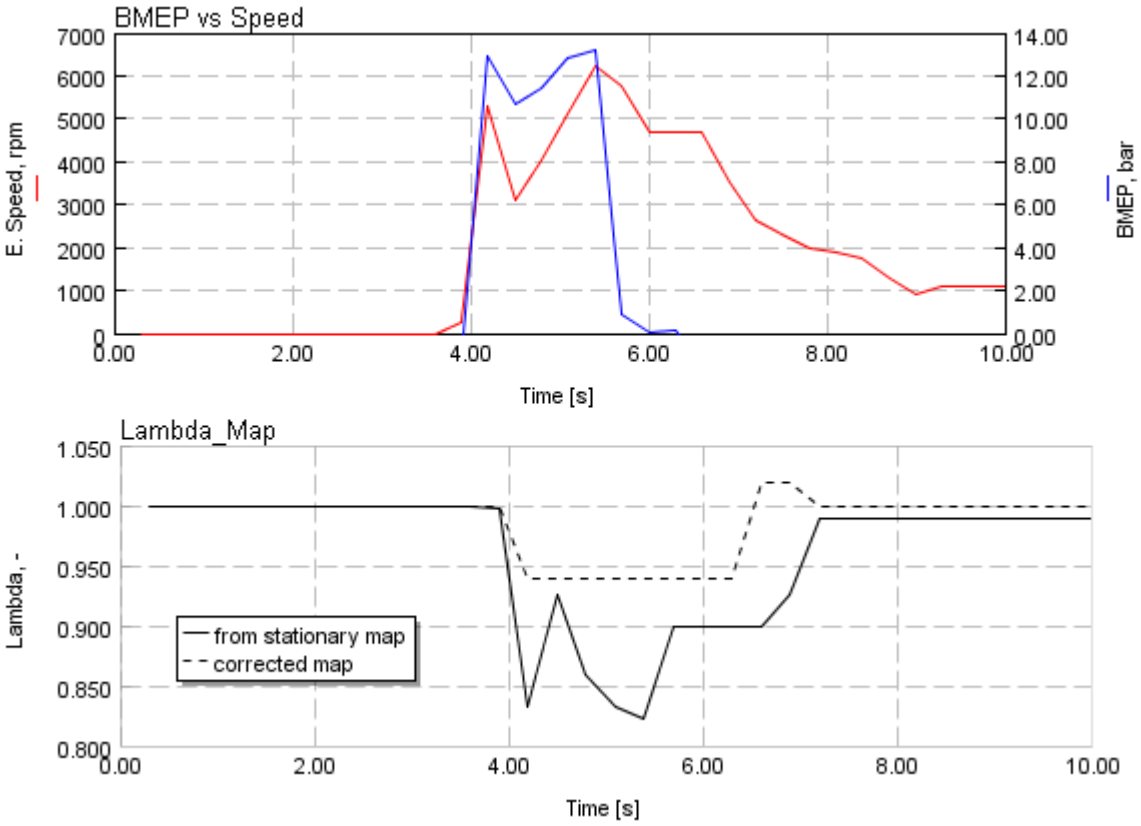

Figure 5.6 – Lambda for the first 10 sec of the cycle.

The oil and coolant temperature are evaluated during the cycle with a model developed in Lamborghini that is able to reproduce the two trends:

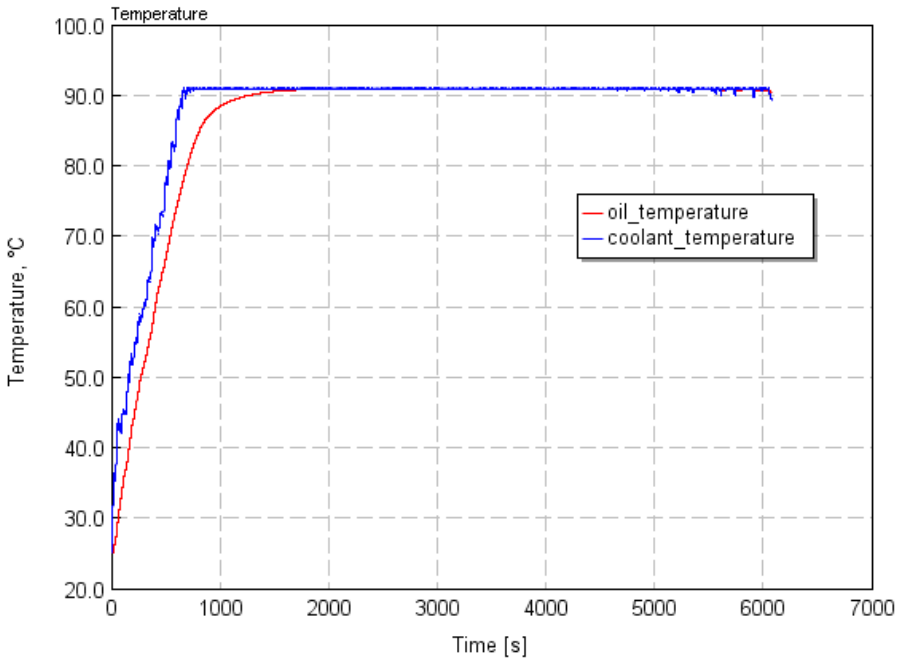

Figure 5.7 – Oil and coolant temperature during the RDE cycle.

Finally, the SA is advanced for the heating catalyst operations, so as to speed up the process.

Model Validation

The methodology described is validated on the NEDC cycle where raw emissions data were available. The comparison in terms of instantaneous and cumulative NOx, HC, CO is shown in the figure 5.8. In this case, since the objective is to evaluate the methodology of dynamic raw emission assessments with a static map approach, the experimental engine out emission maps are used. In this way, there is no risk of adding emissions modeling errors.

The results are very satisfactory: all the peaks are well detected, and the final cumulative numerical values are close to the experimental ones.

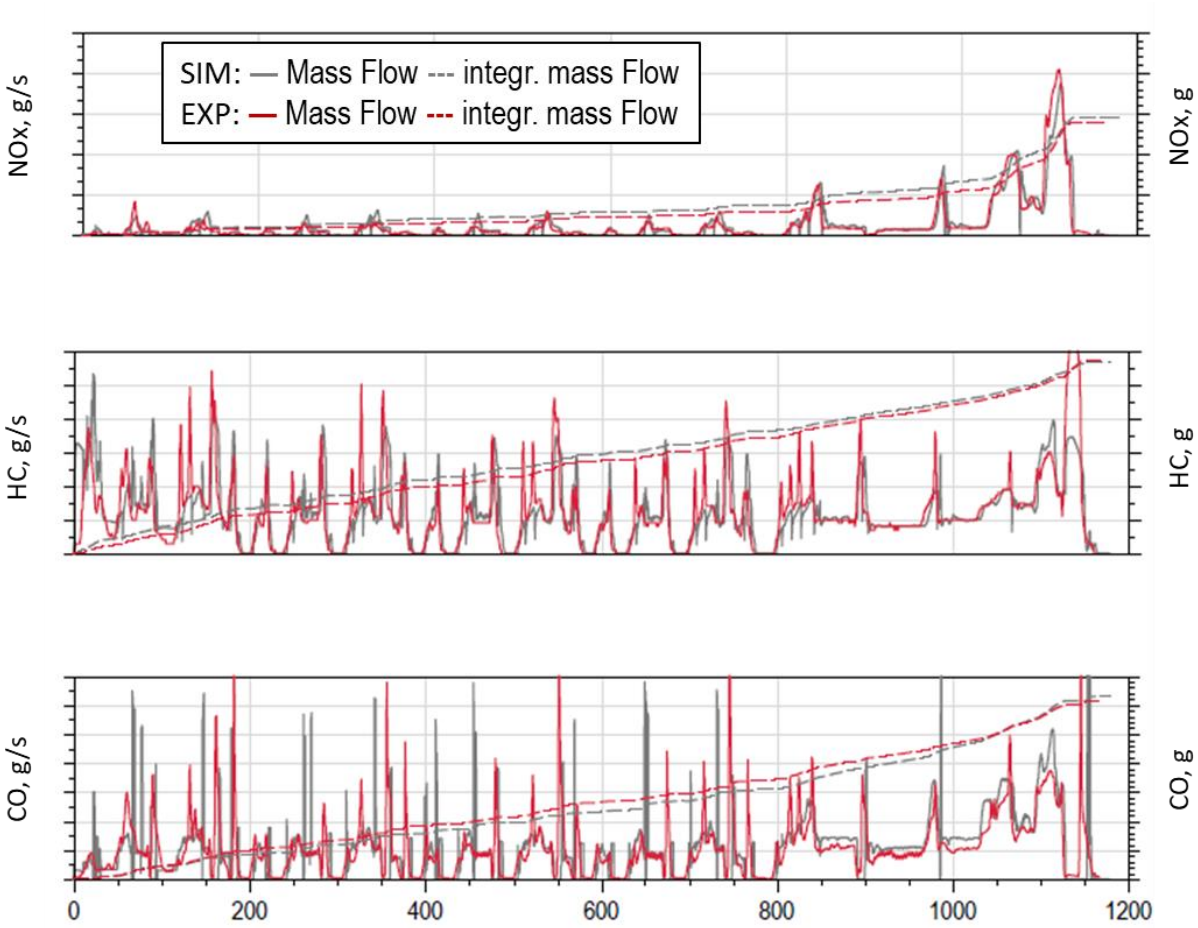

Figure 5.8 – Dynamic emission model validation on NEDC cycle in term of instantaneous and cumulative NO, HC and CO raw emissions.

Once it was established that the approach for the assessment of raw emissions over the cycle was reliable, we moved on to the use of modelling over the RDE driving cycle. In this case, the model was used using both the experimental and numerical stationary raw emission maps.

The figure 5.9 shows the cumulative emissions. The dashed curve is with the experimental emission map, while the continuous is obtained with the numerical raw emissions from the IV chapter. Once again, the results highlight the goodness of the emission maps obtained numerically, except for HCs where the numerical case underestimates the one obtained with the measurements.

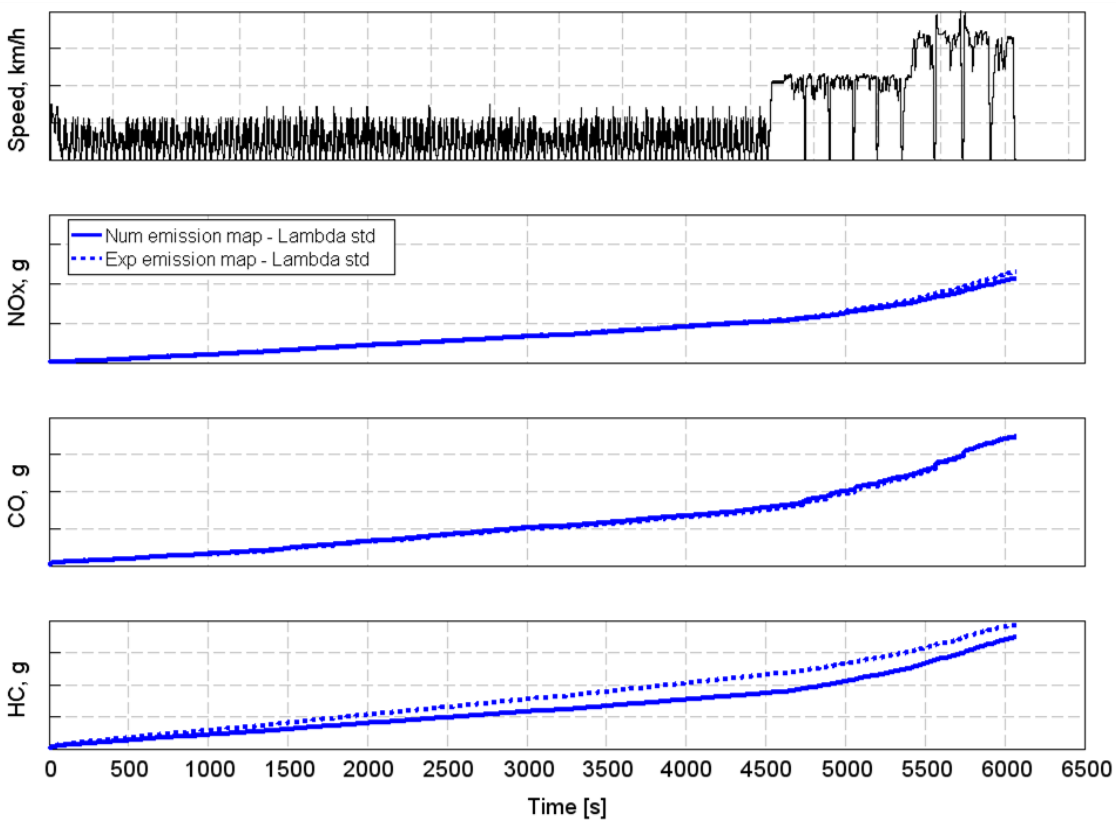

Figure 5.9 – Raw emissions trend on the RDE cycle with lambda standard calibration.

The same vehicle model is then used with a different engine calibration, i.e. using lambda map = 1. Here, the performance parameters and emission maps are updated. Also in this case the model is used with both the test bench emissions and the numerical values.

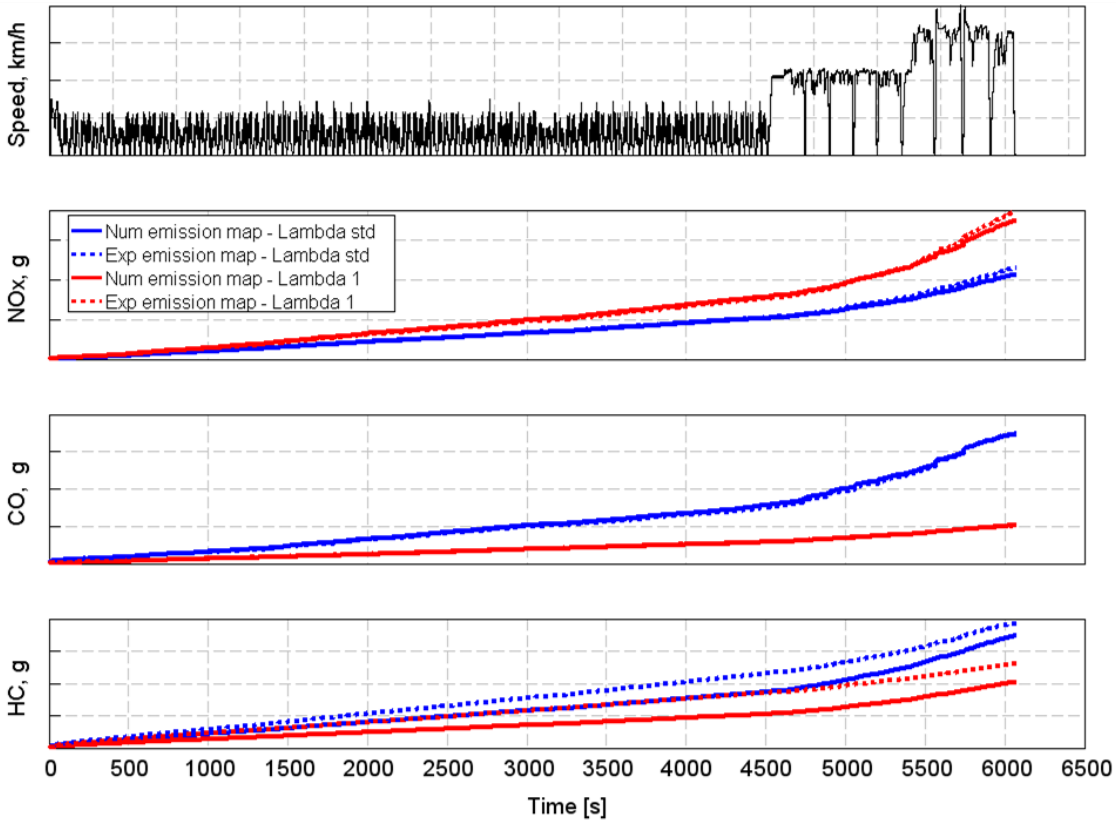

Figure 5.10 – Raw emissions trend on the RDE cycle with lambda standard and lambda =1 calibration.

The figure 5.10 shows the difference on the cycle in term of cumulated emissions. As expected with the stoichiometric mixture the NOx increases due to the higher temperature. On the contrary, HC and CO decrease. The percentage difference is -70.5% for the CO, -41.4% for the HC and +64% for the NOx production.

It is evident how a vehicle modeling associated with 1D combustion and emission models allows the evaluation on a driving cycle of engine out emissions with different engine calibration. This approach can also be used to evaluate the impact of a hardware variation. In fact, the model has been tested predictively by introducing water injection to the engine. Figure 5.11 summarizes the main result of the work. It is possible to compare the percentage increase in emissions by switching from a WLTC to a real driving cycle. Moving to a stoichiometric strategy, for the same cycle, the results show a reduction of

CO of 70.5 %, HC of 41.3 % and NO of 64 %. The use of water injection reduces CO and NOx emissions. On the other hand, there is a 13.9% increase in HC.

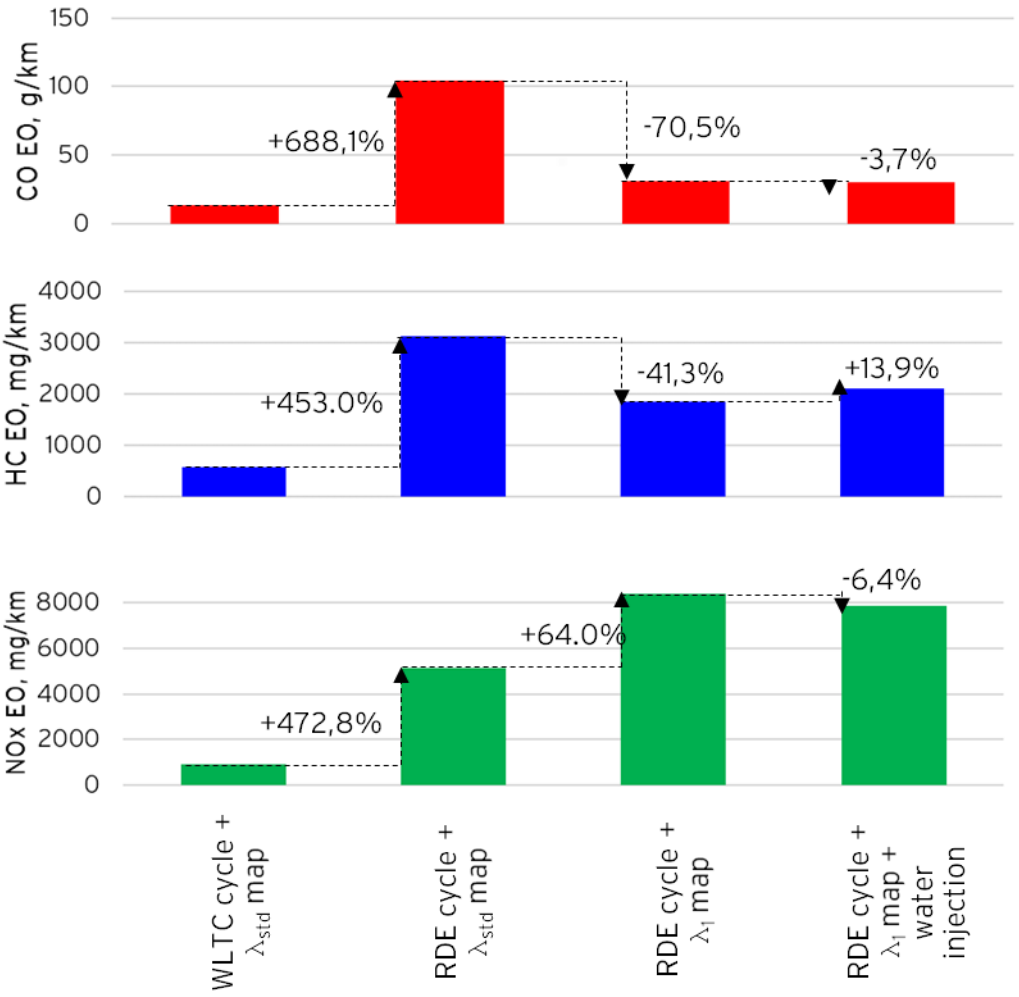

Figure 5.11 – Percentage difference on HC, CO and NO emissions for different driving cycles, calibrations and engine hardware.

6. Conclusions

The innovative contribution of this work can be hence recognized in the development of a 1D model characterized by a single set of tuning constants, allowing an accurate reproduction of the combustion process in the whole engine configurations. The results about the raw emissions put into evidence that the numerical approach predicts the experimental data of carbon monoxide (CO) and nitrogen oxides (NOx), but it is not enough advanced to reproduce the hydrocarbon (HC) level, although the variations with the engine operating parameters (speed, load, air/fuel ratio) are captured. The model is employed to study the water injection impact to draw the variation trend of the exhaust temperature, performance and the pollutant emissions. The computed HC, CO and NOx maps have been then embedded in a vehicle simulation to estimate the impact of the analysed technical solutions on a RDE cycle suggested by Lamborghini. In this way, with a numerical approach, a new hardware is analysed and its impact in term of raw pollution level is verified on a realistic drive cycle, that the new regulations will impose. So, a new approach to design the future high-performance engines has been proposed and the impact of the new regulations can be foreseen before experimental tests, reducing the time to market and the economic effort. Summarizing, the presented numerical approach showed the potential to predict, on a physical basis, the combined effects of various techniques on the engine performance. This methodology could represent an effective tool to identify the trade-off between engine complexity and expected improvements, contributing to support and drive the development process of new engine/vehicle. Future improvement could be a refinement of HC prevision.

7. References

1. European Commission, “Regulation No. 443/2009: Off. J. Eur. Union., L 140, 1–15”, http://eur-lex.europa.eu/legal-content/EN/TXT/?uri=celex:32009R0443, February 2017.
2. European Environment Agency, “Annual European Union greenhouse gas inventory 1990–2012 and inventory report 2014, Report No.: 9/2014”, 2014.
3. Moriya Y., Watanabe A., Uda H., Kawamura H., et al., “A Newly Developed Intelligent Variable Valve Timing System – Continuously Controlled Cam Phasing as Applied to a New 3 Liter Inline 6 Engine”, SAE paper 960579, 1996, doi: 10.4271/960579.
4. Sellnau M., Kunz T., Sinnamon J., Burkhard J., “2-step Variable Valve Actuation: System Optimization and Integration on an SI Engine”, SAE paper 2006-01-0040, doi:10.4271/2006-01-0040.
5. Kreuter P., Heuser P., Schebitz M., “Strategies to Improve SI-Engine Performance by Means of Variable Intake Lift, Timing and Duration”, SAE 920449, 1992, doi:10.4271/920449.
6. Roberts, M., “Benefits and Challenges of Variable Compression Ratio (VCR),” SAE Technical Paper 2003-01-0398, 2003, doi:10.4271/2003-01-0398
7. Shaik, A., Moorthi, NSV., Rudramoorthy, R., “Variable Compression ratio engine: a future power plant for automobiles-an overview”, *Proc. of the Istitution of Mechanical Engineers Part D: Journal of Aut. Eng.* Vol. 221(9):1159-1168, 2007, doi: 10.1243/09544070JAUTO573.
8. Wilcutts, M., Switkes, J., Shost, M., and Tripathi, A., "Design and Benefits of Dynamic Skip Fire Strategies for Cylinder Deactivated Engines," *SAE Int. J. Engines* 6(1):278-288, 2013, doi:10.4271/2013-01-0359.
9. Francqueville, L., Michel, J., “On the Effects of EGR on Spark-Ignited Gasoline Combustion at High Load”, *SAE Int J Engines* 7(4):1808-1823, 2014, doi:10.4271/2014-01-2628.

10. Grandin, B., Ångström, H., “Replacing Fuel Enrichment in a Turbo Charged SI engine: Lean Burn or Cooled EGR”, SAE Paper 1999-01-3505, 1999, doi:10.4271/1999-01-3505.
11. Potteau, S., Lutz, P., Leroux, S., Moroz, S. et al., “Cooled EGR for a Turbo SI Engine to Reduce Knocking and Fuel Consumption”, SAE Technical Paper 2007-01-3978, 2007, doi:10.4271/2007-01-3978.
12. Alger, T., Chauvet, T., Dimitrova, Z., “Synergies between High EGR Operation and GDI Systems”, *SAE Int J Engines* 1(1):101- 114, 2008, doi:10.4271/2008-01-0134.
13. Lee, S., Park, S., Kim, C., Kim, Y.M., Kim, Y., Park, C., “Comparative study on EGR and lean burn strategies employed in an SI engine fueled by low calorific gas”, *Applied Energy* 129: 10-16, 2014 doi:10.1016/j.apenergy.2014.04.082.
14. Lattimore, T., Wang, C., Xu, H., Wyszynski, M.L., Shuai, S., “Investigation of EGR Effect on Combustion and PM Emissions in a DISI Engine”, *Applied Energy* 161: 256-267, 2016, doi: 10.1016/j.apenergy.2015.09.080.
15. Wei, H., Zhu, T., Shu, G., Tan, L., Wang, Y., “Gasoline engine exhaust gas recirculation – A review”, *Applied Energy* 99: 534-544, 2012,doi:10.1016/j.apenergy.2012.05.011.
16. Hoppe, F., Thewes, M., Baumgarten, H. and Dohmen, J., “Water injection for gasoline engines: Potentials, challenges, and solutions”, *International J of Engine Research* 17(1):86-96, 2016, doi: 10.1177/1468087415599867.
17. Soyelmez, M.S., Ozcan, H., “Water Injection Effects on the Performance of Four-Cylinder, LPG Fuelled SI Engine”, Open Access Scientific Reports, 2(1), 2013, doi: 10.4172/scientificreports.591.
18. Busuttil, D., Farrugia, M., “Experimental Investigation on the Effect of Injecting Water to the Air to Fuel Mixture in a Spark Ignition Engine”, *MM (Modern Machinery) Science Journal* 1:585-590, 2015.
19. Iacobacci, A., Marchitto, L., Valentino, G., “Water Injection to Enhance Performance and Emissions of a Turbocharged Gasoline Engine under High Load Condition”, *SAE Int. J. Engines* 10(3):2017, doi:10.4271/2017-01-0660.
20. Lanzafame, R., “Water Injection Effects In A Single-Cylinder CFR Engine”, SAE Technical Paper 1999-01-0568, 1999, doi:10.4271/1999-01-0568.

21. Özkan H., Söylemez M.S., “Experimental Investigation of the Effects of Water Addition on the Exhaust Emissions of a Naturally Aspirated Liquefied-Petroleum-Gas fueled Engine”, *Energy&Fuels* 19(4): 1468-1472, 2005, doi: 10.1021/ef049850g.
22. Boretti, A., “Water injection in directly injected turbocharged spark ignition engines”, *Applied Thermal Engineering* 52(1):62-68, 2013 doi:10.1016/j.applthermaleng.2012.11.016.
23. d'Adamo, A., Berni, F., Breda, S., Lugli, M. et al., “A Numerical Investigation on the Potentials of Water Injection as a Fuel Efficiency Enhancer in Highly Downsized GDI Engines”, SAE Paper 2015-01-0393, 2015, doi:10.4271/2015-01-0393.
24. Siano, D., Valentino, G., Bozza, F., Iacobacci, A., Marchitto, L., "A Non-Linear Regression Technique to Estimate from Vibrational Engine Data the Instantaneous In-Cylinder Pressure Peak and Related Angular Position", SAE Technical Paper 2016-01-2178, 2016, doi:10.4271/2016-01-2178.
25. Bozza, F., De Bellis, V., Minarelli, F., and Cacciatore, D., "Knock and Cycle by Cycle Analysis of a High Performance V12 Spark Ignition Engine. Part 2: 1D Combustion and Knock Modeling," *SAE Int. J. Engines* 8(5):2002-2011, 2015, doi:10.4271/2015-24-2393.
26. De Bellis, V., Bozza, F., Fontanesi, S., Severi, E. et al., "Development of a Phenomenological Turbulence Model through a Hierarchical 1D/3D Approach Applied to a VVA Turbocharged Engine," *SAE Int. J. Engines* 9(1):506-519, 2016, doi:10.4271/2016-01-0545.
27. Morgan, N., Smallbone, A., Bhave, A., Kraft, M., Cracknell, R., Kalghatgi, G., “Mapping surrogate gasoline compositions into RON/MON space”, *Combustion and Flame* 157(6): 1122–1131, 2010, doi: 10.1016/j.combustflame.2010.02.003.
28. Tanaka, S., Ayala, F., Keck, J.C., “A reduced chemical kinetic model for HCCI combustion of primary reference fuels in a rapid compression machine”, *Combustion and Flame* 133(4): 467-481, 2003, doi: 10.1016/S0010-2180(03)00057-9.
29. Liu, Y., Jia, M., Xie, M., Pang, B., “Development of a New Skeletal Chemical Kinetic Model of Toluene Reference Fuel with Application to Gasoline Surrogate Fuels for

Computational Fluid Dynamics Engine Simulation", *Energy Fuels* 27(8):4899–4909, 2013, doi: 10.1021/ef4009955.

30. Andrae, J., "Comprehensive chemical kinetic modeling of toluene reference fuels oxidation", *Fuel* 107:740–748, 2013, doi: 10.1016/j.fuel.2013.01.070.
31. De Bellis, V., Severi, E., Fontanesi, S., Bozza, F., "Hierarchical 1D/3D approach for the development of a turbulent combustion model applied to a VVA turbocharged engine. Part II: combustion model", *Energy Procedia* 45: 1027-1036, 2014, doi: 10.1016/j.egypro.2014.01.108.
32. Douaud, A., Eyzat, P., "Four-Octane-Number Method for Predicting the Anti-Knock Behavior of Fuels and Engines", SAE Technical Paper 780080, 1978, doi: 10.4271/780080.
33. Lafossas, F.A., Castagne M., Dumas, J.P., Henriot, S., "Development and validation of a knock model in spark ignition engines using a CFD code", SAE Technical Paper 2002-01-2701, 2002, doi:10.4271/2002-01-2701.
34. Teodosio, L., De Bellis, V., and Bozza, F., "Fuel Economy Improvement and Knock Tendency Reduction of a Downsized Turbocharged Engine at Full Load Operations through a Low-Pressure EGR System," *SAE Int. J. Engines* 8(4): 1508-1519, 2015, doi:10.4271/2015-01-1244.
35. Bozza, F., De Bellis, V., Siano, D., "A Knock Model for 1D Simulations Accounting for Cyclic Dispersion Phenomena", SAE Paper 2014-01-2554, 2014, doi:10.4271/2014-01-2554
36. Arsie, I, Pianese, C.; Rizzo, G., "Models for the prediction of performance and emissions in a spark ignition engine - A sequentially structured approach," SAE Technical Paper 980779, 1998, doi: 10.4271/980779.
37. Kaplan, J. A., & Heywood, J. B., "Modeling the spark ignition engine warm-up process to predict component temperatures and hydrocarbon emissions," SAE Technical Paper 1991, 361-376, doi: 10.4271/910302.
38. Lavoie, G. A., "Correlations of combustion data for SI Engine calculations–laminar flame speed, quench distance and global reaction rates," SAE Technical Paper1978,1015-1033, doi: 10.4271/780229.
39. Schramm, J., & Sorenson, S. C., "A model for hydrocarbon emissions from SI engines," SAE Technical Paper 1990, 2331-2349, doi: 10.4271/902169

40. North, G., L., Santavicca, D., A., “The fractal nature of premixed turbulent flames,” Combustion Science and Technology 72(4-6): 215-232, 1990, doi: 10.1080/00102209008951648.